The Open Circuit Voltage of Polymer Electrolyte Membrane Fuel Cells

Die Leerlaufspannung von Polymerelektrolyt-Membran-Brennstoffzellen

Von der Fakultät für Maschinenwesen der Rheinisch-Westfälischen Technischen Hochschule Aachen zur Erlangung des akademischen Grades einer Doktorin der Ingenieurwissenschaften genehmigten Dissertation

vorgelegt von

Yun Cai

Berichter: Univ.-Prof. Dr. rer. nat. Werner Lehnert

Univ.-Prof. Dr.-Ing. Bastian J. B. Etzold

Tag der mündlichen Prüfung: 18. 12. 2019

Abstract

The proton exchange membrane fuel cell (PEFC), because of its wide application and low operating temperature, rapid startup, high efficiency, simplicity of operation, and generation of environmentally friendly products when hydrogen is used as fuel [1-5], has attracted the attention of researchers. Open circuit voltage (OCV), voltage without load, has a significant effect on the lifetime of PEFCs, and is therefore a good tool to diagnose the malfunction of fuel cells [6] especially on MEA failure monitoring.

Mixed potential, caused by surface oxidation, oxygen reduction reaction, and hydrogen crossover are widely accepted reasons why the experimental OCV (about 1 V) is lower than the theoretically expected one [7-9] even considering the effect of temperature and pressure or gas solubility. In order to examine this discrepancy, the open circuit potential (OCP) of Pt disk, carbon support and Pt on carbon support under different cases is studied in half-cell experiments, and the OCV of Pt on carbon support is studied in single cell experiments in this thesis.

The OCP of the half-cell from 30 °C to 80 °C for different gas compositions in various electrolyte concentrations, is studied using the electrochemical measurement of cyclic voltammetry (CV), linear sweeping voltammetry (LSV) and chrono-potentiometry by two different equipments. In order to understand the kinetics of surface oxidation, a model including Nernst equation and first order reaction is used for the OCP calculation of different catalysts (Pt disk, carbon support and Pt on carbon support) under different conditions. As a result, the experimental results fit well with the calculations.

The OCV of single cell at 40, 60 and 80 °C for different gas compositions at different relative humidity is studied using the electrochemical measurement of CV, and LSV, potential holding added chrono-potentiometry, and electrochemical impedance spectroscopy (EIS) with Baltic cell equipment. The over voltage caused by hydrogen crossover is obtained by calculation through crossover current and charge transfer resistance, and by experiment through the difference between OCP of the half-cell and OCV of the single cell. In addition, the experimental over voltage is much smaller than the calculated one.

Kurzfassung

Brennstoffzellen mit Protonen-Austausch-Membran (engl. proton exchange membrane fuel cell, PEFC) finden als Energiewandler aktuell eine breite Anwendung. Die wichtigsten Vorteile dieses Typs sind eine niedrige Betriebstemperatur, hohe Leistungsdichte, Einfachheit in der Anwendung, kurze Anlaufzeit und umweltfreundliche Emissionen bei Betrieb mit reinem Wasserstoff [1-5]. Ein Betrieb der Zelle bei offener Zellspannung (engl. open circuit voltage, OCV) hat einen signifikanten Einfluss auf die Lebensdauer der PEFC. Darüber hinaus ist die gemessene offene Zellspannung ein guter Indikator für die Diagnose von Betriebsstörungen von Brennstoffzellen [6].

Der Wert der OCV liegt in Experimenten mit ca. 1 V deutlich unter dem theoretischen Wert von 1.23 V [7, 8]. Diese Abweichung wird der Oberflächenoxidation des Platinkatalysators welches die Ausbildung eines Mischpotentials bedingt, der Löslichkeit der Gase im flüssigen Elektrolyten und der Diffusion der Gase durch die Polymermembran zugeschrieben. In der vorliegenden Arbeit werden die Effekte getrennt untersucht. Der Einfluss des Mischpotentials auf die offene Zellspannung wird in Halbzellen-Experimenten an Pt-Elektroden und an technischen Elektrodenschichten aus Pt Nanopartikeln auf Kohlenstoffträger untersucht. Dafür werden zwei unterschiedliche Zelltypen, eine sogenannte "Glaszelle" und eine "RDE Zelle" (engl. rotating disk elektrode, RDE) verwendet. Dabei werden sowohl die Gaszusammensetzung, der Elektrolyt als auch die Temperatur als Einflussparameter variiert. Das Ziel ist die Charakterisierung der Kinetik der Oberflächenoxidation von Platinkatalysatoren.

Als experimentelle Methoden werden die zyklische Voltammetrie (CV) und "linear sweeping voltammetry" (LSV) in Kombination mit zeitabhängiger Potentiometrie verwendet. Zur Interpretation der Ergebnisse dient ein vereinfachtes Reaktionsmodell. Um aus den Experimenten mit Halbzellen Aussagen für technisch relevante Brennstoffzellen treffen zu können, werden die oben beschriebenen Experimente durch Versuche an Einzelzellen vom Typ "Baltic Fuel Cell" ergänzt. Der Einfluss der Wasserstoffpermeation lässt sich durch den Vergleich von Halbzell- und Zellmessungen charakterisieren. Die theoretische Überspannung durch den Umsatz des von der Anodenseite übergetretenen Wasserstoffs, wird auf Grundlage von Diffusionsmessungen durchgeführt. Der so erhaltene Diffusionsstrom kann mit Hilfe der "charge transfer resistance" in eine theoretische Überspannung überführt werden. Die experimentell beobachtete Überspannung ist deutlich geringer als der berechnete Wert.

Contents

Chapter 1 Introduction

Energy and environmental issues [10, 11] are the crucial topics in the world because of the severe energy shortage and environmental pollution, which is caused by increasing population [12, 13] and carbon dioxide (CO_2) emissions [14, 15]. That is why renewable energy is very important. However, even more important is discovering how to store such energy in a condensed way when the supply of the renewable energy source is intermittent. This is necessary because an intermittent energy source cannot meet the energy need. At present, the possible energy storing methods include batteries, chemical bonds, compressed air [16] etc. In this case, a kind of prospective technology is fuel cells [17-28], which can directly convert the chemical energy into electrical energy [29, 30], and can be widely adapted for automobiles, scooters and bicycles, golf carts, utility vehicles, distributed power generation, backup power, portable power, space, airplanes and locomotives, boats, and underwater vehicles. Thus it will emerge into the public view [31].

Fuel cells consist of several types, including the alkaline fuel cell (AFC), molten carbonate fuel cell (MCFC), phosphoric acid fuel cell (PAFC), solid oxide fuel cell (SOFC) and proton exchange membrane fuel cell (PEFC). Among them, PEFC, which can convert the free-energy of the hydrogen–oxygen reaction into electricity, has attracted the attention of researchers and has become a promising candidate for transportation and electrical power generations due to its low operating temperature, rapid startup, high power density, simplicity of operation, and generation of environmentally friendly by- products when hydrogen is used as a fuel [1-5].

1.1 The fundamental of PEM fuel cells

PEFC mainly contains one membrane (PEM), two electrodes (anode and cathode), and a flow field plate. The H_2 oxidation reaction occurs on the anode side (Equation 1.1), and as a result the protons go through the membrane and react with O_2 and generate H_2O in the cathode (Equation 1.2). The electrons transfer from anode to cathode by the external circuit. The schematic graph displays this in Figure 1.1.

$$H_2 \rightarrow 2H^+ + 2e^- \quad (1.1)$$

$$½\ O_2 + 2H^+ + 2e^- \rightarrow H_2O \quad (1.2)$$

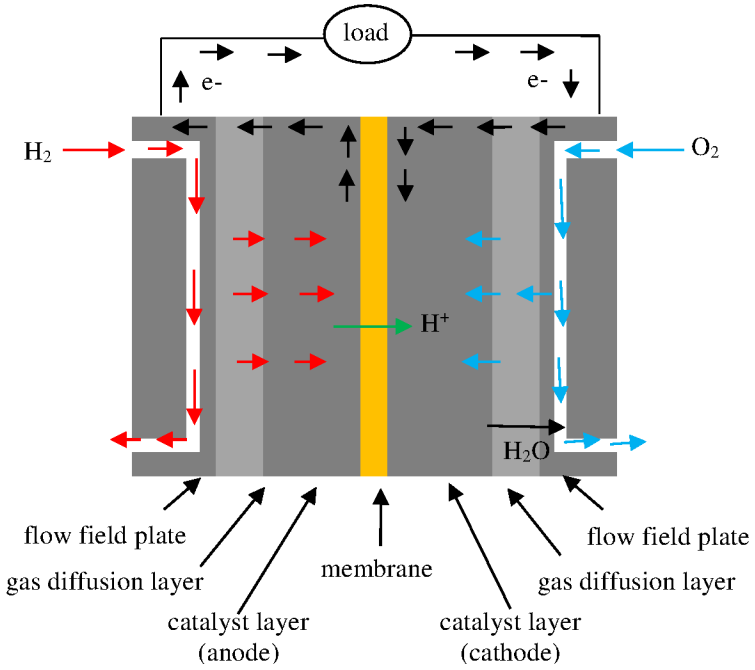

Figure 1.1. The schematic graph of PEM fuel cells.

The two major hurdles limiting the large scale commercialization of PEFC are cost and durability. The key to reduce the cost is to reduce the Pt loading, which can be accomplished by dispersing platinum on various carbon supports [32, 33] or using non-noble metal catalysts [34]. The factors [35] affecting the durability of PEFC, contains catalyst layer degradation, gas diffusion layer degradation [36], carbon support corrosion [37], and degradation of the polymeric membrane [38-40]. Pei et al. [41, 42] have reviewed the main factors affecting the lifetime of PEFC in automotive applications and have particularly noted that start and stop cycles and the dynamic operation of PEFC provoke a reduced lifetime. Thus, load cycling is one of the main reasons for PEFC degradation. The real driving cycles of PEFC were analyzed and it was identified that 56.6% of the total PEFC degradation can be traced to dynamic load changes, while 33% of the degradation occurred under start/stop cycles with 5.8% under high power load and 4.7% of the degradation rate occurring during periods of idling.

1.2 Open circuit voltage

The OCV is observed when no current is drawn from the fuel cell. It has significant uses such as being a tool for diagnosing fuel cells [6] and in its application for accelerated life-time tests for fuel cells. OCV measurement plays a great role in monitoring MEA failure, such as in membrane failure during pinholes formation. An unusual OCV may indicate some potential defects in the membrane, gaskets or even bipolar plates [43-45].

Theoretically, OCV, voltage without load, should be equal to 1.23 V at normal temperature and pressure (NTP) condition. According to the calculation [7-9, 46] considering the temperature and gas pressure, it should be about 1.22 V (NTP). If the gas solubility is considered [8, 46], the value should be about 1.01 V (NTP). However, fuel cells experience an open circuit voltage [29], which is between 0.9 V and 1 V per cell if there is fuel at the anode and air at the cathode, respectively. Some researchers [6, 7] have provided several reasons why the experimental potential is lower than the theoretical value. For example, Vilekar and Datta [6] give a good introduction on this issue with various reasons and related analysis given by other researchers.

At present, the most widely accepted explanation for this problem offers two possibilities. One involve the idea that mixed potential as compared to thermodynamic potential [47-50] leads to lower OCV in acidic medium. The other interpretation is that H2 crossover [29] occurs in the single cell or in the stack of fuel cells causing the discrepancy.

To date, a quantitative explanation for such OCV behavior has not been clear in the literature. Many explanations for it have been given by researchers. However sufficient illumination on the subject has not yet been provided. Next, we will focus on mixed potential and hydrogen crossover.

1.3 Mixed potential and hydrogen crossover

1.3.1 The mixed potential of Pt electrode

Compared to other cathodic catalysts, platinum has been the first choice for ORR of PEFC. In order to better understand mixed potential, it is necessary to know the surface oxidation of pure Pt. About 50 years ago, the surface oxidation of pure platinum in 0.5 or 1 M sulfuric acid

solution at different temperatures with N_2 saturated was studied by many researchers [51-57]. Several models have been used to explain the reaction mechanism.

Conway's group [57] studied the condition of the electrochemically oxidized platinum surface in 0.5 M H_2SO_4 solution by cyclic voltammetry and provided calculations to explain the individual reaction steps. The oxidation of pure platinum does not only involve the steps from Pt to PtOH and then to PtO, then to PtO_x, but also includes several medium reactions from Pt_xOH to PtOH, as shown in the Equation 1.3. And the responding CV peaks of the $OH_{species}$ at 0.89 V, 0.94-0.95 V, and 1.04-1.05 V, separately, are attributed to different surface species (such as Pt_4OH, Pt_2OH, and PtOH). Next, the adsorbed hydroxyl group (OH_{ads}) generated on the interface place, exchange between OH_{ads} and the surface platinum atoms, and thus lead to the formation of a quasi-3D lattice, as shown in Equation 1.4. As the rearranged PtOH layer formed completely, PtO generates according to Equation 1.5. This reaction occurs even beyond 1.1 V. However, the conformation of a completed PtO structure needs a higher potential, and then the step from PtO to PtO_x occures. The products of these 6 steps can be described as seen in Figure 1.2, in which the figure from (a) to (f) correspond to the product of $PtOH_{ads}$, $(OH–Pt)_{quasi\text{-}3D\ lattice}$, complete $(OH–Pt)_{quasi\text{-}3D\ lattice}$, $PtO_{quasi\text{-}3D\ lattice}$, completed $PtO_{quasi\text{-}3D\ lattice}$ and PtO_x, separately.

$$Pt + H_2O \rightarrow Pt–OH_{ads} + H^+ + e^- \quad (1.3)$$

$$Pt–OH_{ads} \rightarrow (OH–Pt)_{quasi\text{-}3D\ lattice} \quad (1.4)$$

$$(OH–Pt)_{quasi\text{-}3D\ lattice} \rightarrow (Pt–O)_{quasi\text{-}3Dlattice} + H^+ + e^- \quad (1.5)$$

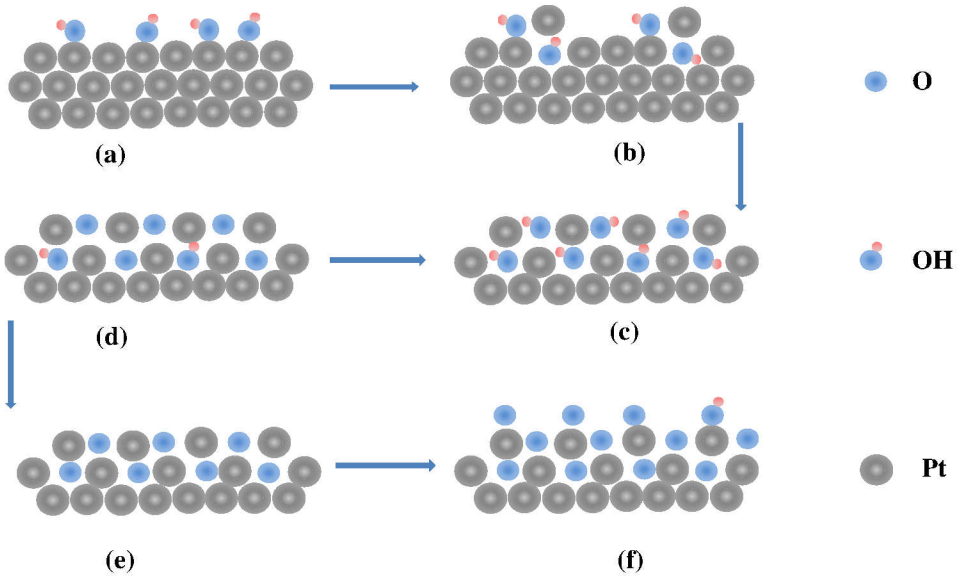

Figure 1.2. The schematic representation of continuing oxidation of a Pt surface up to and beyond the "PtO" state with rearrangement [57].

Nagy and You [58] have investigated the initial oxidation and reduction of Pt (111) single crystal faces in 0.1 M $HClO_4$ solutions and in 0.1 M CsF by CV and synchrotron x-ray scattering. They propose a three-step mechanism. Firstly, the platinum surface is oxidized to PtOH by the initial adsorption of OH at 0.9 V. Secondly, the PtOH is rearranged to HOPt at $\leqslant$ 1.20 V and then oxidized to PtO at >1.20 V, or the PtOH oxide to PtO and then finally it is rearranged to OPt. Drnec et al. [59] study the surface oxides on a Pt (111) surface in 0.1 M $HClO_4$ by using in-situ surface x-ray diffraction. They propose that the surface restructuring in the incipient oxidation stages is consistent with a place exchange process between Pt and O atoms which sharply peaks in the CV at 1.05 V. The further oxidation and restructuring of surface occurs in the range of $\geqslant$ 1.15 V. Jerkiewicz et al. [52] re-examine the mechanism of platinum surface electro-oxidation by cyclic-voltammetry, in situ electrochemical quartzcrystal nanobalance (EQCN) and ex situ auger electron spectroscopy (AES) measurements. They state platinum electro-oxidation does not involve OH_{ads} as an intermediate, and have proposed a two-step mechanism, where in step 1 the adsorption of half a monolayer of oxygen takes place in the range of $0.85 \leqslant E \leqslant 1.10$ V. Step 2 describes adsorption of the second half monolayer of oxygen and the further oxidation of the platinum surface layer to PtO in the range of $1.20 \leqslant E \leqslant 1.40$ V.

However, as the electrode is saturated with O_2, the reaction on the surface of Pt is more complex, being not only the platinum oxidation, but also the oxygen reduction reaction, and thus leading a formation of mixed potential [50].

For the study of oxygen reduction reaction, Anastasijević, Vesović, and Adžić [60] calculated several reasonable pathways:

(1) 'direct' four-electron reduction pathway;

(2) a two-electron 'series' pathway including the formation of hydrogen peroxide;

(3) a 'series' pathway including two- and four-electron reduction.

(4) a 'parallel' pathway which is a combination of (l), (2) and (3);

(5) an 'interactive' pathway in which diffusion of species from a 'series' path into a 'direct' path is possible.

Markovic et al. [61] isolates 3 possibilities, that O_2 can be reduced either directly to water (direct 4-electron reduction) electrochemically, or to adsorbed hydrogen peroxide ($H_2O_{2,ad}$) ('series' 2-electron reduction), and then further reduced to water, or chemically decomposed on the electrode surface, and/or desorbed into the electrolyte solution. Some experimental results suggest that a series pathway via an $(H_2O_2)_{ad}$ intermediate is the most viable pathway. The ORR mechanism on Pt has also been investigated by other literature [62-68]. In fuel cell processes, the 4-electron direct pathway is highly preferred according to Song et al. [69].

Therefore, the open circuit potential (OCP) can be comprehended as a mix of the platinum oxidation and the four-electron oxygen reduction reaction. Here, the term OCP is used instead of OCV because it presents a potential of one electrode for half-cell. Moreover, the steady state of the OCP of Pt can be up to 1.06 V (versus NHE, 25 °C, 1.0 atm) [70]. Parthasarathy et al. [71-73] observed the OCV of Pt with Nafion membrane coating, creating an environment similar to that of a fuel cell.

1.3.2 The mixed potential of carbon support

It's known that the catalyst of fuel cells can be Pt, Pt alloy and Pt-free compounds. Whatever they are, carbon materials are commonly used as electro-catalyst supports because of their high electrical conductivity and surface area, as well as their wide variety of structural and chemical

properties. However, the carbon electrochemical oxidation limits its use as an electrode in electrochemistry.

As per Borup's group [74] and Hasche's group [75], it is known that for fuel cells the carbon oxidation below 1.2 V can be negligible because of its slow kinetics under normal operating conditions. However, it occurs easily on the cathode during abnormal operational conditions, such as fuel starvation or the formation of an air/fuel boundary due to repeated start up/shut down cycles as given in literature [30, 76-81]. Such situations cause increases in the potential of electrodes higher than the OCV. The high potential accelerates the kinetics of electrochemical corrosion and in the end deteriorates the performance and durability of fuel cells [78, 81]. Moreover, carbon oxidation effects the loss of structural carbon, a significant change of the surface properties, a reduced conductivity of catalysts and a weakened interaction with the catalysts. These results in an aggregation of isolated metal particles when carbon materials are used for a catalyst support [74, 82-86]. This great carbon support oxidation causes a performance reduction of PEFC [74, 87]. Moreover, surface oxidation may result in an increase of the surface hydrophilicity, and as a consequence, a decrease in gas permeability [88]. This is probably because the pores are flooded with water, thus hindering gas transport [89]. Because of these factors, the study of carbon corrosion is essential.

It is known that carbon reacts with water and can be oxidized to carbon monoxide or carbon dioxide following Equation 1.6 and Equation 1.7 [85]. And the carbon monoxide can be oxidized to carbon dioxide according to Equation 1.8 [85].

$$C + H_2O \rightarrow CO + 2H^+ + 2e^-; \qquad E^0 = 0.518\ V \qquad (1.6)$$

$$C + 2H_2O \rightarrow CO_2 + 4H^+ + 4e^-; \qquad E^0 = 0.207\ V \qquad (1.7)$$

$$CO + H_2O \rightarrow CO_2 + 2H^+ + 2e^-; \qquad E^0 = -0.103\ V \qquad (1.8)$$

Researchers give several mechanisms of the carbon oxidation when platinum is present or absent. In the absence of platinum, surface oxide generation of carbon in acidic electrolytes involves the general steps of oxidation of carbon in the lattice structure followed by hydrolysis and gasification of oxidized carbon to CO_2 [75, 90, 91]. The detailed mechanism [85] is not yet

fully understood but is presumed to include parallel formation of surface and gaseous carbon oxides by disproportionate formation of oxygen functional groups. One generic mechanism is the surface adsorption of oxygen atoms, followed by oxide species formation as reaction intermediates, and at last further oxidization to CO_2. The pathway is shown schematically as below [92, 93]:

$$C + H_2O \rightarrow C–O_{ad} + 2H^+ + 2e^- \quad (1.9)$$

$$C–O_{ad} + H_2O \rightarrow CO_2 + 2H^+ + 2e^- \quad (1.10)$$

There are different forming mechanisms of surface functional groups offered [74, 75, 94, 95]. For example, the Equation 1.11 and Figure 1.4 is shown, separately, reported by Borup et al. [40] and Cai's group [90] as:

$$R–C_s–H \rightarrow R–C_s–OH \rightarrow R–C_s\,O \rightarrow R–C_sOOH \quad (1.11)$$

In the above the subscript 's' indicates surface species. The initial oxides formed on active sites promote the formation of gaseous products, such as CO, CO_2, and O_2. However, as the carbon surface becomes saturated with suitably stable surface oxides during electrochemical oxidation, the formation of additional oxides may be inhibited [92]. These surface oxides could slow down the reaction kinetics towards further oxidation and formation of gaseous products [96]. The schematic diagram is shown in Figure 1.3.

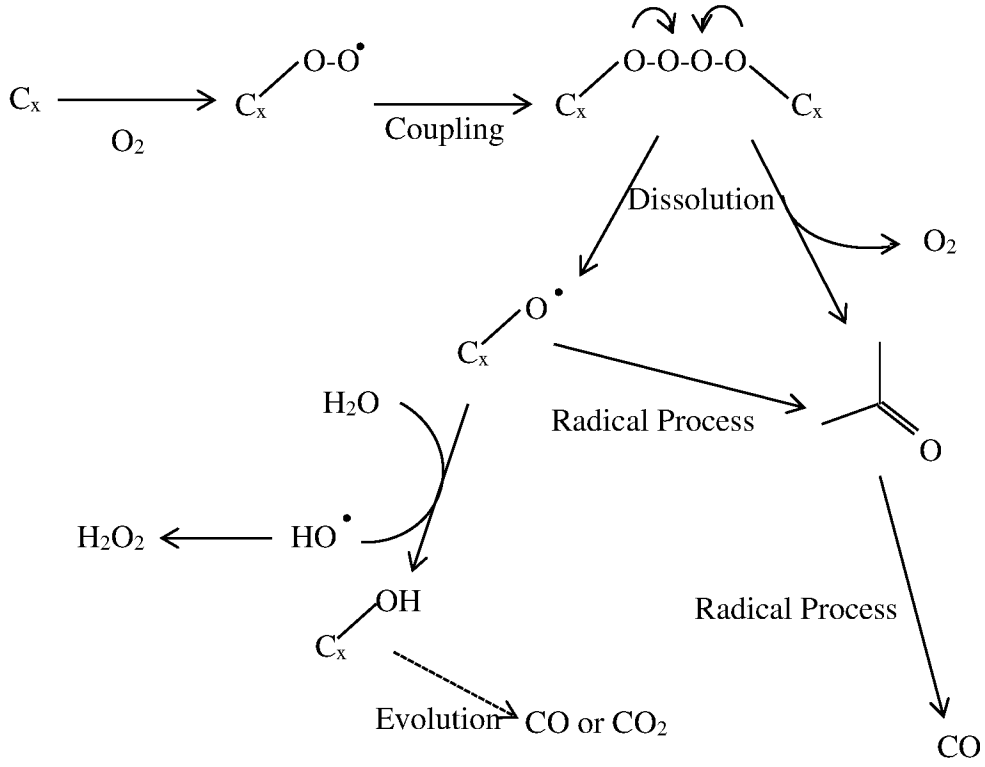

Figure 1.3. Carbon corrosion in the absence of Pt [90].

What's more, the carbon may be directly electrochemically oxidized to CO_2 as reported by Kinoshita [92], as shown in Equation 1.12 and 1.13.

$$C + O_2 \rightarrow CO_2; \qquad E^0 = 2.044\ V \tag{1.12}$$

$$C + \tfrac{1}{2} O_2 \rightarrow CO; \qquad E^0 = 0.711\ V \tag{1.13}$$

Also, Cai's group [90] concludes that when Pt is present it can react with oxygen and water to generate highly reactive OH and OOH radicals, as shown in Figure 1.4 (a). These radicals can attack carbon, produce surface oxygen groups, which can then decompose to form gaseous CO and CO_2 at high temperatures, as shown in Figure 1.4 (b).

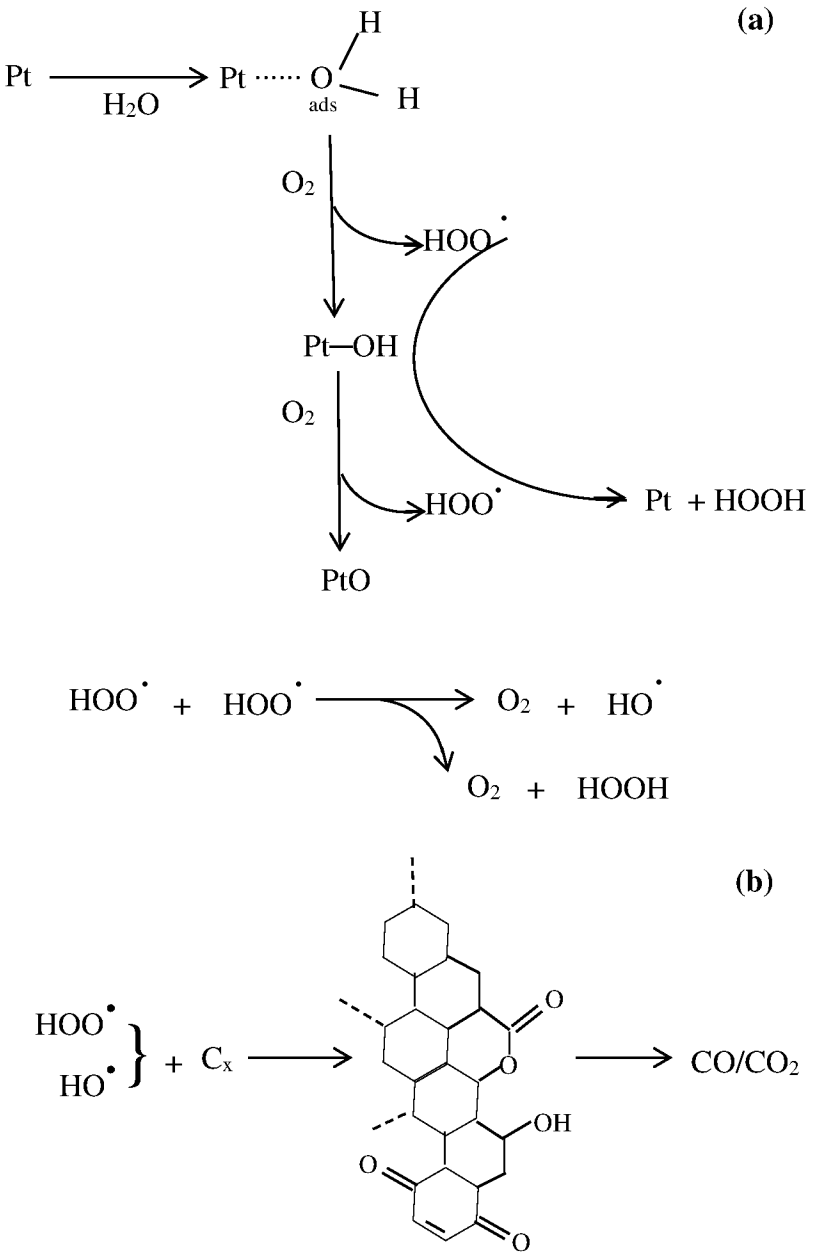

Figure 1.4. (a) Formation of radicals by reaction of Pt, O_2, and H_2O; (b) carbon corrosion in the presence of Pt, O_2 and H_2O [90].

1.3.3 Hydrogen crossover

It is known that the membrane should be electrically nonconductive and practically impermeable to reactant gases. However, some electrons can go through membranes through a shortcut, and some hydrogen or oxygen will permeate through the membrane.

A schematic of the various processes that occur as a result of the permeation is provided in Figure 1.5. Even if the external current is 0, namely, under open circuit conditions, internal short-circuiting current exists since the membrane has the character of electronic conductivity supported by electrolyte [29]. In addition, the gas (H_2 or O_2) which permeates through the membrane will lead to the generation of crossover currents. As the H_2 permeates from anode to cathode, the possible oxidation pathway is chemical, electrochemical, or both. However, the thermodynamic potential of the cathode is much higher (~1.0 V) than for anode, thus greatly enhancing the possibility of the electrochemical pathway [97]. Therefore, the HOR at the cathode offer electrons to the ORR even under open circuit conditions.

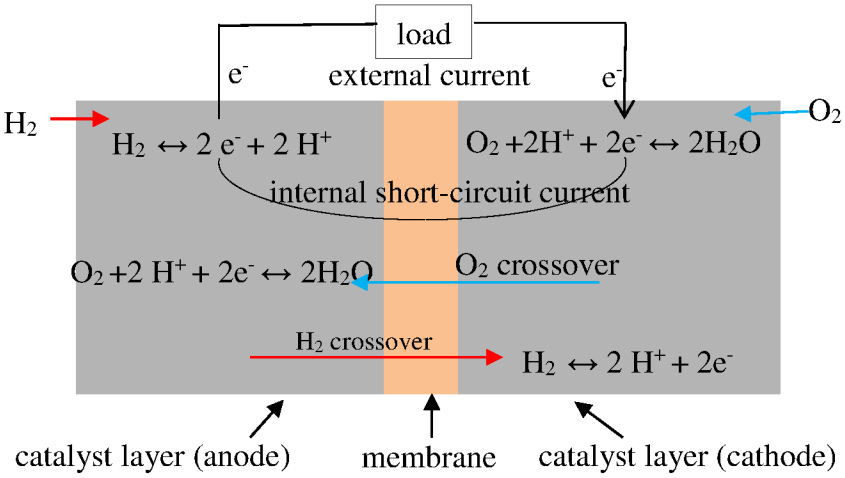

Figure 1.5. The schematic diagram of the electrode reactions and resulting current (external current, internal gas crossover and short-circuit current).

Moreover, Vilekar et al. [6] has estimated the effect of gas permeation on OCV in PEFC by a simple model. As a result, the crossover current caused by oxygen permeation nearly has no effect on over potential of anode. They state that the internal short-circuit current is much smaller than the H_2 crossover current. Therefore, hydrogen crossover entirely accounts for the observed potential loss under open-circuit conditions.

Generally, hydrogen crossover may cause the reduction of fuel efficiency, the depression of cathode potential and the formation of aggressive peroxide radical [98-100]. When the fuel cell is operated under open-circuit or very low current density conditions, these losses may have a marked effect on the cell potential [29, 31, 101, 102]. In addition, hydrogen crossover demotes

the efficiency and durability of a fuel cell. For example, the hydrogen crossover may cause a local hot spot, resulting in pinholes, and then leading to membrane degradation, which inversely causes a severe hydrogen crossover, and finally forms a vicious circle [9, 103]. Hydrogen crossover may not only cause membrane degradation, but also catalyst degradation when hydrogen peroxide generates on the cathode [99, 103]. Besides, the hydrogen crossover process can be affected by the membrane structure [104] and operating conditions [65, 99, 100, 104, 105] of fuel cells due to the diffusion process.

Researchers always evaluate the hydrogen crossover by the H_2 crossover rate. Many methods can be used to get the H_2 crossover rate. For instance, the gas crossover rate can be measured in a form with mass transfer limited current using in-situ electrochemical measurement. A number of techniques can be used to measure hydrogen crossover of PEFC, in particular, in-situ measurements, such as volumetric method, gas chromatography, CV, mass spectrometry and LSV. Of all in-situ methods mentioned above in measuring hydrogen crossover current, LSV is the simplest and the most efficient one [106]. Using this technique, the hydrogen crossover of various membranes has been investigated, such as, Nafion [97, 107-109], Nafion-palladium [107], sulfonated poly(ether ether ketone) (SPEEK) [110], and Flemion [111]. The current obtained from LSV measurement ($I_{cross\ H2}$) can be used to calculate hydrogen crossoveorate ($J_{crossH2}$), as shown in Equation 1.14 [98]. Where n means the electron number of H_2 oxidation (= 2), F is Faraday constant (A s mol^{-1}), and A serve as the MEA active area (cm^2).

$$J_{\mathrm{crossH2}} = \frac{I_{\mathrm{crossH2}}}{\mathrm{n\ F\ A}} \tag{1.14}$$

It was reported that the water content of the membrane [107] and gas pressure [99] has a significant influence on the hydrogen crossover rate. Cheng et al. [98] proposes that the hydrogen permeability coefficient increases effectively with increasing temperature, whatever the backpressure and RH are. Moreover, increasing backpressure causes increasing of the hydrogen permeability coefficient in relation to differing RH. Additionally, the effect of temperature on the hydrogen crossover is larger than that for backpressure or RH. Inaba et al. [99] states that under atmospheric pressure, the hydrogen crossover current was about 0.8 mA cm^{-2} at 80 °C, and gas crossover increased with increasing factors (temperature, hydrogen gas

pressure and relative humidity). Laraminie and Dicks [29] suggest that hydrogen crossover sustains a “internal current”, about 2 mA, which results in an over voltage of around 0.3 V.

1.4 The goal of this work

In the literature noted above, the mechanism of platinum surface oxidation is investigated as a function of potential. In the case of the OCV of PEFC, the potential results from the kinetics of the surface reaction. Then the kinetics of surface oxidation can be derived by observing the open circuit potential as a function of time. In order to separate the effects of Pt surface oxidation, carbon oxidation and hydrogen crossover, the OCV of PEM fuel cell and the OCP of half-cell is studied in this thesis.

Chapter 2 Methodology and instruments

As shown in chapter 1, the OCV of fuel cells is affected by the mixed potential and hydrogen crossover. In order to study OCV thoroughly, half-cell and single cell experiments are applied. A part of this work has been published [46].

2.1 The half-cell of 'glass cell -1' experiments

2.1.1 The equipment and preparation

A special three-electrode cell [112] was designed at the IEK-3 (Forschungszentrum Juelich) that gives good gas tightness from room temperature (RT) to higher temperature (max. 80 ℃ used in this work), as shown in the Figure 2.1. In this thesis, this half-cell is called 'glass cell-1'.

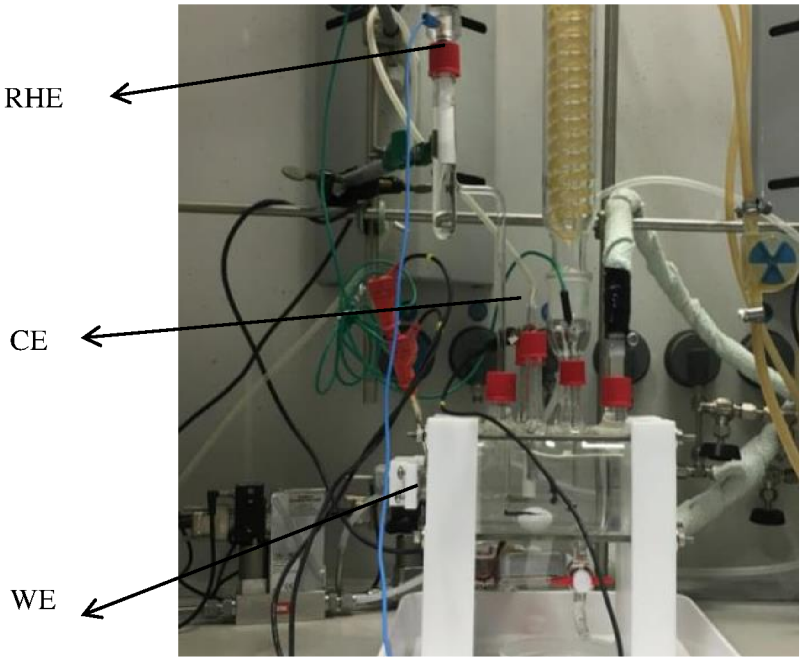

Figure 2.1. The 'glass cell-1' equipment.

A platinum disk with a size of 25 mm × 25 mm × 0.5 mm was used as the working electrode. The effective area is 2.54 cm^2. Prior to each measurement, the platinum disk was polished with

alumina paste (Buehler) with a particle size of 5, 1 and 0.05 μm, respectively. Then the specimen was cleaned with ethanol and distilled water in an ultrasonic cleaner for 15 min respectively, and finally dried with a high-pressure air flow [113].

As the reference electrode (RE), a reversible hydrogen electrode RHE (HydroFlex, Gaskatel GmbH) was employed, and a platinum mesh served as the counter electrode (CE).

The 98 wt.% H_2SO_4 and 70% $HClO_4$ was diluted by using ultrapure water for the preparation of 0.001, 1 and 6 M sulfuric acid electrolytes, and 1 M perchloric acid electrolytes, respectively. High purity of nitrogen (99.999%), oxygen (99.9991%), air (99.999%) and hydrogen (99.999%) were used.

2.1.2 The electrochemical measurement

Before the measurement, the cell was purged in 165 ml 1 M (or 0.001 M, 6 M) sulfuric acidic electrolytes (or 1 M perchloric acid electrolyte) for 60 min with N_2 at 100 ml min^{-1} gas flow rate. The specimen was connected to the Autolab potentiostat PGSTAT302N (Metrohm). To guarantee a homogeneous gas environment, the bulk electrolyte was stirred with a magnetic stirrer during gas purging period. Gas purging and the magnetic stirring were stopped during measurement.

In order to obtain clean surfaces and reproducible crystal orientation conditions of the polycrystalline platinum disk, the working electrode was electrochemically cleaned by cyclic voltammetry in the potential range between 0.05 V and 1.2 V for eight cycles with a scan rate of 50 mV s^{-1}.

After being heated to the expected temperature, the gas was switched to O_2 for 60 minutes at 100 ml min^{-1} gas flow rate, and the CV on the potential range of 0.05 and 1.2 V at 50 mV s^{-1} was implemented. Then, LSV was performed in the cathodic direction from 1.1 V to 0.4 V, immediately followed by OCP recording using chronopotentiometry. In this thesis, the temperature from 30 °C to 80 °C has been tested. The OCP of platinum inside N_2 and air are monitored, too. All measurements were repeated several times in order to illustrate the good reproducibility of the values. Figure 2.2 (a) and 2.2 (b) are schematic diagrams of the steps of OCP measurement with O_2 or air saturation and with N_2 saturation. The experimental results will be shown in chapter 3. All potentials in this thesis are related to the reversible hydrogen electrode. Further, the data presented are not iR corrected.

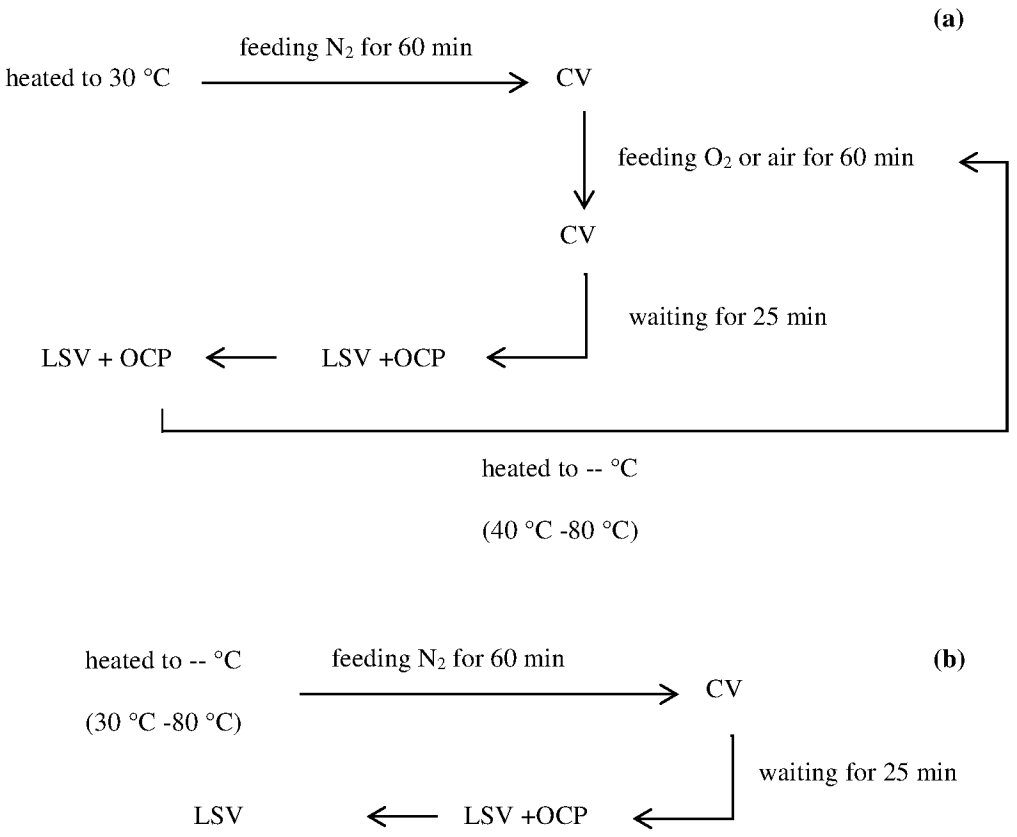

Figure 2.2. The schematic diagram of the steps of OCP measurement (a) with O_2 or air saturation and (b) with N_2 saturation.

2.2 The half-cell of 'glass cell-2' experiment

2.2.1 The equipment and preparation

Considering the limit (boundary issues) of 'glass cell-1' on the applying Pt/C catalyst, another three-electrode cell provided by the 'PINE' company, was improved at the IEK-3 (Forschungszentrum Juelich) which is suitable for the use of rotating disc electrodes, as shown in the Figure 2.3. In this thesis, we named this half-cell 'glass cell-2'.

A 5 mm diameter platinum or glassy carbon disk embedded in a PEEK shroud (Pine Instruments) was used as working electrode. The geometric area is 0.196 cm^2. Prior to measurement, the disk electrode was polished with albumin's paste (Buehler) with a particle size of 1, 0.3 and 0.05 μm, respectively, if a scratch was seen. Then it was cleaned with ethanol and

distilled water in an ultrasonic cleaner for 15 min respectively, and finally dried with a high-pressure air flow [113].

The working electrode (Pt or glassy carbon disk) is purged into electrolyte without rotating. The exposed area of the tested sample is 0.196 cm^2. As reference electrode, a reversible hydrogen electrode (HydroFlex, Gaskatel GmbH) was employed, while a platinum mesh served as the counter electrode.

The 98 wt. % H_2SO_4 was diluted by using ultrapure water for the preparation of 1 M acid electrolytes. High purity of nitrogen (99.999%), oxygen (99.9991%), air (99.999%) and hydrogen (99.999%) were used.

The catalyst of Pt/C (or C) on the glassy carbon disk is prepared by the following methods.

By casting catalyst-containing inks on glassy carbon electrodes, high quality catalyst films can be obtained. The catalysts are well-dispersed inks including water, alcohol and Nafion ionomer. The ink recipes vary with the catalyst types. A small amount of Nafion ionomer is added to either the mixed solution of water and alcohol to improve adhesion of the film to the electrode surface.

The following is a good recipe for a thin-film electrode of 20% Pt on Vulcan carbon with Pt loading of 20 μg_{Pt} cm^{-2}. The recipe comes from Garsany's group [113]. It involves mixing 20 ml of isopropanol with 79.6 ml of nanopure water and 0.4 ml of 5 wt. % Nafion ionomer solution (Ion Power, Liquion 1100) at first. This is followed by measuring 10 mg of the catalyst into a 10ml borosilicate vial and adding 5 ml of the stock isopropanol/ Nafion solution. The mixed solution is stirred for one minute using a high shear mixer (IKA, T10Basic S1). Finally, the ink is transferred to an ultrasonicator (Branson, 2510) and sonicated for 60 minutes in a water bath temperature 40 °C [113].

A droplet of 10 µl ink was placed onto the prepared glassy carbon electrode, completely covering the glassy carbon without connecting the Teflon. At last, the electrode was dried under a slow flow of N_2 at room temperature in a covered beaker.

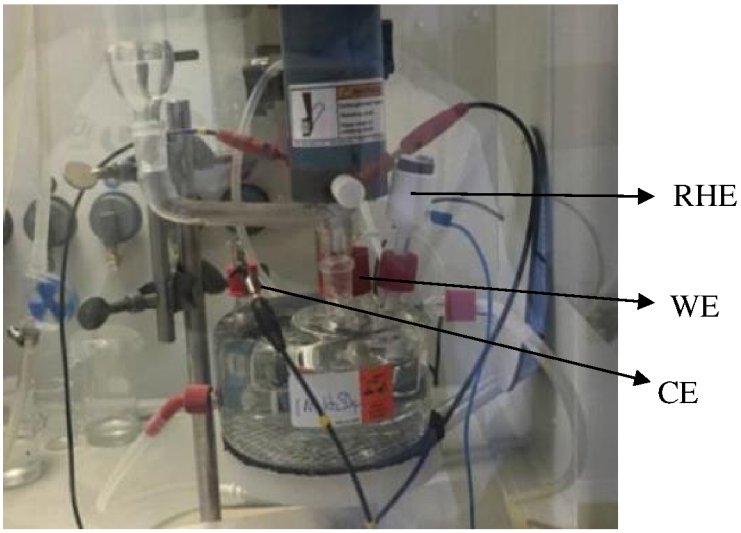

Figure 2.3. The 'glass cell-2' equipment.

Three different ratios of Pt on Vulcan carbon are used in this chapter. Their Pt ratios are 20%, 46% and 60%. The amount of inks using in this chapter is always 10 µl. In addition, for the catalyst of $Pt/C_{60\%\ Pt}$, the films of different platinum loading are studied, being 20, 60 and 120 $\mu g_{Pt}\ cm^{-2}$.

2.2.2 Electrochemical measurement

The cell was purged in N_2 for 30 min at the gas flow rate of 100 ml min^{-1}, and the cell was connected to the Autolab potentiostat PGSTAT302N (Metrohm). In order to obtain surfaces and reproducible crystal orientation conditions of the polycrystalline platinum disk, the working electrode was electrochemically cleaned by cyclic voltammetry in the potential range between 0.05 V and 1.2 V for eight cycles with a scan rate of 50 mV s^{-1}. Afterward, switching the gas to O_2 for 30 minutes at 100 ml min^{-1} gas flow rate, a CV on the potential range of 0.05 and 1.2 V at 50 mV s^{-1} was implement again. Finally, LSV was performed in the cathodic direction from 1.1 to 0.4 V, immediately followed by OCP record.

The difference of the OCP measurement process in this part from that of 'glass cell' is that the gas saturation time is 30 minutes.

All measurements were repeated several times in order to illustrate the good reproducibility of the values. Figure 2.4 (a) and 2.4 (b) is a schematic diagram of the steps of OCP measurement with O_2 or air saturation and with N_2 saturation. The experiment results will be shown in chapter

4. As mentioned before, the presented data are related to the reversible hydrogen electrode. Further, the data are not iR corrected.

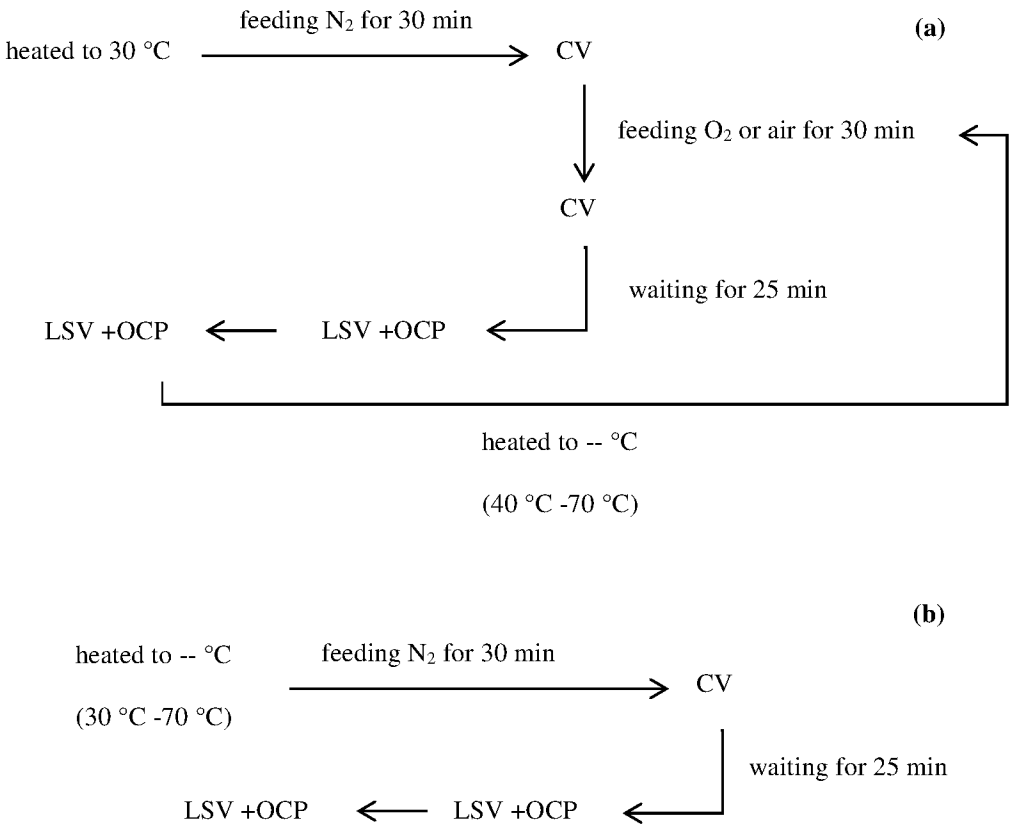

Figure 2.4. The schematic diagram of the steps of OCP measurement with (a) O_2 or air saturation and (b) N_2 saturation.

2.3 The single cell experiment

2.3.1 The equipment and its assembly

A special single cell was used, which is called Baltic quickCONNECTfixture (qCf). It is made up of the support frame pressure unit (SFPU) and cell fixture (cf), as shown in the Figure 2.5.

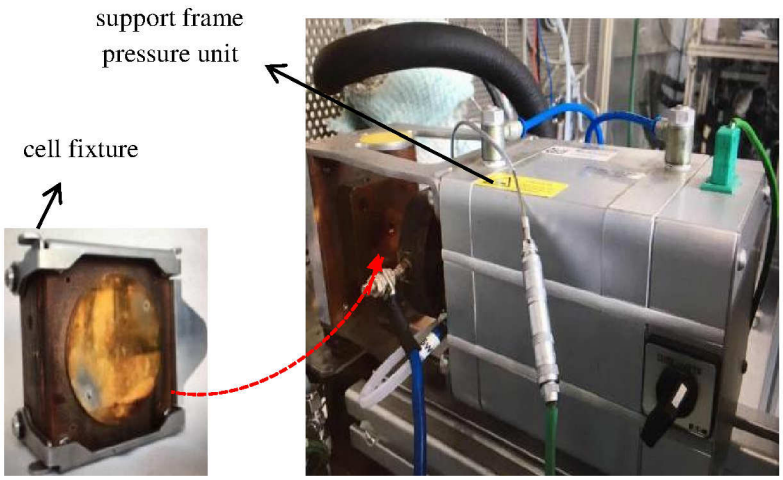

Figure 2.5. The single cell equipment.

In this thesis, a graphite-based bipolar plate was used. It has a serpentine flow field developed at Forschungszentrum Juelich with an active area of 25 cm^2. It is made of PPS material (Graphite & Polyphenylenesulfide) from the Eisenhuth company. It was cleaned with water and isopropanol and dried with compressed air before being assembled in the Baltic module.

After assembly with the MEA, the cell was fixed on the test station, and then compressed by 3 bar. The MEA includes a commercial catalyst coated membrane (CCM) from GORE company, which has a platinum loading of 0.4 mg cm^{-2} for the cathode and a 15 µm reinforced PFSA membrane, and two commercial carbon layers of H2315 CX165 from Freudenberg company.

High purity of nitrogen (99.999%), oxygen (99.9991%), air (99.999%) and hydrogen (99.999%) were used.

2.3.2 Electrochemical measurement

The test station used in this thesis is assembled in IEK-3, which consists of a data acquisition system, electronic load, mass flow controllers, LabVIEW software and the Baltic module. And the Autolab potentiostat PGSTAT302N (Metrohm) is employed on the cycle voltammetry, linear sweeping voltammetry, OCV and EIS measurement.

Before the measurement, a break-in process is necessary, which makes our cell achieve a stable condition. The cells were operated at 80 °C under 1, 0.7 and 0 A cm^{-2} current control for 1 h. The cycle is repeated 5 times and followed 0.5 A cm^{-2} current control for 16 h.

(1) Polarization curve

The polarization curve is the most frequently used method to examine the performance of the fuel cell, due to its convenience of measurement and analysis. The curve, describing the voltage decrease with increasing current density, can be divided into three parts: activation, ohm and concentration. They respond to the reaction rate loss, resistance loss and transport loss, separately [31, 114].

In this thesis, the current was stepped from zero up to the maximum test current density with an increment between 50 and 100 mA cm^{-2}. The time spent at each current density was 1 min when measuring polarization curves. Moreover, it is obtained before and after the measurement for one condition on each day.

(2) OCV measurement

For the OCV measurement, the OCV is recorded after a potential of 0.7 V for 5 minutes under O_2/air saturation. This process is a little different from that of the half-cell, which uses a linear sweeping voltammetry from 1.1 V to 0.4 V. This is because of the current limitation of our Autolab potentiostat PGSTAT302N (Metrohm). Thus, a potential of 0.7 V for 5 minutes is used to realize the catalyst surface reduction.

(3) EIS and LSV measurement

Depending on the research objectives, in situ impedance measurement is a good tool [115-117] [115, 118-120] for analysis of a single fuel cell or a fuel cell stack. Linear sweeping voltammetry (LSV) is a good method [65, 121-123] to measure the hydrogen crossover current. In my thesis, I use the EIS added LSV measurement to study the hydrogen crossover. Below I give some information on why and how to use them.

Following the EIS and LSV, the over potential (η_C) of ORR caused by hydrogen crossover can be calculated by Equation 2.1. The j_C is the crossover over current density obtained from LSV measurement. R_{CT} is the charge transfer resistance got from EIS results. A is the area of cell, equal to 25 cm^2.

$$\eta_C = j_C R_{CT} A \tag{2.1}$$

Considering the requirement of the comparison of charge transfer resistance and apparent exchange current density in chapter 6, their relationship is shown in Equation 2.2 [124]. The R and F is the gas constant and Faraday's constant, respectively. z is the number of electrons involved.

$$R_{CT} = \frac{RT}{zFj^0_{O_2}} \tag{2.2}$$

The impedance is measured at OCV condition in the range of 100 KHZ - 0.01 HZ for two kinds of cathode gas feeding, air and O_2. The linear sweeping voltammetry is swept from OCV to 0.6 V under N_2 condition at the rate of 1 mV / s.

(4) CV measurement

The CV on the potential range of 0.05 and 1.2 V at 50 mV s^{-1} was carried out under N_2 saturation also. The period during 0.05 - 0.4 V is the normal range of calculating the electrochemical surface area (ESA). A classical method supplied by Dhiman's group [125] is given in Equation 2.3, as below.

$$\text{ESA} = \frac{Q}{[Pt]C} \tag{2.3}$$

Where ESA is the electrochemical surface area [m^2 g^{-1}], Q is the average charge for hydrogen adsorption and desorption [in C], [Pt] is the platinum loading [in g] and C is a constant, which is defined as the charge required to oxidize a monolayer of atomic hydrogen on a Pt catalyst (C= 2.1 C m^{-2}).

As the relative humidity of both sides is 100%, the temperature at 40 °C, 60 °C and 80 °C is applied in this part. Additionally, the 50% and 75% relative humidity of cathode side is researched at 60 °C. The operational steps for each condition are shown in Figure 2.6.

Measurement results will be given in chapter 5. The data presented are not iR corrected.

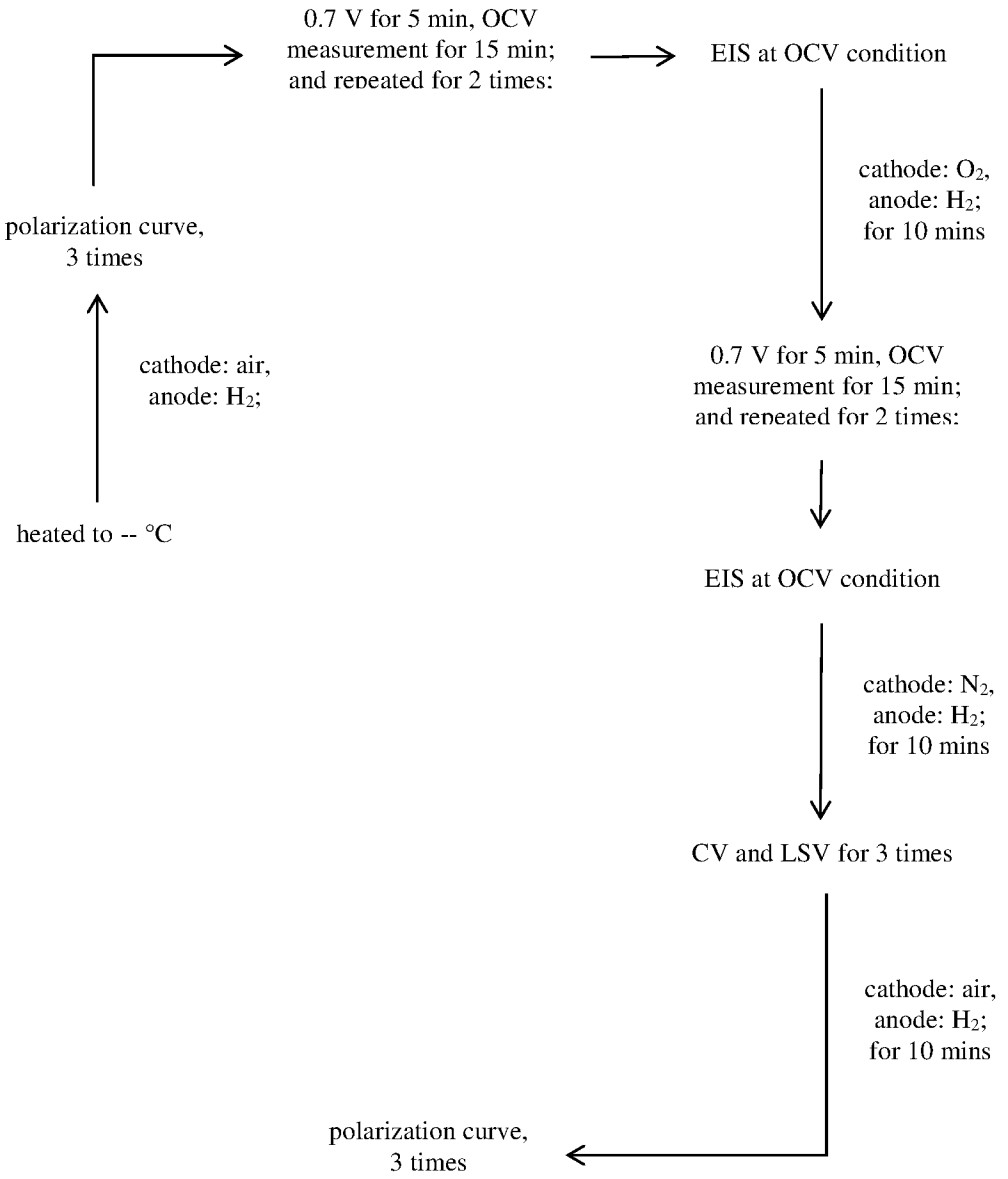

Figure 2.6. The schematic diagram of the electrochemical measurement steps of a single cell.

2.4 The calculation theory

In this section, the calculation theory is given. It will be used to calculate the OCV results which will be shown in chapter 3.

2.4.1 The calculation of H_2 and O_2 reaction to form water

Equation 2.4 is the reaction in which hydrogen reacts with oxygen to form water. According to the Nernst Equation, the cell potential can be written as Equation 2.5, in which the p_i/p^0 can be written by X_i compared with the classical Nernst Equation.

$$0.5\ O_2 + H_2 \rightleftharpoons H_2O \tag{2.4}$$

$$E_{H2O}(T) = E^0_{H2O}(T) - \frac{RT}{2F}(\ lnX_{H2O} - lnX_{H2} - 0.5\ lnX_{O2}) \tag{2.5}$$

The $E^0_{H2O}(T)$ is the standard potential of the Equation 2.4. It is a function of temperature. We can calculate it by the Equation 2.6 and 2.7 [126].

$$E^0(T) = \frac{-\Delta G^0(T)}{nF} \tag{2.6}$$

$$\Delta G^0(T) = a \cdot T - b \tag{2.7}$$

F is the Faraday constant, 9.64853399×10^4 C mol^{-1}, which is the number of coulombs per mole of electrons; n is the number of moles of electrons transferred in the cell reaction or half-reaction. $\Delta G^0(T)$ is the standard Gibbs energy, which is a function of temperature. For the liquid water, the constant of a and b equals to 160.778 J mol^{-1} K^{-1} and 284972 J mol^{-1} within the range of 298 K to 500 K, respectively. Table 2.1 illustrates the calculated value of ΔG^0 and E^0 from 298.15 K to 353.15 K.

Table 2.1. Calculated values for ΔG^0 and E^0.

T/K	303.15	313.15	323.15	333.15	343.15	353.15
ΔG^0/ J mol^{-1}	-236232	-234624	-233017	-231409	-229801	-228193
E^0/V	1.224	1.216	1.208	1.200	1.191	1.183

As for the mole fraction of hydrogen and oxygen, there are two models used in this thesis. One takes into account the gas concentration in the gas phase, which is marked as gas concentration model, and the other takes into account the gas concentration in the electrolyte according to the gas solubility [46], which is marked as gas solubility model below.

The gas concentration needs to be corrected by the equilibrium water vapor content because of the existence of liquid water. The equilibrium water vapor pressure can be calculated by the Antoine Equation 2.8. Then, the mole fraction of oxygen and hydrogen are acquired by Equation 2.9 and 2.10.

$$\log \mathrm{p} = 4.6543 - \frac{1435.264}{\mathrm{T} - 64.868} \tag{2.8}$$

$$\mathrm{X_{Vap}} = 10^{\log p} \cdot (105\ Pa)/(101325\ Pa) \tag{2.9}$$

$$\mathrm{X_{O2}} = 1 - \mathrm{X_{Vap}} \tag{2.10}$$

The solubility X_i of gas in solution can be calculated by the Equation (2.11) [127], which neglects the influence of the acid type.

$$\ln \mathrm{X_i} = \mathrm{A} + \frac{\mathrm{B}}{\mathrm{T^*}} + \mathrm{C} \cdot \ln \mathrm{T^*} \tag{2.11}$$

Here, $\mathrm{T^*} = \frac{\mathrm{T}}{100\mathrm{K}}$. The equation can be used up to 353 K. The constant, A, B and C are different for different gases. The value for the gas of O_2 and air is given, as shown in Table 2.2.

Table 2.2. The constant A, B and C [127].

	A	**B**	**C**
O_2	-66.7354	87.4755	24.4526
Air	48.1611	55.2845	16.8893

Figure 2.7 shows these two kinds of calculation results when the cathode is O_2. Obviously, the cell potential calculated by the gas concentration model is much higher than that calculated by

the model taking into account the gas solubility. Furthermore, both of them decrease with increasing temperatures. The decreasing degree of the former ones is smaller than that of latter ones. Considering the experimental value from literature, the cell potential calculated by the gas solubility model is closer to the real conditions.

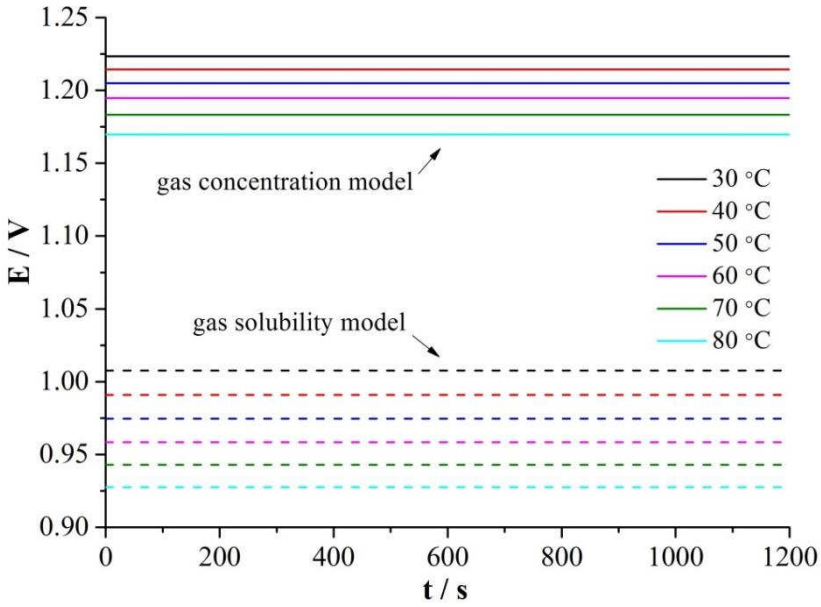

Figure 2.7. The calculating results from 30 °C to 80 °C by gas concentration model (solid line) and gas solubility model (dashed line).

2.4.2 The calculation of platinum surface oxidation

According to the information given in chapter 1, we know the platinum oxidation is a stepwise process. According to CV results, the cathode reaction on the surface of the electrode is not only the oxygen reduction (Equation 2.12) but also the oxidation of Pt. In order to simply describe this process, we condense them into one total process [46]. Since less parameters are better, the Equation 2.13 is picked up, which comes from the suggestions of Hoare et al. [68].

$$0.5\ O_2 + 2H^+ + 2e^- \rightleftharpoons H_2O \tag{2.12}$$

$$PtO + 2H^+ + 2e^- \rightleftharpoons Pt + H_2O \tag{2.13}$$

$$H_2 \rightleftharpoons 2H^+ + 2e^- \tag{2.14}$$

Adding the anode reaction of Equation 2.14, the Nernst equation of the reaction of platinum itself (Equation 2.15) and the reaction that hydrogen reacts with oxygen to form water (Equation 2.4) is displayed in Equation 2.16 and 2.5, separately.

$$PtO + H_2 \rightleftharpoons Pt + H_2O \tag{2.15}$$

$$E_{PtO}(T) = E^0_{H2O}(T) - E^0_{PtO}(T) - \frac{RT}{2F}(\ln X_{Pt} + \ln X_{H2O} - \ln X_{PtO} - \ln X_{H2}) \tag{2.16}$$

The $E^0_{PtO}(T)$ is a function of temperature, which was not clear up to now. Considering this and since these two reactions actually are difficult to divide into two separate entities, Equation 2.5 and 2.16 can be combined together, and a new equation (Equation 2.17) including both of these two reactions can be written.

$$E_{OCV}(T) = E^0_{H2O}(T) - E^0_{mix}(T) + \frac{RT}{2F}(\ln X_{PtO} + \ln X_{H2} + 0.5 \ln X_{O2}) \tag{2.17}$$

The calculation method of $E^0_{H2O}(T)$ is given above, which could be calculated by the Equation 2.6 and 2.7. The responding parameters are shown in Table 2.1. There are two kinds of models to calculate the molar fraction of hydrogen and oxygen.

The only difficulty is the calculation of the molar fraction of PtO and Pt. Here, the molar fraction of PtO can be computed as the coverage of the electrode, which is equal to 0 and 1 at t=0 s and t approaches infinity, separately, as shown in Equation 2.19. It can be achieved by first order rate reaction, as shown in Equation 2.18. Here, k is the reaction rate, and t is time.

$$X_{PtO} = 1 - e^{-kt} \tag{2.18}$$

$$S = X_{PtO} \tag{2.19}$$

Combining Equation 2.17 and 2.18, the whole equation (Equation 2.20) [46] is obtained to fit the experimental value. The variable parameters are $E^{0}_{mix}(T)$ and k, which are influenced by temperature. The calculating results will be shown together with the experimental results in the following chapters.

$$E_{OCV}(T,\ t) = E^{0}_{H2O}(T) - E^{0}_{mix}(T) + \frac{RT}{2F}\left(\ln\left(1 - e^{-kt}\right) + \ln X_{H2} + 0.5\ \ln X_{O2}\right) \quad (2.20)$$

2.4.3 The calculation of carbon surface oxidation

According to the discussion in chapter 1, carbon oxidation is a stepwise process. In a view of CV results, the cathode reaction on the surface of the electrode is not only the oxygen reduction (Equation 2.12) but also the oxidation of carbon. In order to simply describe this process, they are connected into one process. Since less parameter is better, the cathode reaction of Equation 2.21 is picked up.

$$C\text{-}O_{ad} + 2H^{+} + 2e^{-} \rightleftharpoons C + H_2O \quad (2.21)$$

Adding the anode reaction of Equation 2.14, the Nernst equation of the total reaction of carbon itself and the reaction that hydrogen reacts with oxygen to form water (Equation 2.4) is displayed in Equation 2.22 and 2.5, separately.

$$E_{C\text{-}Oad}(T) = E^{0}_{H2O}(T) - E^{0}_{C\text{-}Oad}(T) - \frac{RT}{2F}(\ln X_{C} + \ln X_{H2O} - \ln X_{C\text{-}Oad} - \ln X_{H2}) \quad (2.22)$$

The $E^{0}_{C}(T)$ is a function of temperature, which has not been clear up to now. Considering this and since these two reactions are difficult to divide into two entities, Equation 2.5 and 2.22 can be combined and written to a new one (Equation 2.23) including both reactions.

$$E_{OCV}(T) = E^{0}_{H2O}(T) - E^{0}_{mix}(T) + \frac{RT}{2F}(\ln X_{C\text{-}Oad} + \ln X_{H2} + 0.5\ \ln X_{O2}) \quad (2.23)$$

The calculating method of $E^{0}_{H2O}(T)$ is given above, which could be calculated by the Equation 2.6 and 2.7. The responding parameters are shown in Table 2.1. There are two kinds of models to calculate the molar fraction of hydrogen and oxygen.

The calculation of the molar fraction of C-O_{ad} is the same to that of PtO, which is thought as the coverage of carbon oxide groups. It can be achieved by first order rate reaction, as shown in Equation 2.24 and 2.25. Here, k is the reaction rate, and t is time.

$$X_{C-Oad} = 1 - e^{-kt} \tag{2.24}$$

$$S = X_{C-Oad} \tag{2.25}$$

Combining Equation 2.23 and 2.24, the whole equation (Equation 2.26) is received, which can be used to fit the experimental value. The variable parameters are $E^{0}_{mix}(T)$ and k, which are influenced by temperature. The calculating results will be shown together with the experimental results in the following chapters.

$$E_{OCV}(T, t) = E^{0}_{H2O}(T) - E^{0}_{mix}(T) + \frac{RT}{2F}\left(\ln\left(1 - e^{-kt}\right) + \ln X_{H2} + 0.5 \ln X_{O2}\right) \tag{2.26}$$

2.4.4 The calculation of catalyst surface oxidation

Though the model above can be used both in the pure platinum and the carbon layer, it can also be used for the catalyst layer. The same method is used to calculate the coverage of oxide on the surface of catalyst layer.

2.4.5 The calculation of catalyst layer in single cell

It's known that the gas solubility/concentration has an effect on the OCV of fuel cells, which reflects on the single cell relative humidity (RH). Its effect on single cell will be shown in chapter 6, which requires the OCV results of half-cell on different RH. However, it can't be obtained for the half-cell. Therefore, the half-cell result is taken as the case of dry gas, and

calculating the results of other RH on this basis. Additionally, the mixed potential E_{mix} and the reaction rate constant, k, is thought of as constant.

According to the definition, relative humidity is the ratio of the partial pressure of water vapor in the mixture to the equilibrium vapor pressure of water at a given temperature, as shown in Equation 2.27.

$$RH = \frac{p_{H2O}}{p^*_{H20}} \tag{2.27}$$

Thus, the molar fraction of vapor water, X'_{Vap}, can be corrected as Equation 2.28. Where the X_{Vap} is obtained from Equation 2.9. And then, the corrected molar fraction of O_2 or hydrogen can be known from Equation 2.29. The subscript i represents the gas type.

$$\mathrm{X'_{Vap}} = \mathrm{X_{Vap}} \cdot \mathrm{RH} \tag{2.28}$$

$$\mathrm{X'_i} = 1 - \mathrm{X_{Vap}} \cdot \mathrm{RH} \tag{2.29}$$

Considering the gas solubility, the molar fraction of O_2 or hydrogen is corrected again by Equation 2.30, in which the X_i is calculated by Equation 2.11.

$$\mathrm{X''_i} = \mathrm{X'_i} \cdot \mathrm{X_i} \tag{2.30}$$

Chapter 3 Half-cell experiment with Pt disk

3.1 Introduction

In this chapter, the study on OCP of pure Pt is achieved by the half-cell equipment with a Pt disk. An easy way is used to explain the OCP and the influencing factors of it using cyclic voltammetry and added OCP measurement (LSV+OCP). A part of this work has been published [46].

3.2 Experiment

The electrochemical cell [112, 128] used in this chapter is 'glass cell-1', which is introduced in chapter 2. After pretreatment, the cell was assembled with 165 ml sulfuric acid (prepared from AR reagent). And then the cell was heated to the expected temperature, followed by the electrochemical measurement including CV, LSV and OCP tests.

3.3 Results and discussion

3.3.1 The electrochemical measurement

(1) Cyclic voltammetry linear scan

At first, an electrochemical cleaning procedure should be done. It can be carried out by feeding nitrogen for 60 minutes [50] and sweeping cyclic voltammetry linear scan in the range from 0.0 V to 1.2 V for several cycles at the scan rate of 100 mV s^{-1} [113]. Then the Pt electrochemical surface area determination can be calculated by CV measurements between 0.05 V and 1.20 V at the rate during 20 - 100 mV s^{-1}. The CV with N_2 saturation at the different sweeping rate is shown in Figure 3.1.

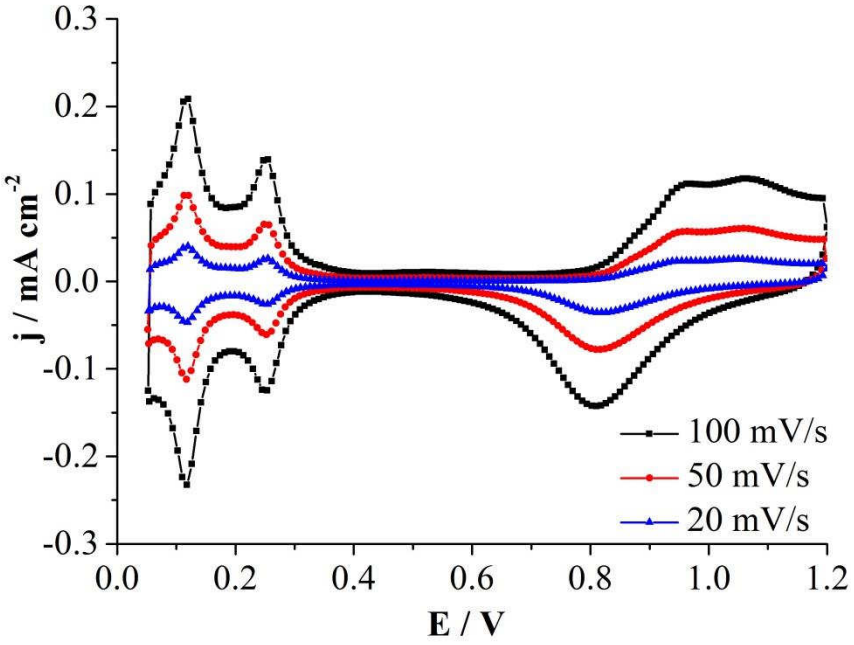

Figure 3.1. The CV of Pt with N_2 saturated in 1 M H_2SO_4 at 30 °C with the different sweeping rate.

In Figure 3.1, the CV is of similar shape at a different sweeping rate, although the intensity and potential position of the peak also differs. For CV at the rate of 50 mV s^{-1}, two obvious and symmetrical hydrogen adsorption and desorption peaks exist. The main voltammetry features of poly-platinum are the peaks at 0.115 V, which are related to (110)-type sites [2]. For the peak at 0.255 V, which is not observed as the main signal on the basal planes but on the stepped surfaces. This peak is the result of (100)-type sites [2]. The anodic peaks at 0.95 V and 1.06 V relates to Pt_2OH and PtOH on the surface of platinum, separately, and the negative peak at 0.81 V relates to the reduction of platinum oxide.

In summary, the CV of Figure 3.1 illustrates that a clean platinum electrode has been obtained. By calculating, the charge density for hydrogen adsorption of the electrode is 252.11 μC cm^{-2}, which is a little bigger than the minimum value (210 μC cm^{-2} [129]) of pure platinum. Considering the similar effect of different sweeping rate on the CV from 20 mV s^{-1} to 100 mV s^{-1}, the middle sweeping rate (50 mV s^{-1}) was chosen for subsequent experimentation.

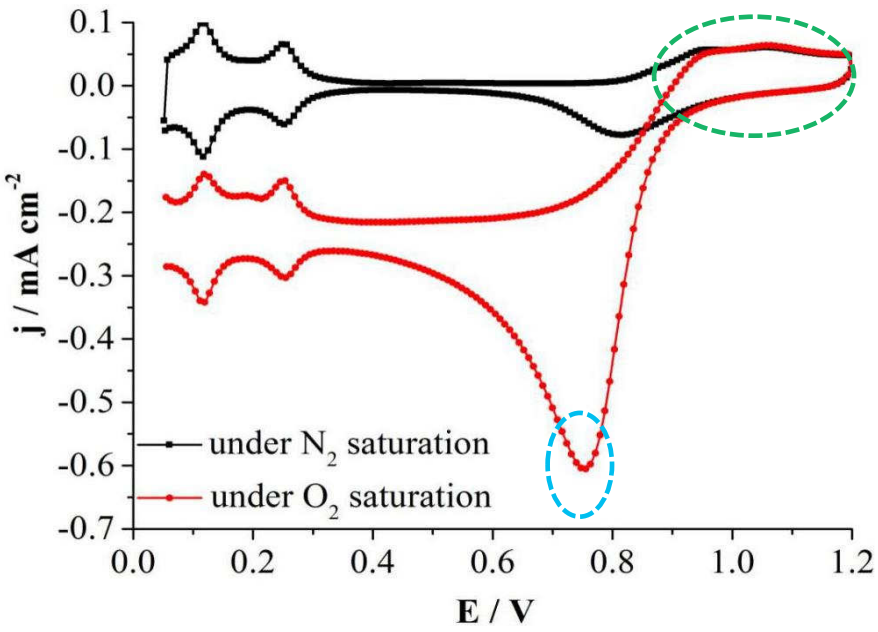

Figure 3.2. The CV of Pt with N_2 and O_2 saturation in 1 M H_2SO_4 at 30 °C at a sweeping rate of 50 mV s^{-1} [46].

After CV measurement with N_2 saturation, the gas was switched to O_2 for 60 minutes, and then a CV (0.05~1.2 V at 50 mV s^{-1}) was implemented. Figure 3.2 compares the CV with O_2 saturation and N_2 saturation.

The peaks of the CV with O_2 saturation have the same potential position to that with N_2 saturation, except for the slightly left shifted oxygen reduction peak (blue circle). The difference of the net current between CV under N_2 and O_2 condition is obvious. Compared with the CV with N_2 saturation, the CV with O_2 saturation can be described by two points: (1) the downshift of the double layer and hydrogen adsorption and desorption region; (2) the large increased oxygen reduction peak. The difference is caused by the oxygen reduction reaction, which starts slowly below 0.95 V, then increases quickly, and finally goes up to a steady state. There is a similar region above 0.95 V (green circle), which thus can be thought as the OCP region. Therefore, the Pt oxidation statement under N_2 saturation can be use in the region of CV under O_2 conditions.

(2) OCP measurement

In order to understand OCP well, an experiment was designed with O_2 saturation. The procedure of LSV (from 1.1 V to 0.4 V at 50 mV s^{-1}) and OCP were tested twice. And the time range of the OCP measurement is the same as the waiting time before LSV measurement.

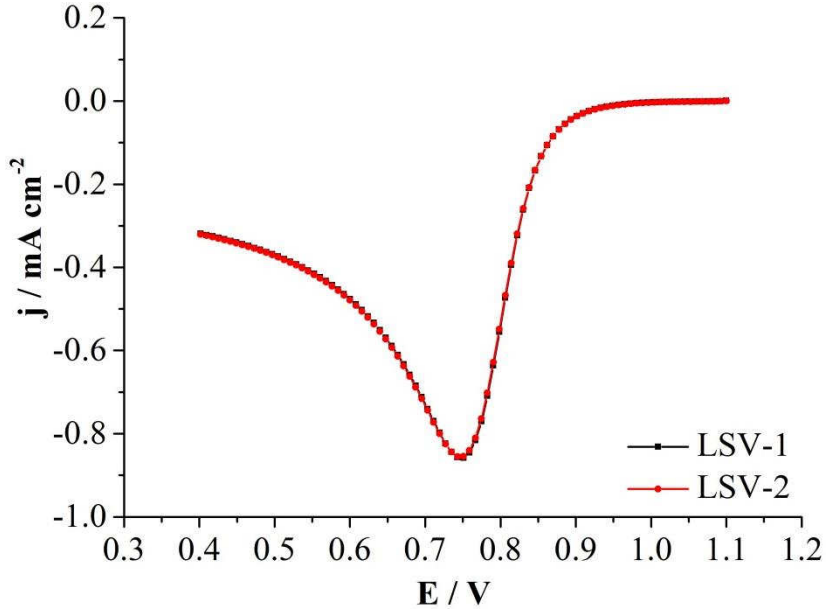

Figure 3.3. The LSV of platinum with O_2 saturation in 1 M H_2SO_4 at 30 °C at a sweeping rate of 50 mV s^{-1} between 1.1 V and 0.4 V [46].

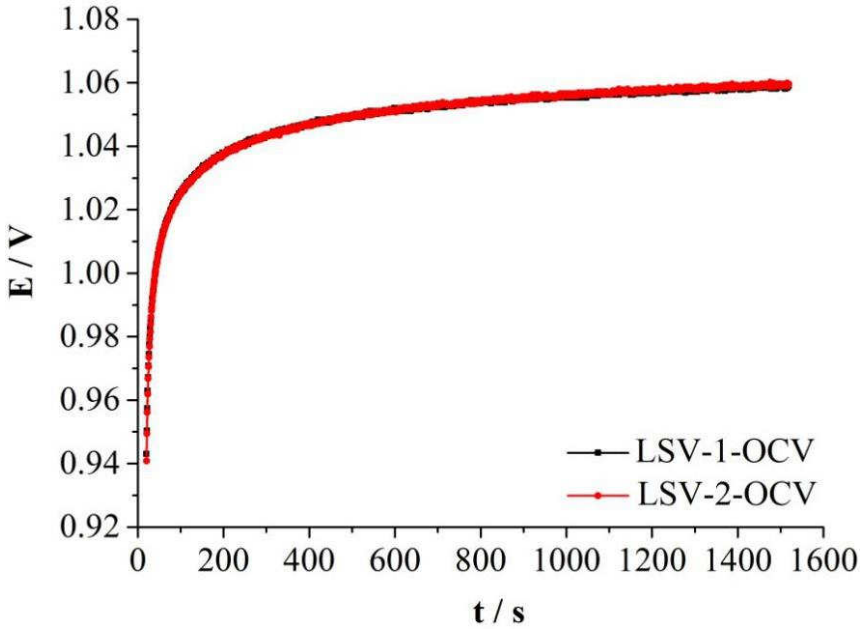

Figure 3.4. The t-E curve of platinum with O_2 saturation in 1 M H_2SO_4 at 30 °C under open circuit condition after performing LSV-1 and LSV-2 [46].

During this experiment, the same timing is kept for the cell on the open circuit condition before the repeated LSV measurement, and the same surface oxide degree of the platinum electrode is expected. This assumption supports that idea that the platinum electrode is on the same condition after LSV measurement. Accordingly, LSV from 1.1 V to 0.4 V was set, which can reduce the surface of platinum to a pure Pt condition. A 1500 s measurement was carried out by chronopotentiometry under open circuit condition. In this case, the graph of t-E after two LSV testings should be the same if the same LSV curve was obtained. This view is verified in the cell of 1 M H_2SO_4. Figure 3.3 and Figure 3.4 give an example of it at 30 °C.

It is known from Figure 3.4 that the voltage goes from a sharply increasing step to a slower transition, and finally up to a steady state. Contacting the platinum oxidation introduced in chapter 1, here we simplify this process into two steps. Step 1 is the oxidation of Pt to PtOH, and Step 2 is the further oxidation of PtOH to PtO_x species, respectively.

(3) The reproducibility

The OCP measurement of Pt in 1 M H_2SO_4 at 30 °C has been repeated several times, which is shown in Figure 3.5. The Figure 3.5 (a), (b) and (c) show several results under three identical preparation conditions, respectively. The OCP at 900 s is 1.050 ± 0.002 V, 1.044 ± 0.002 V and 1.046 ± 0.001 V under the same preparation method, respectively. The OCP at 900 s under three identical preparation conditions is 1.047 ± 0.004 V.

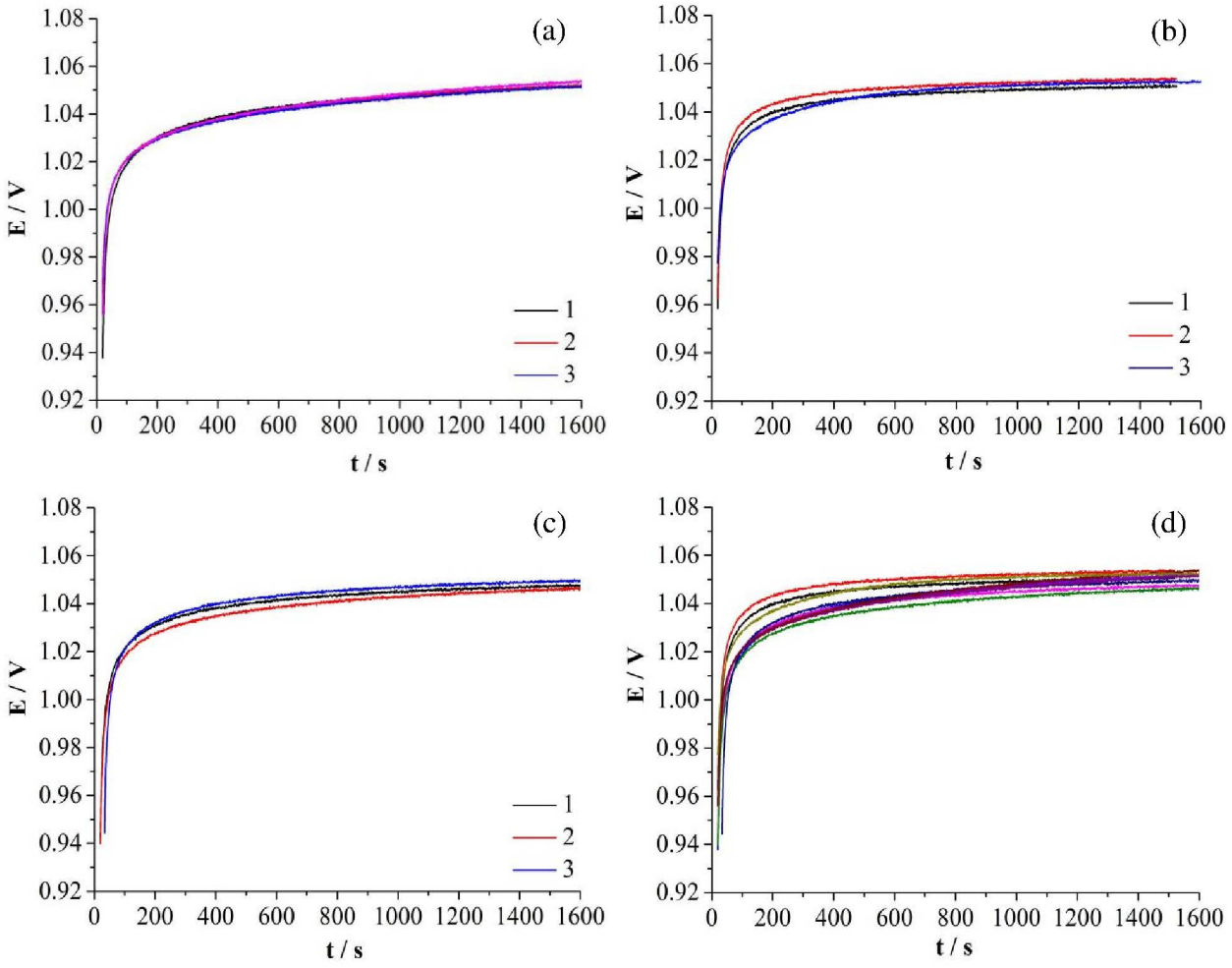

Figure 3.5. The t-E curve of platinum with O_2 saturation in 1 M H_2SO_4 at 30 °C under open circuit condition. The (a), (b) and (c) represents three identical preparation conditions. The 1, 2, and 3 in (a), (b) and (c) relate to three times repeated results. All the results are shown in (d).

3.3.2 The effect of temperature on OCP

According to the Nernst equation, with increasing temperature, the OCP value decreases. Thus, the effect of temperature in the range from 30 °C to 80 °C has been studied in this chapter. This range is just the normal operating temperature range of PEFC. When the cell is heated to a higher temperature, the measurement process is the same as that at 30 °C with O_2 saturation. Similar to the result at 30 °C, the identical LSV and OCP curve at each temperature has been obtained. Figure 3.6, 3.7 and Figure 3.8 shows the CV and one of the LSV and time vs OCP curve at different temperatures, respectively.

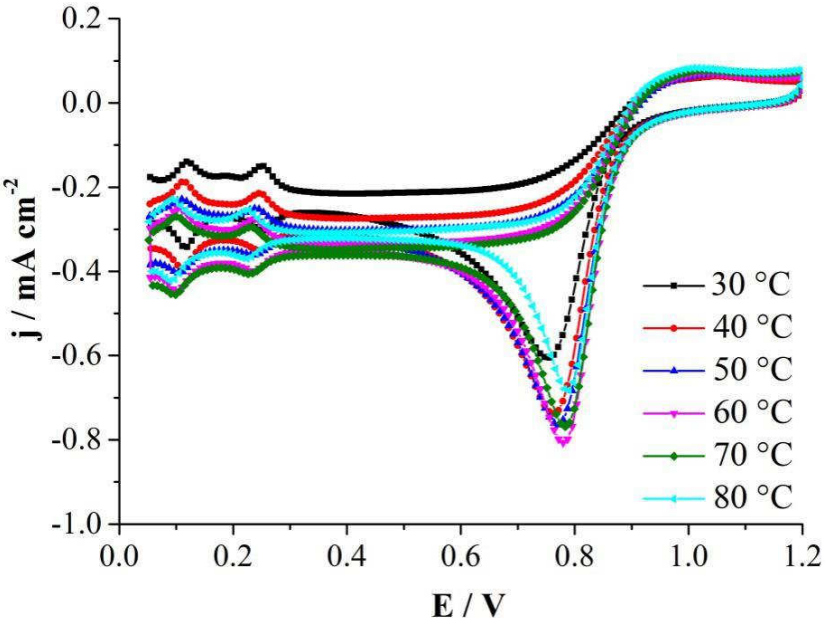

Figure 3.6. The CV of platinum with O_2 saturation in 1 M H_2SO_4 at different temperatures at a sweeping rate of 50 mV s^{-1}.

The LSV curves shown in graph 3.7 display that the intensity of the reduction peak decreases from 30 °C to 80 °C with a little right potential shift, especially at 70 °C and 80 °C. Namely, the reduction of Pt oxide groups become easier and the O_2 concentration in the electrolyte decreases from 30 °C to 80 °C.

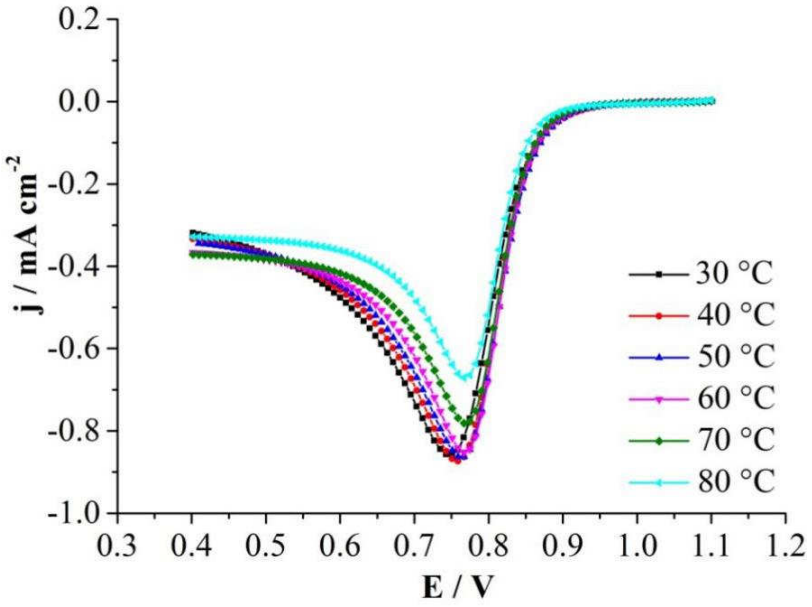

Figure 3.7. The LSV of platinum with O_2 saturation in 1 M H_2SO_4 at different temperatures at a sweeping rate of 50 mV s^{-1}.

Figure 3.8 gives the OCP from 30 °C to 80 °C. It's clear that the OCP, at 900 s, decreases with increasing temperature. This changing rule is consistent with the rule of the Nernst equation changing with temperature. Compared with the relatively stable value, at 900 s, with the Nernst equation, which is between 1.18 V and 1.23 V for gas phase and between 0.93 V and 1.01 V, if gas solubility is considered, our experimental value is close to the later one, as shown in Figure 3.9.

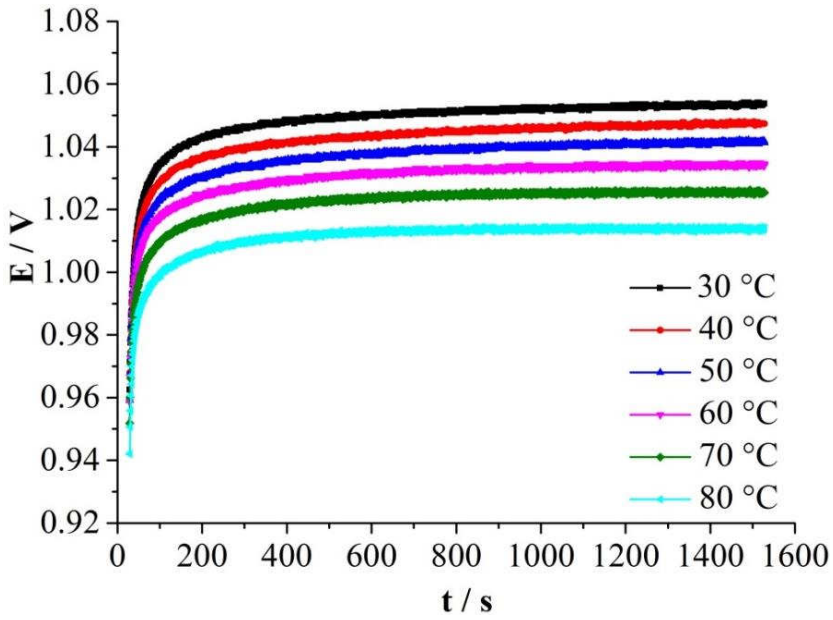

Figure 3.8. The t-E of platinum in 1 M H_2SO_4 with O_2 saturation at different temperatures at a sweeping rate of 50 mV s^{-1} [46].

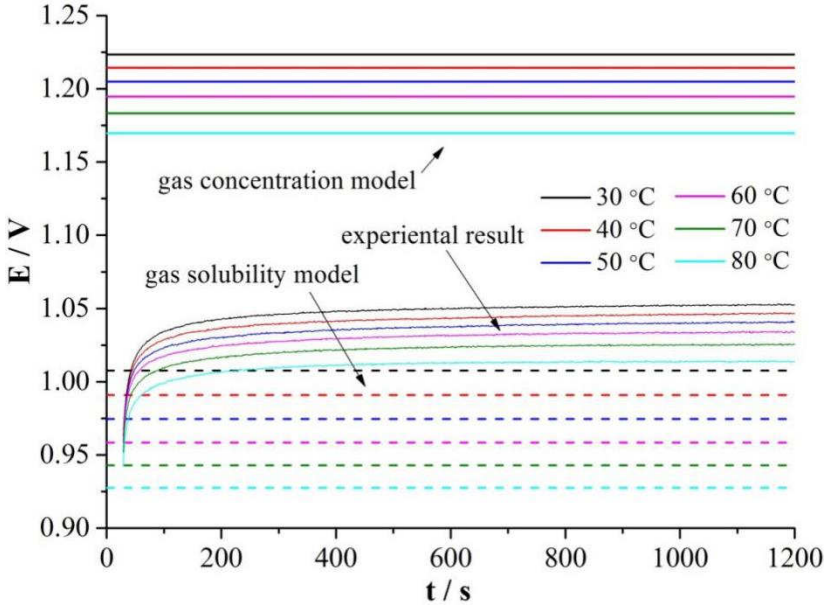

Figure 3.9. Comparison of theoretical Nernst potential for liquid water formation calculated with gas phase concentrations (upper part) and gas solubility (lower part), and the t-E of platinum in 1 M H_2SO_4 with O_2 saturation at different temperatures [46].

3.3.3 The effect of gas composition on OCP

Considering the results of Figure 3.9, the OCP at a temperature from 30 °C to 80 °C were measured and compared under different gas saturation. The gases are N_2, air, and O_2. For each group, the CV under N_2 saturation at 30 °C is obtained at first. The CV and OCP results are shown in Figure 3.10, Figure 3.11 and Figure 3.12. In Figure 3.11 (a), (b), (c) and Figure 3.12, the OCP under N_2, air, and O_2 at different temperature and their comparison at 30 °C are given separately.

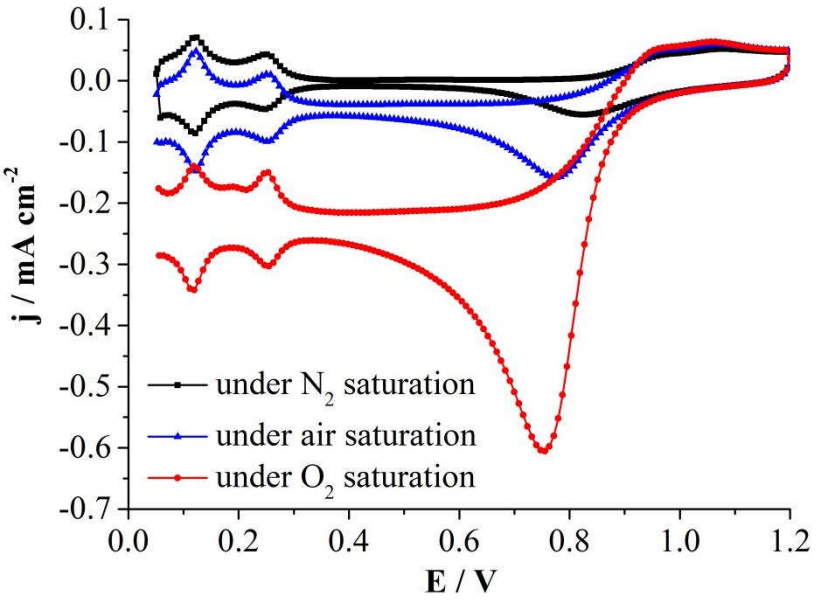

Figure 3.10. The CV of platinum in 1 M H_2SO_4 at 30 °C at a sweeping rate of 50 mV s^{-1}.

Comparing the CV under different conditions, the downshift of the net current under O_2 saturation is bigger than that under air saturation. This is thought of as the limit of O_2 reduction reaction, which has a relationship with the gas concentration. These results comply with the fact of the solubility concentration of oxygen.

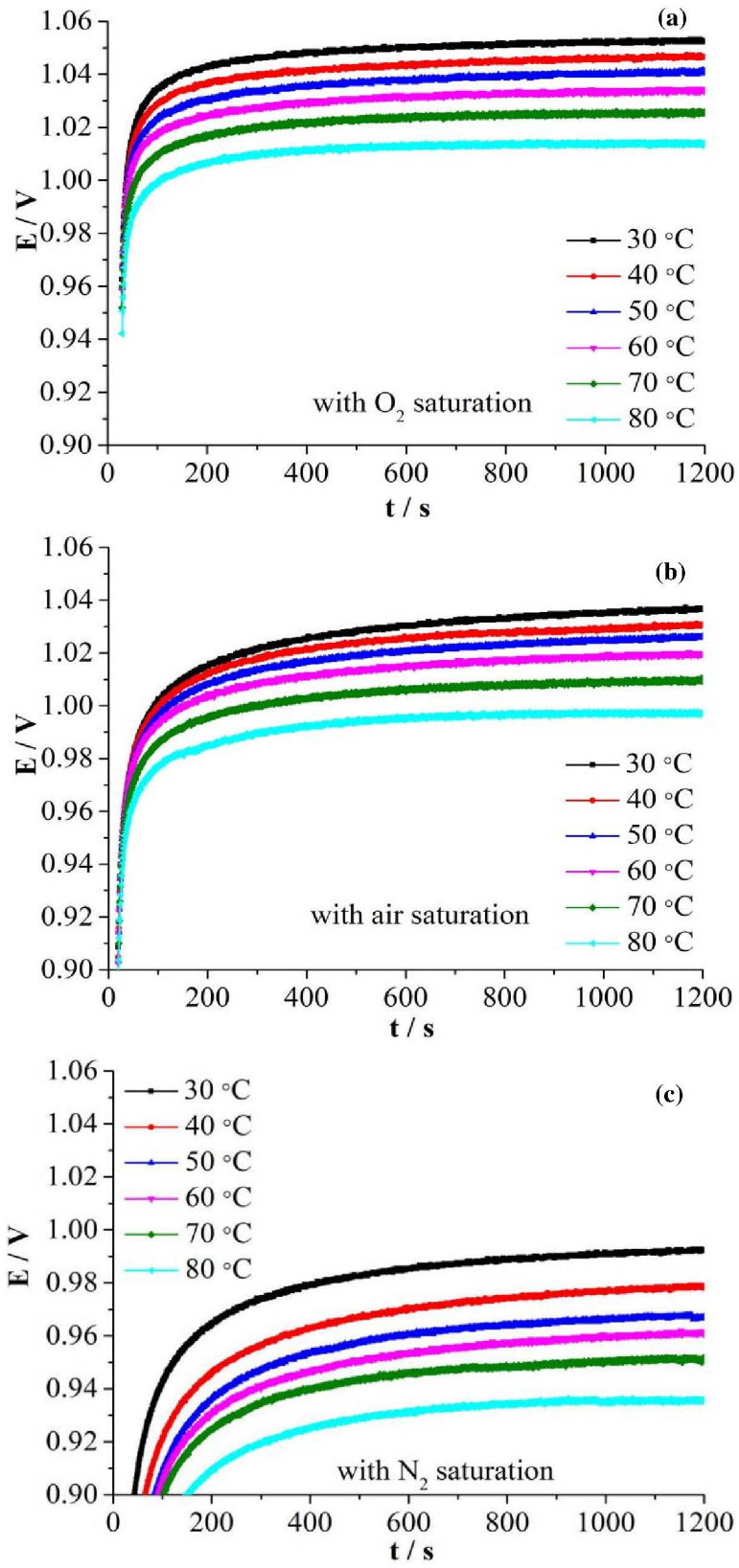

Figure 3.11. The t-E of platinum in 1 M H_2SO_4 with O_2 (a), air (b) and N_2 (c) saturation from 30 °C to 80 °C [46].

Obviously, the shape of the t-E curve obtained under all of the conditions is the same. The OCP value in slow reaction region decreases with increasing temperature within these three gas compositions. The OCP with O_2 saturation is higher than that with air saturation, which is higher than that with N_2 saturation. The speed of the oxidation becomes faster from N_2 saturation to air and then to O_2 saturation. The possibility is that the different surface oxide covered on the surface, and the higher the O_2 concentration is, the bigger the surface coverage will be.

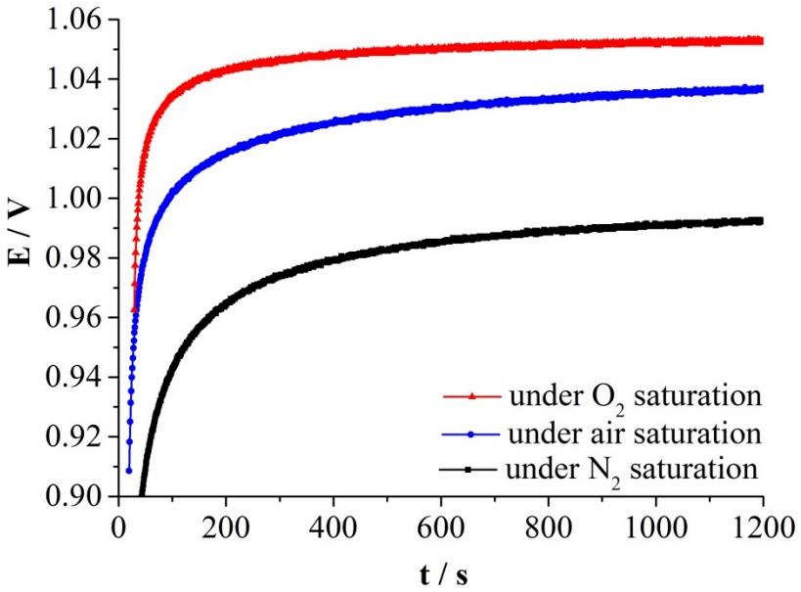

Figure 3.12. The t-E of platinum in 1 M H_2SO_4 with O_2, air and N_2 saturation at 30 °C.

According to the calculation shown in chapter 2 and the experimental results shown in Figure 3.11, the fitting results, which consider the gas solubility, are shown in Figure 3.13. The graph (a), (b) and (c) relates to the OCP with O_2, air, and N_2 saturation, respectively.

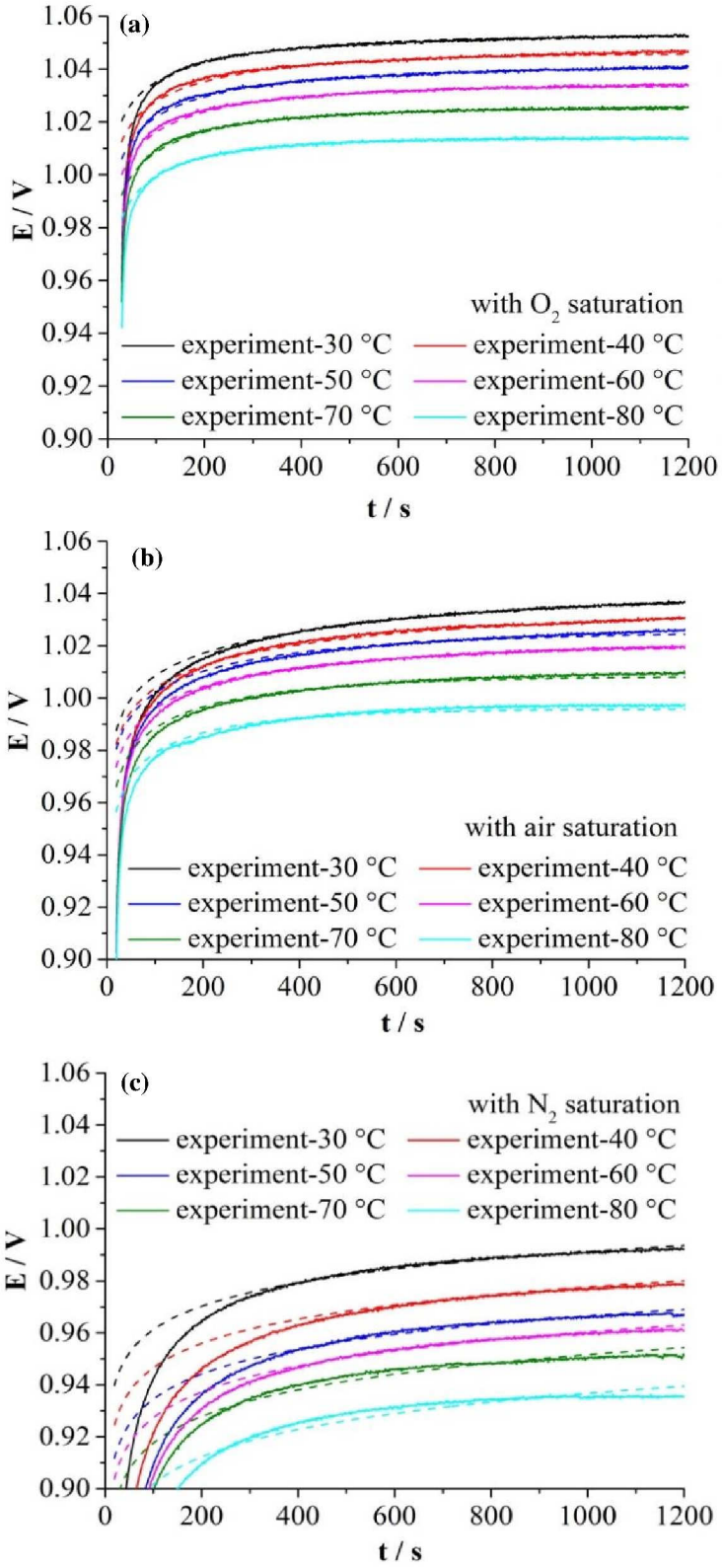

Figure 3.13. Fitting of t-E curve of platinum in 1 M H_2SO_4 with O_2 (a), air (b) and N_2 (c) saturation from 30 °C to 80 °C [46]. Solid line represent the experimental data, dashed line are simulated results.

Obviously, the model results fit well with the experimental OCP with O_2 and air saturation. However, it does not work for that with N_2 saturation. The fitting parameters, $E^0_{mix}(T)$ and k, are displayed in Figure 3.14. This figure shows the fitting results including two calculation models, gas concentration phase and gas solubility phase, which is introduced in chapter 2.

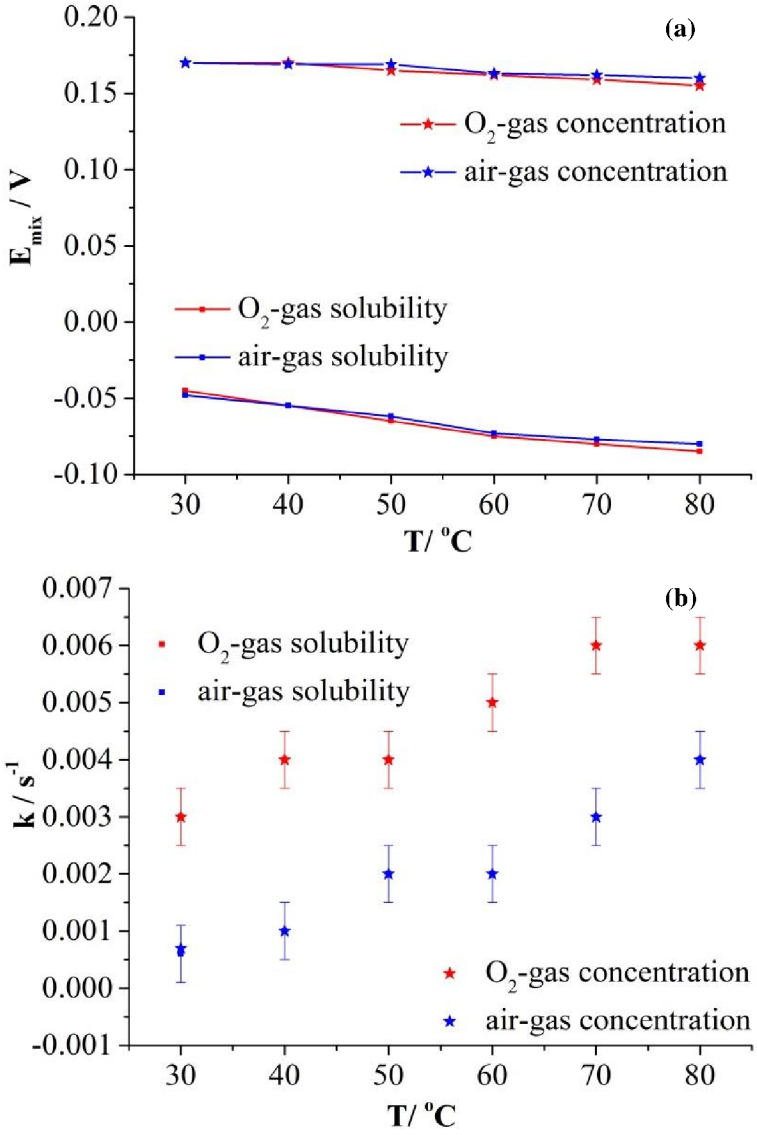

Figure 3.14. Fitting parameters $E^0_{mix}(T)$ (a) and k(T) (b) from 30 °C to 80 °C [46].

Both $E^0_{mix}(T)$ and k are a function of temperature. The $E^0_{mix}(T)$ with O_2 saturation is the same as that with air saturation and decreases with increasing temperature in both models. Additionally,

the $E^{0}_{mix}(T)$ in the calculating model of gas phase is higher than that in the case of gas solubility, and the difference between them is about 200 mV.

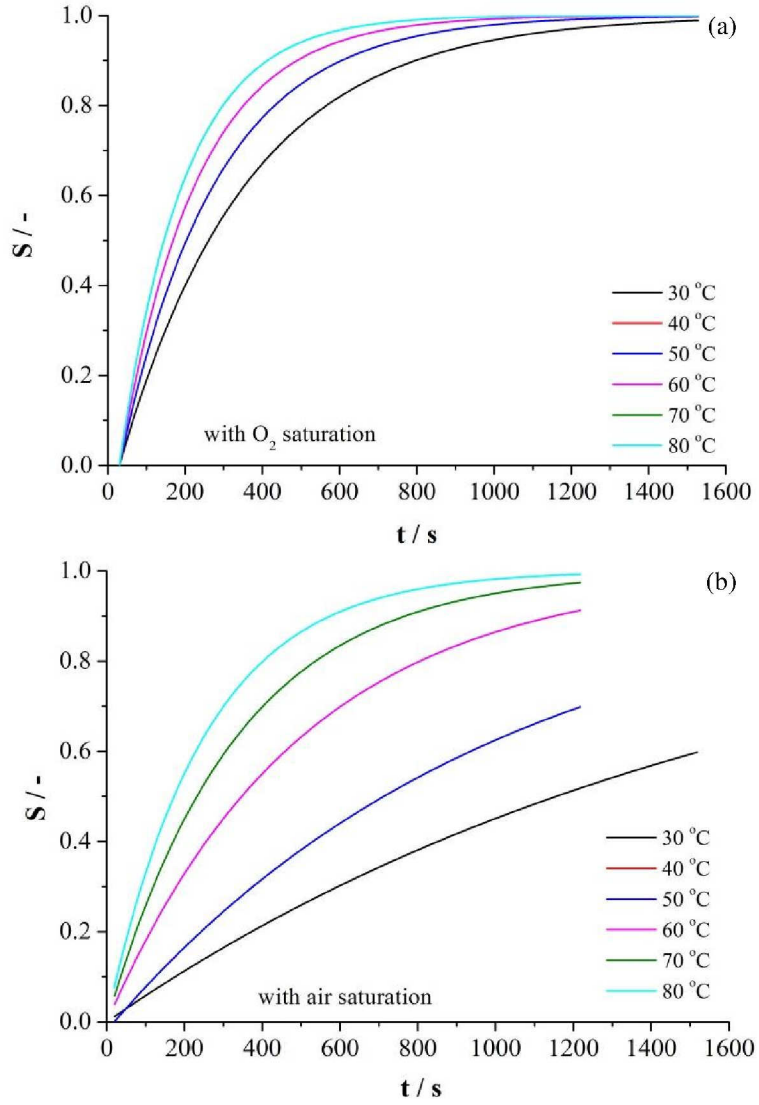

Figure 3.15. Surface coverage S as a function of time with O_2 (a) and air (b) saturation of the electrolyte at different temperatures.

For the reaction rate k, it is the same in both models of calculation. Namely, the absolute value of k does not depend on the model approach for the Nernst equation. It increases as temperature increases. From theory shown in chapter 2, k should be independent of concentration, while the k under O_2 saturation is higher than that under air saturation, as shown in Figure 3.14 (b). One of the possibilities is that the different surface oxide covered on the surface, and the higher the O_2

concentration, the bigger the surface coverage.

Additionally, the surface fraction of the oxidized platinum species can be calculated from the reaction rate according to Equation 2.19 on page 28. The surface fraction of PtO from 30 °C to 80 °C with O_2 and air saturation is shown in Figure 3.15. For both cases, the lowest value of S_{PtO} is at 30 °C and the highest value is at 80 °C. For oxygen, a comparably narrow range results and, after 900 s, the surface is almost completely oxidized. At T = 80 °C the surface becomes almost completely oxidized after 900 s, and even for the lowest temperature T = 30 °C, a surface fraction of 93% is reached at 900 s. For air, the temperature has a much stronger influence. The surface fraction of 97% is reached at 900 s at 80 °C, while only 0.42 is reached at 900 s at 30 °C.

From figure 3.13, it can be determined that after about three minutes, a fairly stable OCP value is reached. At this time, up to 36% of the surface is covered by oxidized species. This value is fairly close to the value of 0.35, which was obtained from an early experiment by Hoare et al. [68].

3.3.4 The effect of electrolyte concentration on OCP

In accordance with the Nernst equation shown above, temperature and oxygen solubility are the important factors affecting OCP. The gas solubility is affected by the temperature, the concentration and the type of the acid. Thus the effect of acid concentration on OCP is studied in this section by measuring the OCP of Pt in the concentration of 0.001 M, 1 M and 6 M H_2SO_4, which is prepared from 98 wt.% H_2SO_4. The same electrochemical measurement shown before is used in this work. The curve of CV and t-E are displayed in Figure 3.16, Figure 3.17 and Figure 3.18, separately.

Compared with the typical CV of 1 M H_2SO_4 with N_2 saturation, the CV of 0.001 M H_2SO_4 presents a typical CV curve of Pt, too, though there is a slightly right potential shift of the hydrogen adsorption and desorption. However, the CV of 6 M H_2SO_4 shows a slightly left potential shift of the hydrogen adsorption and desorption, and a different platinum oxidation region. In addition, the lower the pH, the larger the potential range of the double layer. Namely, the lower the concentration, the earlier the oxidation of Pt begins.

Comparing the CV of different concentrations of acid under O_2 condition, the downshift of double layer current of 0.001 M H_2SO_4 is bigger than that of 1 M H_2SO_4 , which is bigger than

that of 6 M H_2SO_4 . And compared to the CV of 6 M H_2SO_4, the CV of 1 M H_2SO_4 is closer to that of 0.001 M H_2SO_4. In summary, the lower the electrolyte concentration gets, the easier the O_2 reduction reaction becomes.

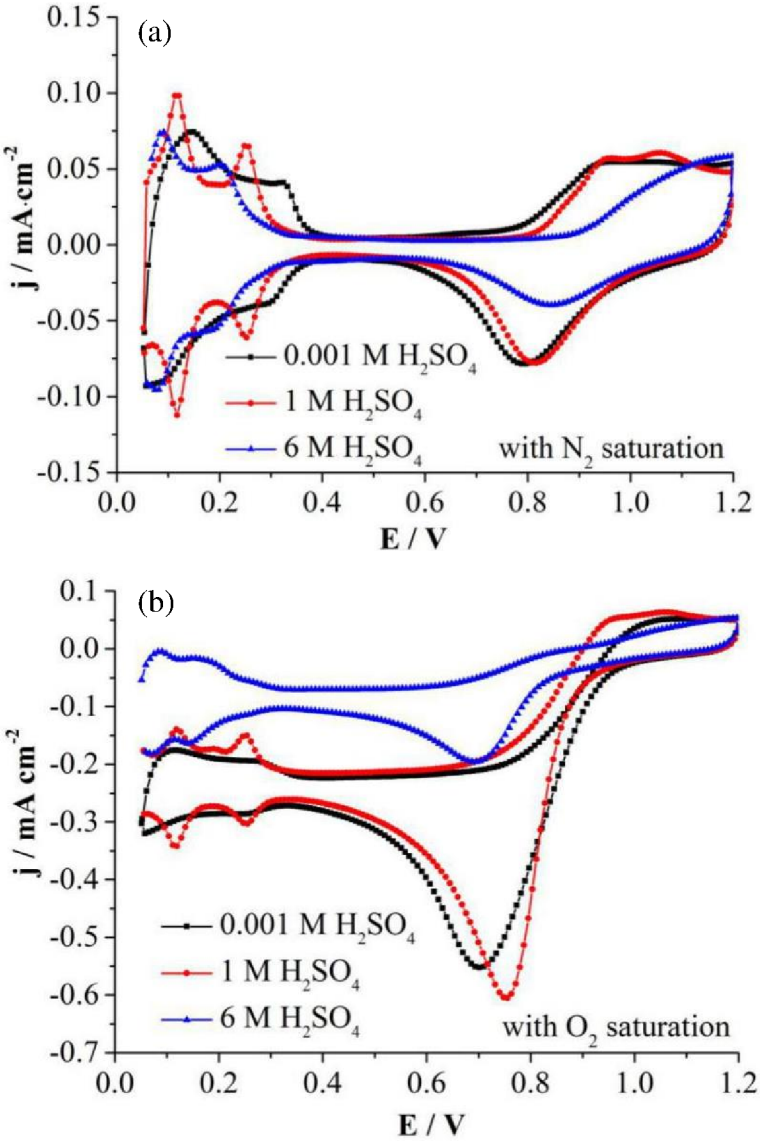

Figure 3.16. The CV of platinum in H_2SO_4 with N_2 (a) and O_2 (b) saturated at 30 °C at a rate of 50 mV s^{-1}.

Figure 3.17 gives the graph of t-E of different concentrations of sulfuric acid, separately. The (a), (b), (c) and (d) relate to the OCP of 0.001 M H_2SO_4, 1 M H_2SO_4, 6 M H_2SO_4 from 30 °C to 80 °C and their comparison at 30 °C.

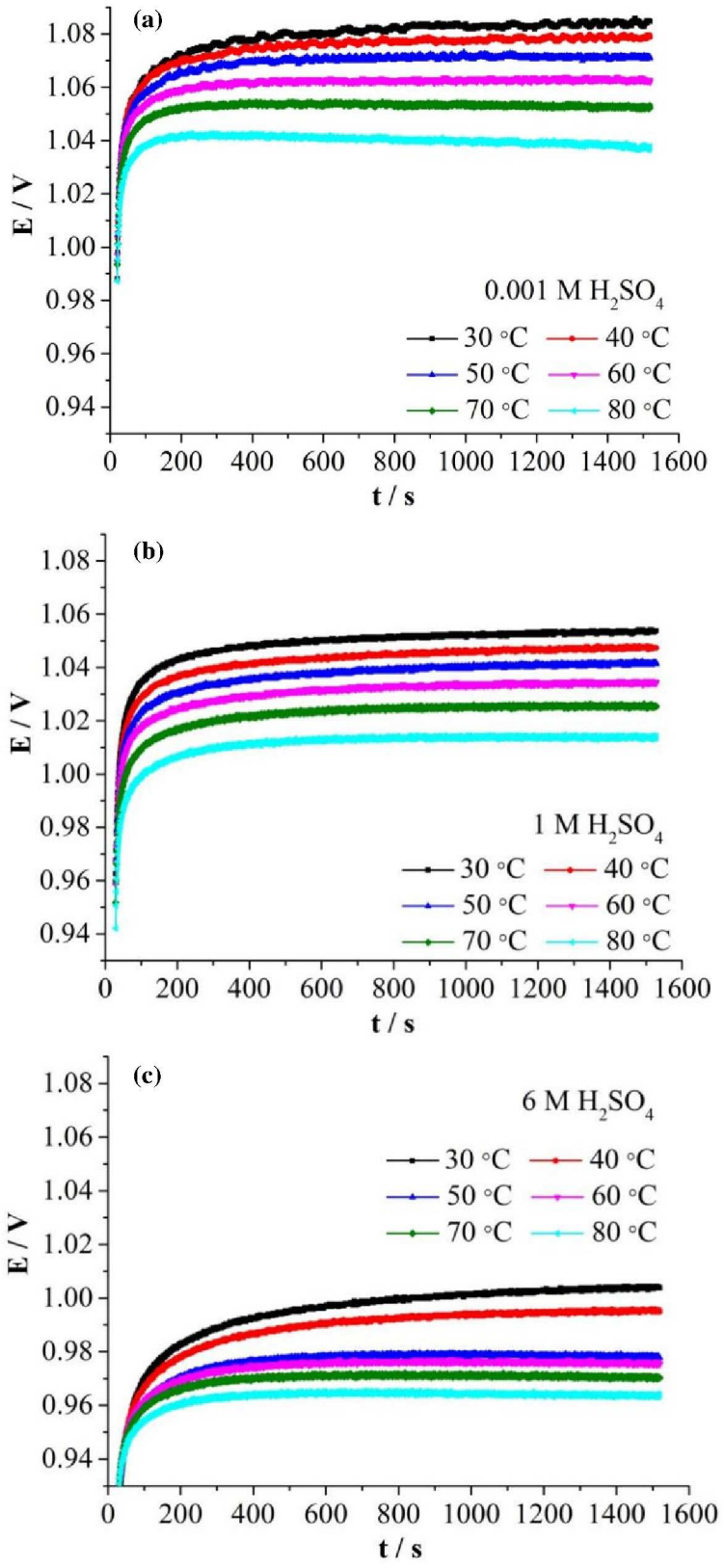

Figure 3.17. The t-E of platinum in 0.001 M (a), 1 M (b), 6 M (c) H_2SO_4 with O_2 saturation from 30 °C to 80 °C.

Obviously, the OCP type obtained under all of the conditions is the same. And the OCP value in slow reaction region decreases with increasing temperature within these three kinds of concentrations of sulfuric acid, and their decreasing value from 30 °C to 80 °C is different. For the condition under 0.001 M H_2SO_4 to 6 M H_2SO_4, the OCP becomes lower and lower, and the speed of the oxidation becomes slower and slower.

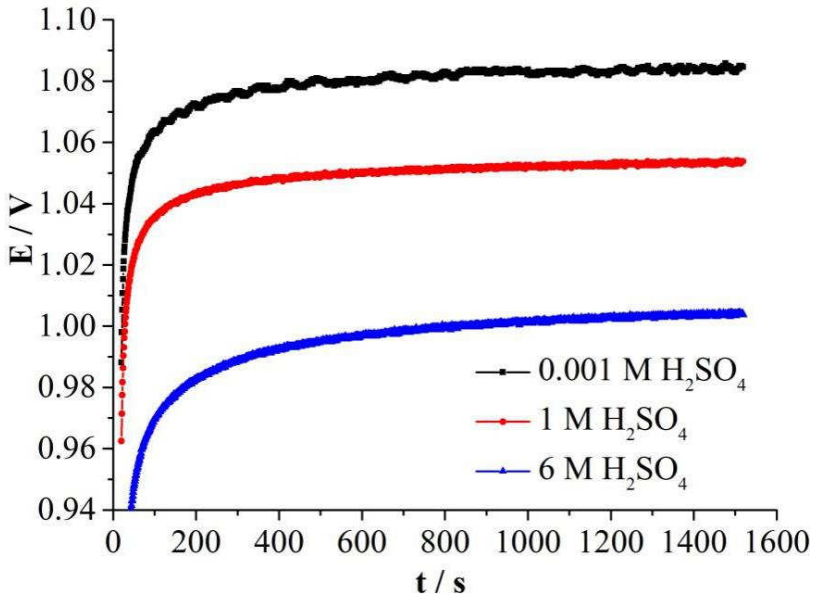

Figure 3.18. The t-E of platinum in 0.001 M , 1 M , 6 M H_2SO_4 with O_2 saturation at 30 °C.

According to this result, a fitting work is applied. The same method considering the gas solubility as above is used. In order to simplify the calculation, the data of gas solubility in water is used. And the variables at a certain temperature still are reaction rate (k) and mixed potential ($E^0_{mix}(T)$). The Figure 3.19 shows the good fitting results of the calculation and experiment results.

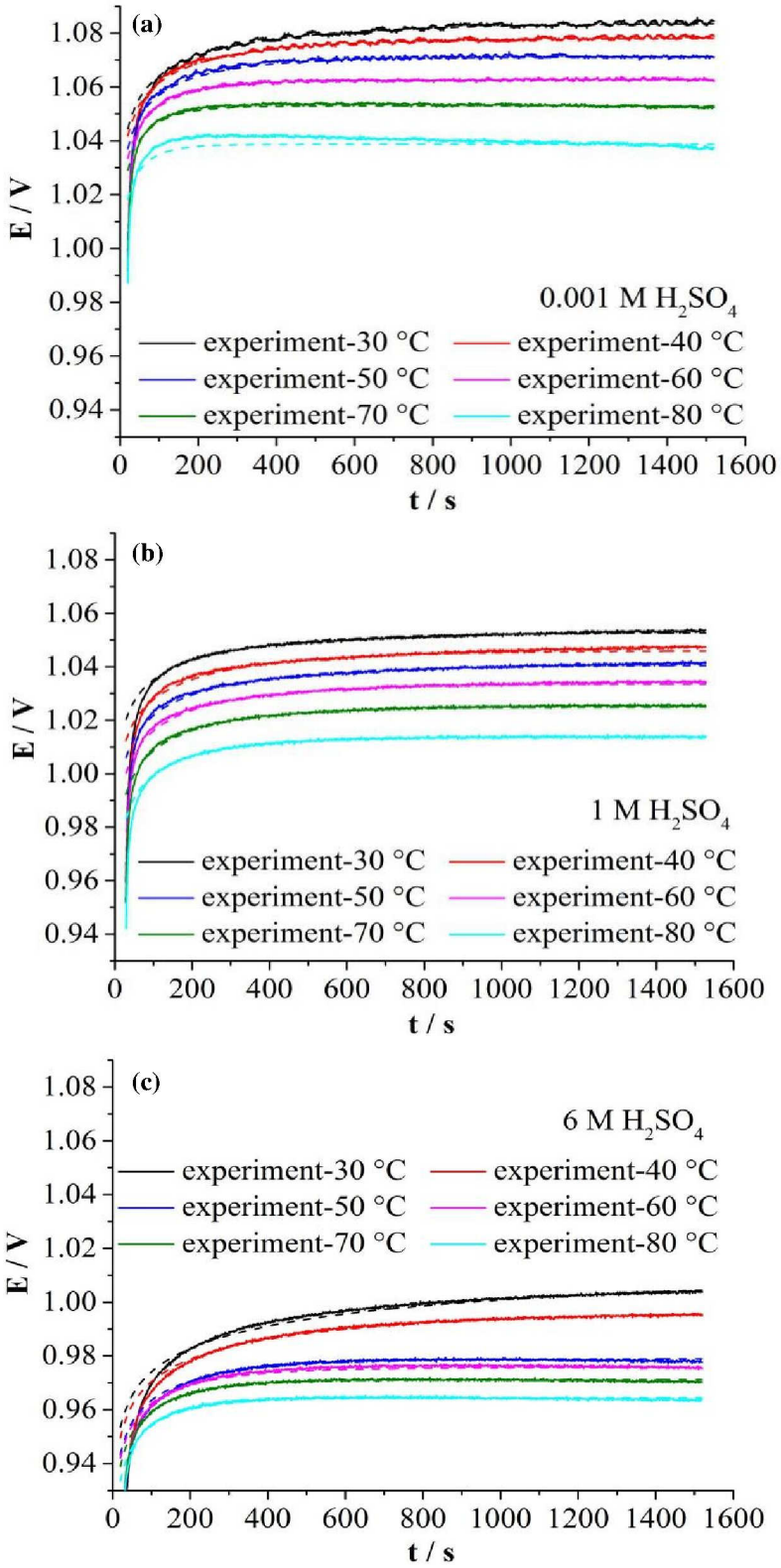

Figure 3.19. The t-E of platinum in 0.001 M H_2SO_4 (a), 1 M H_2SO_4 (b) and 6 M H_2SO_4 (c) with O_2 saturation from 30 °C to 80 °C. Solid lines represent the experimental data, dashed lines are the fitted simulation data.

The fitting results are shown in Figure 3.20. Whatever the concentration is, when the temperature increases, $E^{0}_{mix}(T)$ decreases, however, k increases. The lower the concentration is, the lower the $E^{0}_{mix}(T)$ will be. The slop of the k varying with temperature in 6 M H_2SO_4 is bigger than that in 1 M H_2SO_4 and smaller than that in 0.001 M H_2SO_4.

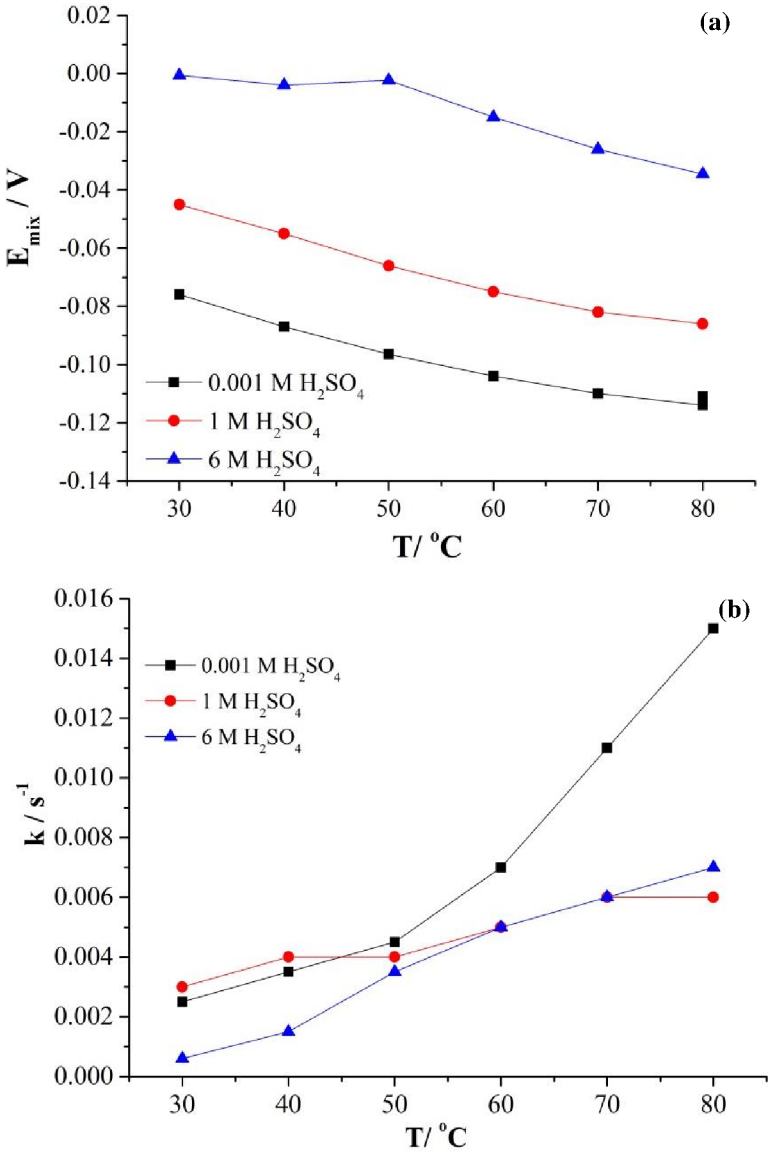

Figure 3.20. The fitting parameters $E^{0}_{mix}(T)$ (a) and k(T) (b) from 30 °C to 80 °C.

However, according to Nernst equation, the $E^{0}_{mix}(T)$ should be only a function of temperature, which has no relationship with acid concentration. Therefore, here, the calculation is corrected

by the effect of protons and gas solubility at different electrolyte concentrations on Nernst equation, as shown in Table 3.1. For gas solubility, the differences of its contribution to the Nernst equation at different electrolyte concentrations can be neglected, compared to the $E^0_{mix}(T)$ at different acid concentrations. The contribution of protons to the Nernst equation at different acid concentration is close to $E^0_{mix}(T)$. Thus, a possible reason is that the different $E^0_{mix}(T)$ at different acid concentration is a proton effect. This assumption is not consistent with the calculation model, as shown in Equation 2.4 and 2.15, in which the proton effect in the cathodic and anodic reactions have been offset by the total reactions. A probable explanation is that the proton amounts on both sides of the electrode of the cell are no longer the same following the surface oxidation of the platinum electrode on the cathode side.

Table 3.1. The contribution of gas solubility, $E^0_{mix}(T)$ and protons at 30 °C at different concentration on Nernst equation.

E/ V	Concentration / M		
	0.001	1	6
$(RT/NF)(\ln X_{H2}+0.5 \ln X_{O2})$	-0.108	-0.108	-0.108
$(RT/NF)(\ln X_{H2}+0.5 \ln X_{O2})$ corrected	-0.106	-0.108	-0.112
$E^0_{mix}(T)$	-0.076	-0.045	-0.001
$(RT/NF)(\ln X_{H+})$	-0.070	-0.026	-0.014

3.3.5 The effect of electrolyte type on OCP

As known, the gas solubility and Pt oxidation are affected not only by the temperature and the concentration, but also by the type of the electrolyte. In this section, the OCP of Pt in $HClO_4$ was examined. Figure 3.21 gives the CV of $HClO_4$ and the CV comparison of $HClO_4$ and H_2SO_4. The (a) and (b) relates to the CV comparison of Pt in 1 M H_2SO_4 and 1 M $HClO_4$ at 30 °C under N_2 and O_2 condition, and the CV of Pt in 1 M $HClO_4$ from30 °C to 80 °C under the O_2 condition, separately.

It can be seen, a normal typical CV of Pt in 1 M H_2SO_4 and 1 M $HClO_4$ under N_2 saturation at 30 °C is obtained. Compared with the CV in 1 M H_2SO_4, the hydrogen adsorption and desorption peak of the CV in 1 M $HClO_4$ is not so obvious, and the downshift of the double layer is bigger.

The CV in graph 3.21 (b) indicate that the double layer of the CV in 1 M $HClO_4$ downshift from 30 °C to 60 °C and then upshift from 60 °C to 80 °C. The phenomenon is the same to that in 1M H_2SO_4.

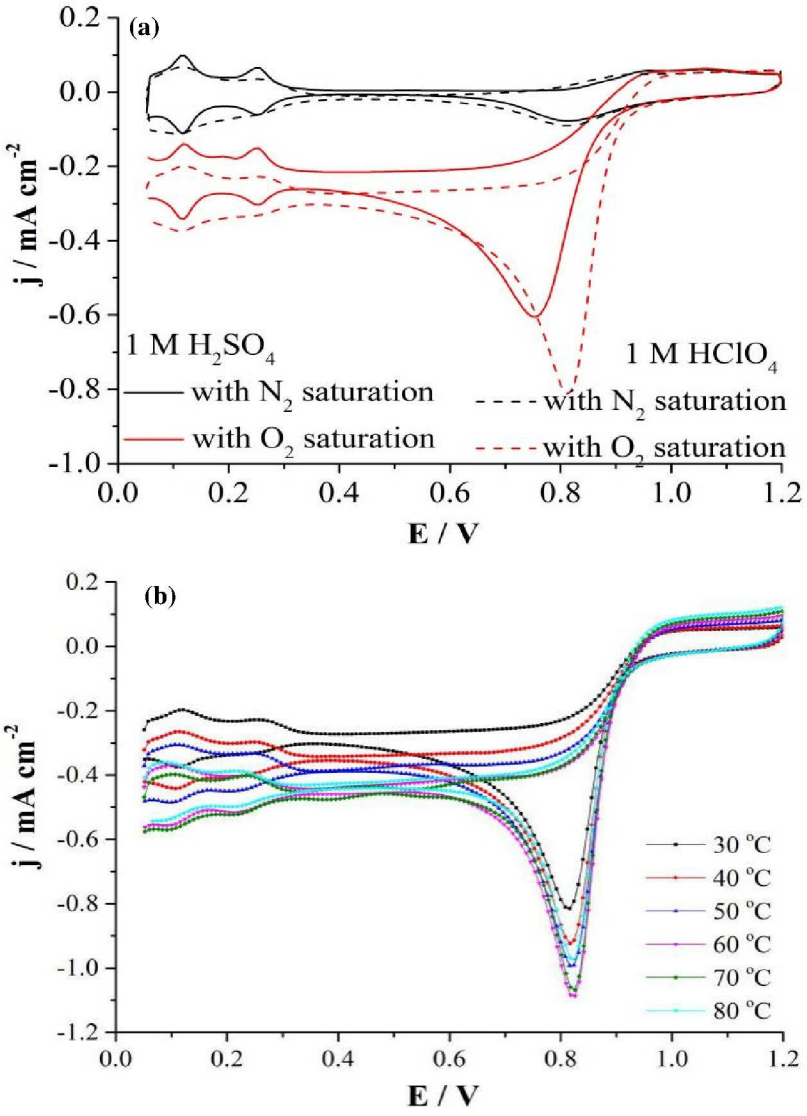

Figure 3.21. The CV of platinum (a) in 11 M H_2SO_4 (solid line) and 1 M $HClO_4$ (dashed line) with N_2 and O_2 saturation at 30 °C and (b) in 1 M $HClO_4$ with O_2 saturation from 30 °C to 80 °C.

Figure 3.22 display the OCP comparison of Pt in 1 M H_2SO_4 and 1 M $HClO_4$ from 30 °C to 80 °C. It can be seen, the OCP of Pt in 1 M H_2SO_4 goes slower than that in 1 M $HClO_4$ from 30 °C to 80 °C. Combining the study above, this is caused by the different Pt oxidation rate

determined by the property of acid. H_2SO_4, as the electrolyte, is not the best choice compared to $HClO_4$, it was used in order to compare the results with other literature data.

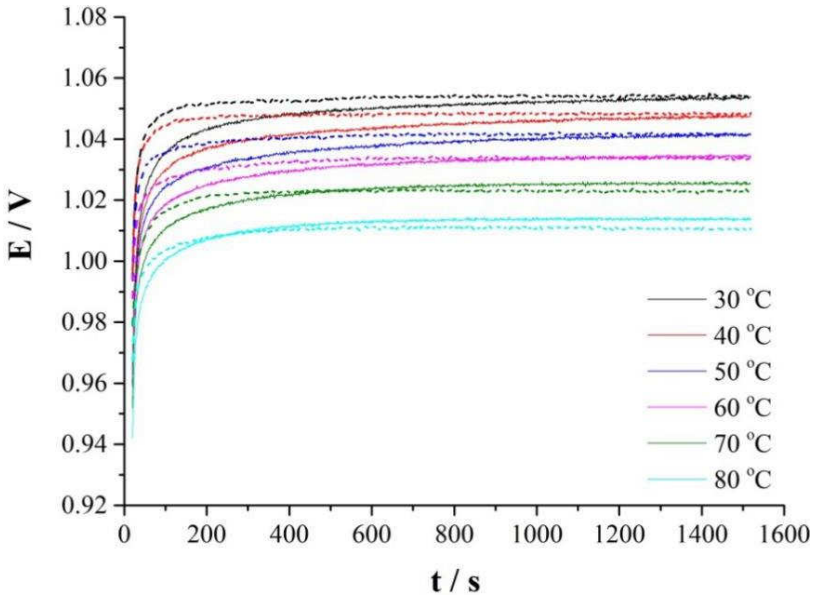

Figure 3.22. The t-E of platinum in 1 M H_2SO_4 (solid line) and 1 M $HClO_4$ (dashed line) with O_2 saturation from 30 °C to 80 °C.

3.3.6 The effect of equipment on OCP

Since 'glass cell-2' will be used in the next work, a simple comparison of the experimental results of the 'glass cell-1' and the 'glass cell-2' half-cell when the working electrode is platinum disk is given.

(1) The effect of operation on OCP

It is known that gas solubility has an effect on the OCP. Since a constant oxygen concentration is required for the electrolyte, the atmosphere above the electrolyte should be controlled carefully. The cell is normally used with open conditions to the atmosphere. In this work, a pure O_2 atmosphere needs to be guaranteed by a closed equipment. Thus the results under these two conditions (open and enclosed) are compared at first in this section. The Figure 3.23 and 3.24 gives the CV and OCP curves of 1 M H_2SO_4 when the 'glass cell-2' is open and enclosed, separately.

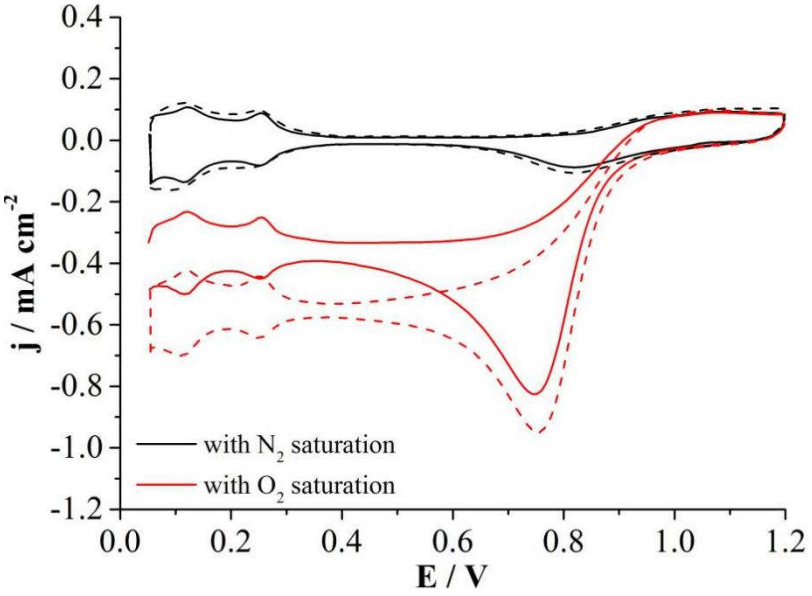

Figure 3.23. The comparison of the CV of Pt in 'glass cell-2' when cell is open (solid line) and closed (dashed line).

When the 'glass cell-2' is open, OCP value is smaller than the OCP when the cell is closed. Consulting also the CV diagram, the difference is caused by gas mass transfer, which is a result of the different saturation amounts of gas. Thus, the operation of closing is used in future work**.**

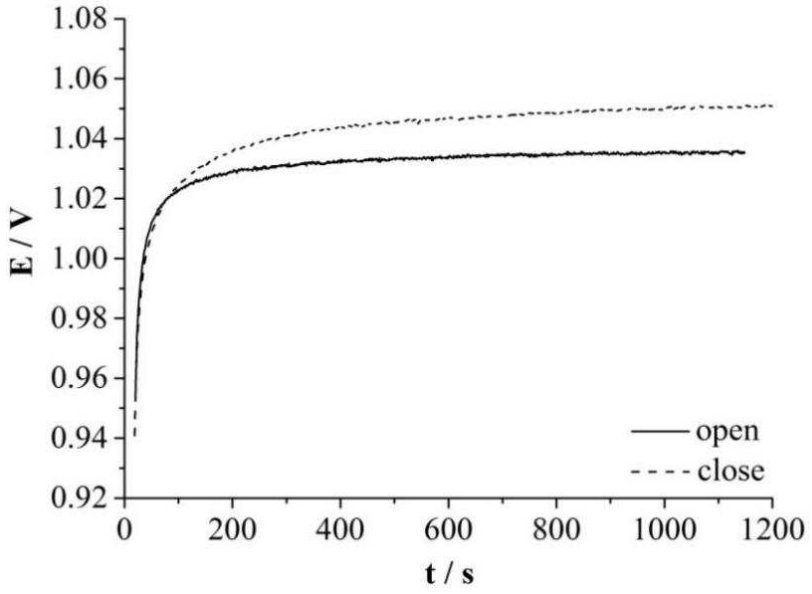

Figure 3.24. The comparison of the t-E of Pt in 'glass cell-2' when cell is open (solid line) and closed (dashed line) with O_2 saturation.

(2) The OCP comparison of Pt in 'glass cell-1' and 'glass cell-2'

After ensuring the closed cell condition, compare the OCP of Pt of these two kinds of equipment. Figure 3.25 and 3.26 display the comparison of their CV and OCP curves.

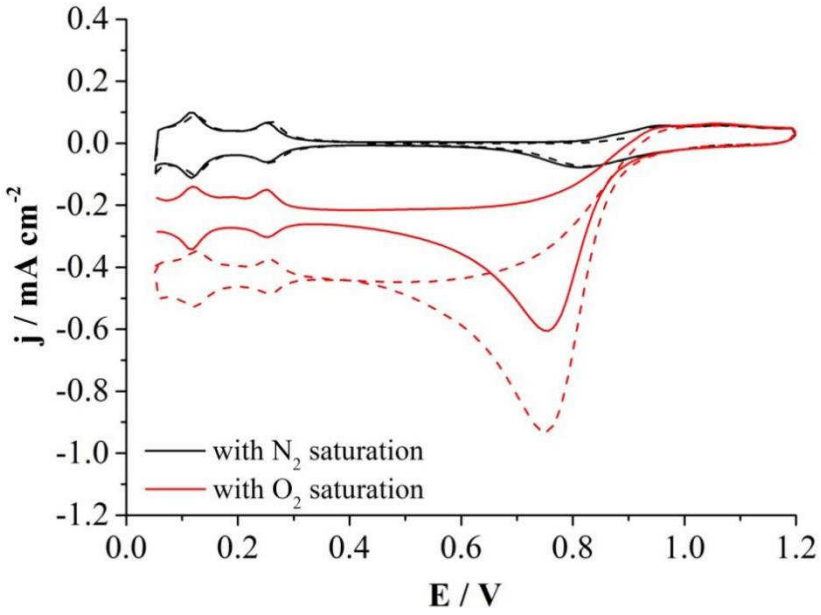

Figure 3.25. The comparison of the CV of Pt in 'glass cell-1' (solid line) and 'glass cell-2' (dashed line) with N_2 saturation and O_2 saturation.

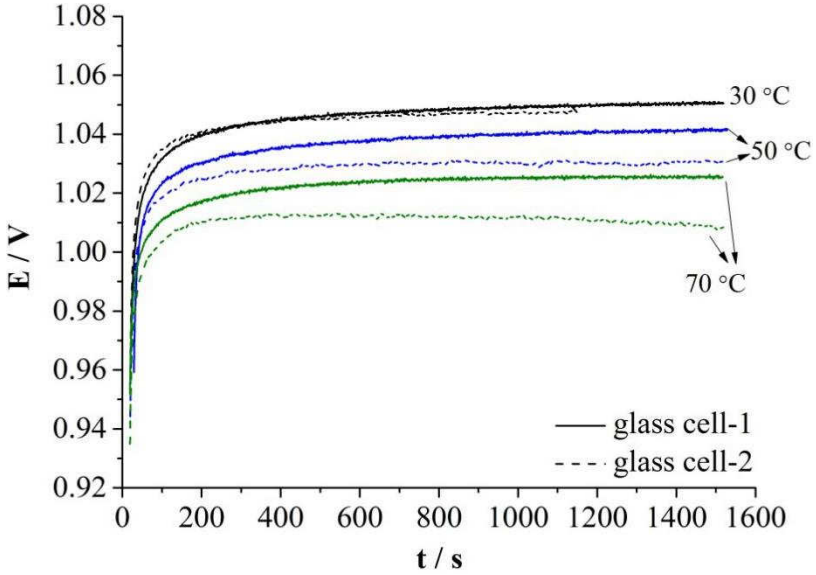

Figure 3.26. The comparison of the t-E of Pt in 'glass cell-1' (solid line) and 'glass cell-2' (dashed line) with O_2 saturation.

The results give us the same CV under N_2 condition by using these two kinds of half-cell equipment, which implies the same Pt surface condition is obtained. As for the OCP curve, they are the same at 30 °C. However, with temperature increases, the OCP measured by 'glass cell-2' half-cell is smaller than the OCP measured by glass cell.

(3) The reproducibility of the OCP of Pt in 'glass cell-2'

The experiment on the OCP of Pt in 'glass cell-2' is repeated several times. The result is shown in Figure 3.27. Because the voltage after 900 s increases very slowly, the voltage at 900 s is chosen for comparison. It is clear that the OCP at 900 s is 1.049 ± 0.001 V under the three identical preparation conditions.

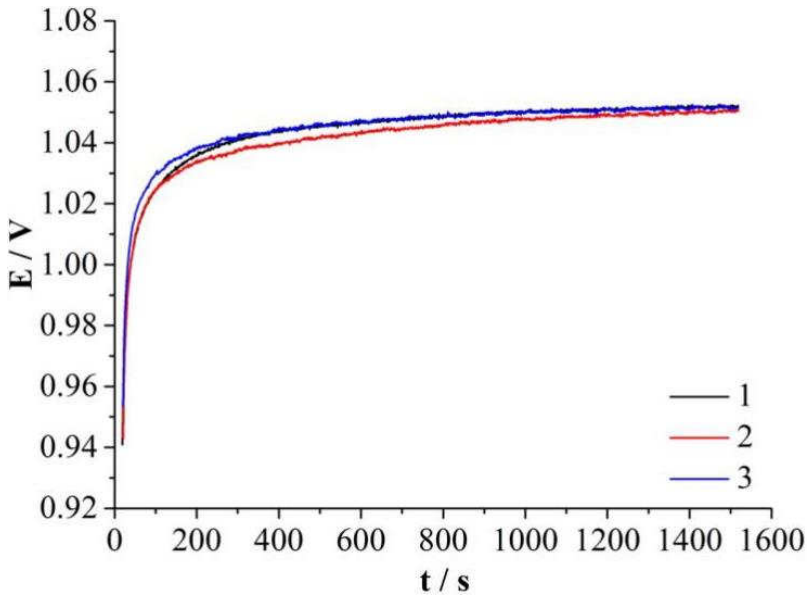

Figure 3.27. The t-E of Pt with O_2 saturation in 1M H_2SO_4 at 30 °C in the 'glass cell-2' when cell is closed. The measurement was repeated three times at identical conditions.

3.4 Summary

(1) The OCP of Pt in H_2SO_4 changes with time, which includes a fast reaction region and a slow reaction region. In the fast reaction steps, the OH_{ad} was adsorbed on the surface of the platinum. In the slow reaction steps, the OH_{ad} showed continuous oxidation into PtO_x species.

(2) As the temperature increases, the OCP of Pt in 1 M H_2SO_4, at 900 s, decreases. From 30 °C to 80 °C, it drops about 40 mV, at 900 s.

(3) The OCP of Pt in 1 M H_2SO_4 with O_2 saturation is higher than that with air saturation and higher than that with N_2 saturation. The Nernst equation and first order reaction have been used for calculation. The calculation results fit well with the experimental results. The mixed potential, E_{mix}, and the reaction rate constant, k, are a function of temperature. Moreover, the E_{mix} is independent of the gas concentration, and the reaction rate is faster for O_2 than for air. When a fairly stable OCP value is reached after 3 minutes, up to 36 % of the surface is covered by oxidized species in the case of O_2. This value is fairly close to the value of 0.35 obtained from an early experiment by other researchers.

(4) As the acid concentration increases, the OCP of Pt in H_2SO_4, at 900 s, decreases. From 0001 M to 6 M, it drops about 80 mV, at 900 s, at 30 °C. The mixed potential, E_{mix}, and the reaction rate constant, k, depends on the concentration. A possible explanation is that the proton amounts on both sides of the electrode of the cell are no longer the same following the surface oxidation of the platinum electrode on the cathode side.

(5) Reaction rate depends on electrolytes. In perchloric acid, it seems to be faster, but the sulfuric acid is chosen because the results can be compared to the literature.

(6) The ‘glass cell-2’ shows a lower OCP value than that of ‘glass cell-1’.

Chapter 4 Half-cell experiment with carbon support

4.1 Introduction

In the previous work, when the catalyst is a Pt disk, the OCP of half-cell in different concentrations of sulfuric acid with O_2 saturation from 30 °C to 80 °C has been tested in 'glass cell-1' and 'glass cell-2' by the measurement of linear voltammetry scan and chronopotentiometry. All the t-E curves show a feature that the potential increases quickly in the initial 3 minutes, and then goes to a stable state. The OCP decreases when the temperature or electrolyte concentration increases. In order to understand OCP further, the model including Nernst equation and first order reaction were used for calculation, which explains OCP well as a mix of oxygen reduction and platinum oxidation.

In fuel cells, carbon supported nanoparticals of Pt are used as electrodes. From the results of Borup's group [74] and Hasche's group [75], it is known that for fuel cells, the carbon oxidation can be negligible because of its slow kinetics under normal operational conditions, but it occurs easily on the cathode under start-up and shut-down conditions. Carbon oxidation effects the loss of structural carbon, and causes a significant change of the surface properties and an aggregation of isolated metal particles when carbon materials are used for a catalyst support [85, 86, 130]. Thus, it is significant to study the carbon oxidation under open circuit conditions.

In this thesis, the OCP of pure carbon in 1 M sulfuric acid in the temperature range of 30 °C - 80 °C is investigated in this chapter.

4.2 Experimental

For the 'glass cell-1', the working electrode is clamped on one side of the outside of the cell, which makes it hard to ensure electrolyte contact at the same position. Thus, the problem of leaking of catalyst and the unknown geometric area of the electrode exist when the catalyst is a film. Owing to this issue, the 'glass cell-1' is replaced by rotating disk electrode in next work. The equipment was shown in Figure 2.3.

In this chapter, the rotating disk electrode of glassy carbon covered by carbon layer was used as the working electrode, while a reversible hydrogen electrode (HydroFlex, Gaskatel GmbH) was employed as the reference electrode and a platinum mesh served as the counter electrode. The details on the preparation work and the equipment used in this chapter is shown in chapter 2.

In this chapter, three different thicknesses of carbon layer are studied, with the carbon loading of 30, 40 and 80 μg cm^{-2}, respectively. In addition, the carbon layer with the loading of 40 μg cm^{-2} is studied under N_2, air and O_2 saturation, separately.

4.3 Results and discussion

4.3.1 The electrochemical measurement

The method of CV, LSV and chronopotentiometry is used in this chapter. CV is an important electrochemical characterization method that can show evidence of surface oxide formation through increased peak current assigned to the hydroquinone – quinone (HQ – Q) redox couple of carbon [74, 93]. Figure 4.1 and Figure 4.2 shows their CV results of carbon layer with loading of 80 μg_C cm^{-2} in 1 M H_2SO_4 at 30 °C at a scan rate of 50 mV s^{-1}.

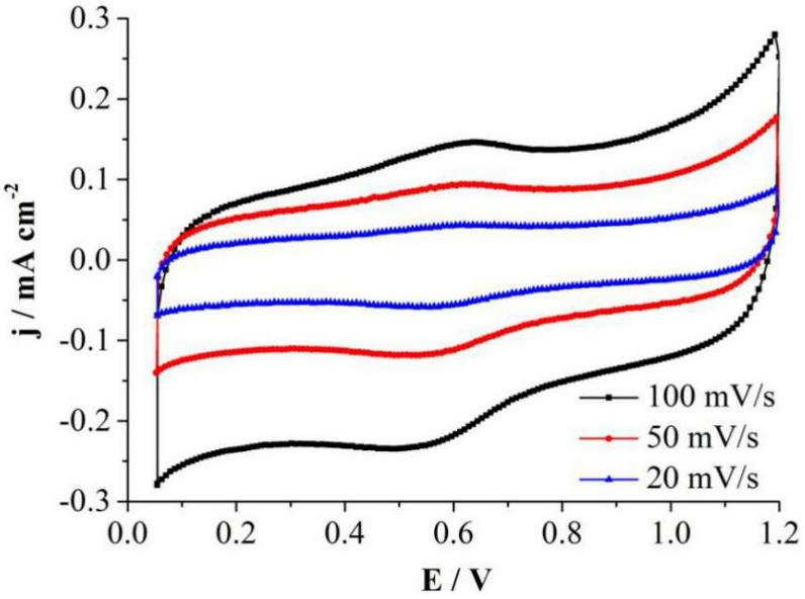

Figure 4.1. The CV of carbon layer with the carbon amount of 80 μg cm^{-2} in 1 M H_2SO_4 on different scan rate at 30 °C with N_2 saturation.

The CV under N_2 condition shows a rectangular type with two smooth peaks in the anodic and cathodic direction, which is about 0.6 V. This is in line with the literature [74, 86, 94], which can be applied to oxygen-containing functional groups, generally a hydroquinone-quinone (HQ-Q) redox pair [83]. Compared to the CV swept at a scan rate of 20 and 100 mV s^{-1}, the CV swept on scan rate of 50 mV s^{-1} is of obvious peak and nonserious tilt phenomenon. Thus, it will be used in the next experiments.

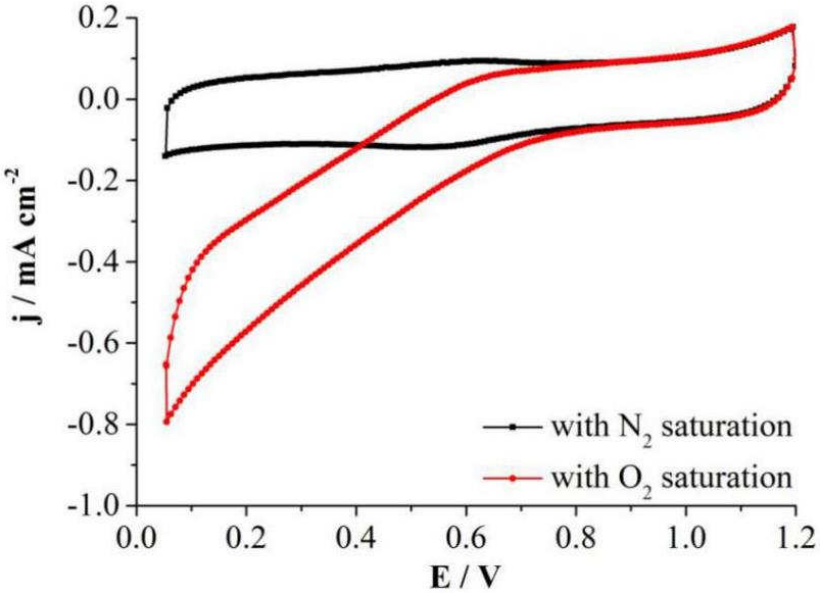

Figure 4.2. The CV of carbon layer with a carbon amount of 80 µg cm^{-2} in 1 M H_2SO_4 at a scan rate of 50 mV s^{-1} at 30 °C with N_2 and O_2 saturation.

Compared with the CV under N_2 saturation, the CV with O_2 saturation shows a tilted region when the potential is below 0.8 V, as well as a similar region when the potential is above 0.8 V, which was thought as an OCP region. It means that the oxygen reduction occurs slowly as the potential is about 0.8 V. Following the decreasing of the potential, the reaction becomes fast, and the reaction does not achieve a stable condition even at 0.05 V. It seems that the carbon prepared in this thesis is not a good choice for the oxygen reduction reaction (ORR). Nevertheless some researchers have given examples of optimized carbon materials for ORR [131-133], like nitrogen doped carbon nano materials.

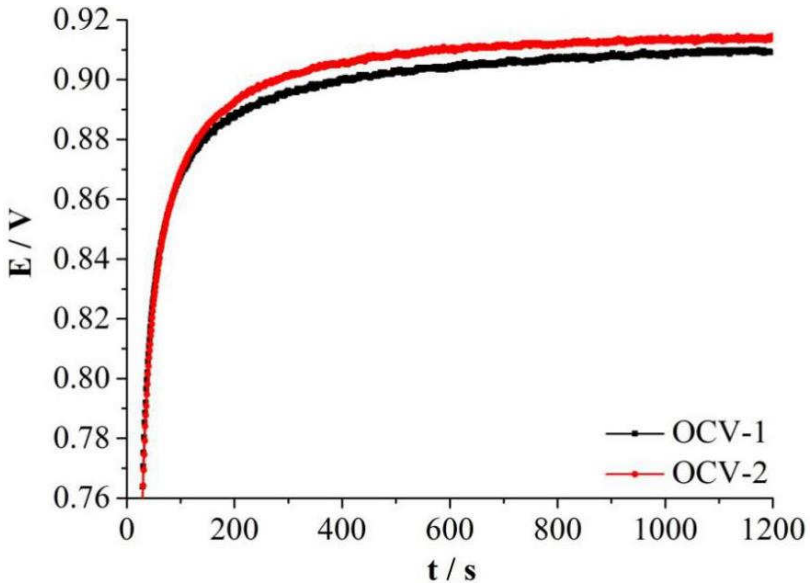

Figure 4.3. The t-E curves of carbon layer with the carbon amount of 80 µg cm^{-2} in 1 M H_2SO_4 at 30 °C with O_2 saturation. The results of two measurements under identical test conditions are displayed.

The same method of OCP measurement as given before is used. The repeated testing OCP at 30 °C is shown in Figure 4.3. Obviously, the t-E curve shows the same shape as pure platinum, including a fast increasing region (< 200 s) and a stable region (> 200 s). Combining this with knowledge introduced in chapter 1, the process can be simply divided into 2 steps: the adsorption of carbon oxide species on the surface of carbon support, and the further oxidation of united carbon oxide species to form carbon dioxide or carbon monoxide. Moreover, the OCP shows a phenomenon that the second measurement OCP (at 900 s) is a little higher (≈ 4 mV) than the first one. This is caused by the special structure of the carbon layer. The porous structure makes the oxidation reduction reaction occur not only on the outer surface of carbon layer, but also on the inner surface.

4.3.2 The temperature effect on OCP

As in the previous chapter, the temperature effect is studied in the range of 30 – 70 °C. Figure 4.4 displays the CV of carbon layer with the loading of 80 µg cm^{-2} under O_2 saturation. Clearly, the typical carbon CV is obtained at each temperature and the slope decreases with increasing temperature.

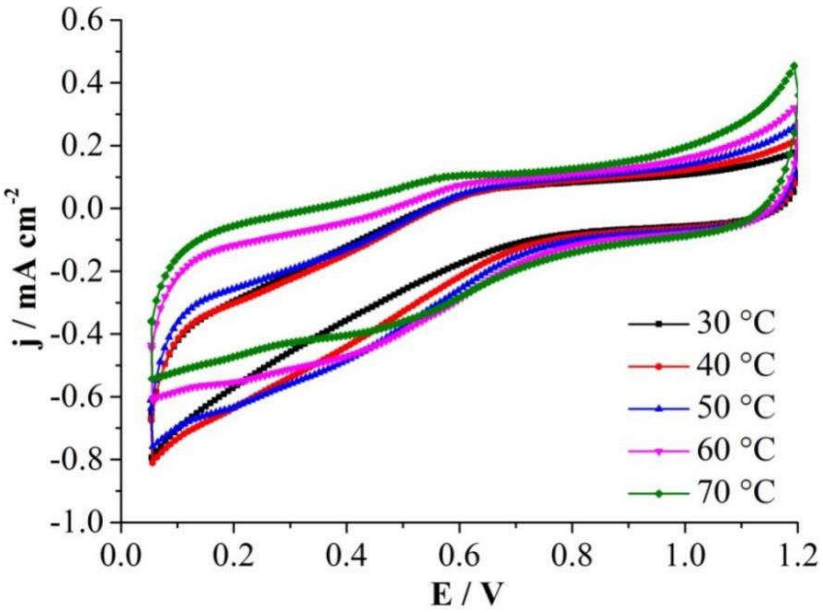

Figure 4.4. The CV of carbon layer with the carbon amount of 80 μg cm^{-2} in 1 M H_2SO_4 in the temperature range of 30-70 °C with O_2 saturation.

The t-E curves are shown in Figure 4.5. It is clear that the higher the temperature, the smaller the OCP (at 900 s), except for that at 40 °C, which is the same as that at 30 °C.

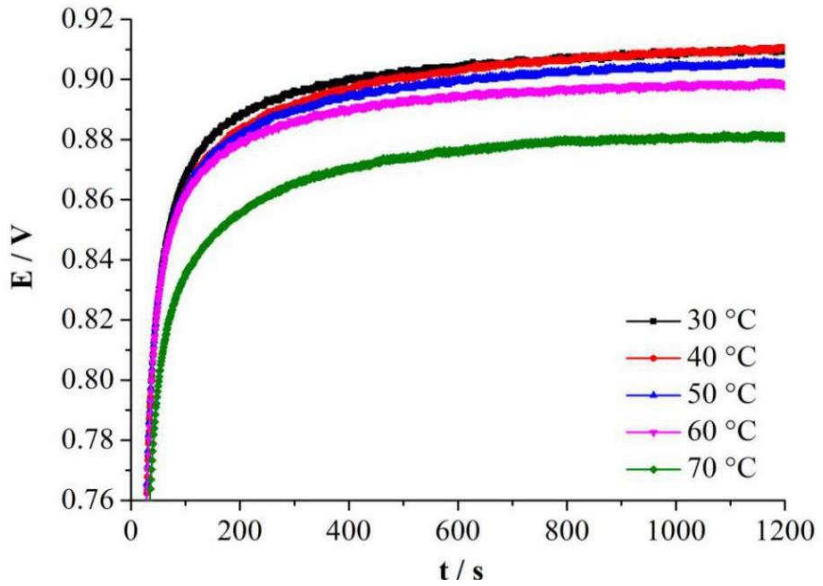

Figure 4.5. The t-E curve of carbon layer with the carbon amount of 80 μg cm^{-2} in 1 M H_2SO_4 in the temperature range of 30-70 °C with O_2 saturation.

4.3.3 The effect of the thickness of carbon layer on OCP

It's known that the preparation of the carbon layer has an effect on OCP. In this chapter, the influence of different thicknesses of the catalyst layer on OCP is studied. Here, 0 µg cm^{-2} means there is no carbon layer on the surface of glassy carbon electrode. It was used as reference. Additionally, how the carbon layer relates to the carbon amount of 30, 40 and 80 µg cm^{-2} is investigated in this chapter. The reason of the choice of these three carbon amounts is that they are the carbon amounts of the catalyst layer that will be discussed in the chapter 5.

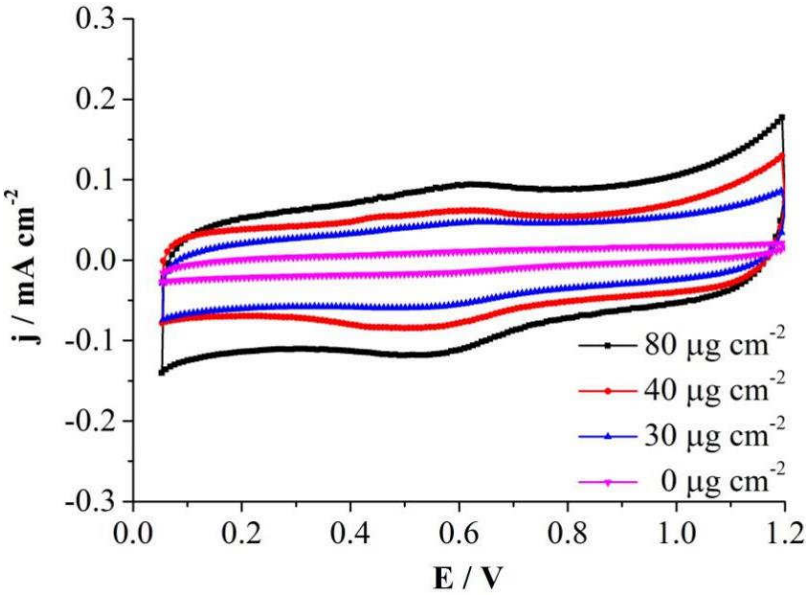

Figure 4.6. The CV of different thickness of carbon layers in 1 M H_2SO_4 at 30°C with N_2 saturation.

The CV under N_2 saturation and O_2 saturation is shown in Figure 4.6 and Figure 4.7, separately. It can be seen that the CV becomes more broadened as the thickness increases. The tilted slope of CV below 0.8 V with O_2 saturation increases with increasing thickness. The reason is that the higher the carbon amount, the higher the internal surface area.

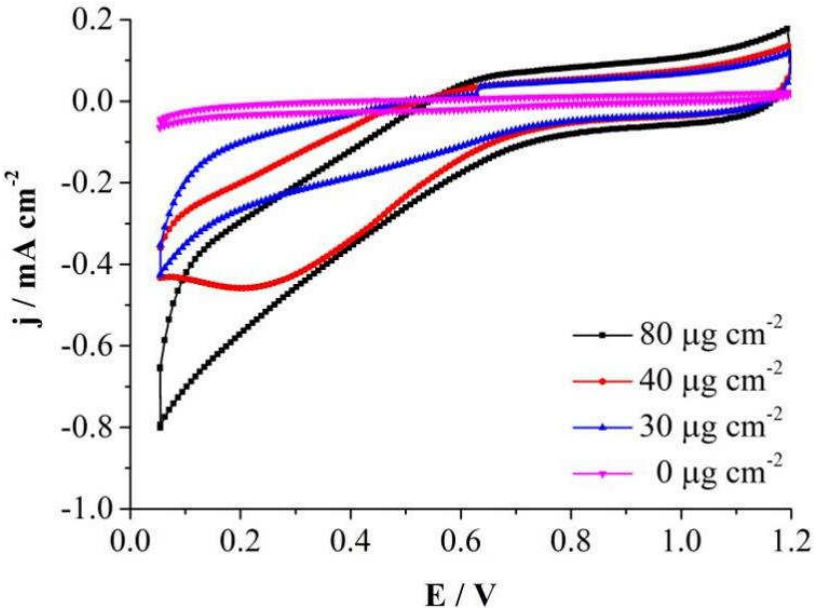

Figure 4.7. The CV of different thickness of carbon layers in 1 M H_2SO_4 at 30°C with O_2 saturation.

Figure 4.8 gives the OCP of the carbon layer with different thicknesses. Clearly, the thicker the carbon layer, the higher the OCP value (at 900 s). It may be caused by the specific surface area. The thicker the carbon layer, the higher the specific surface area. Moreover, the porous carbon layer shows a much higher OCP value compared to the glassy carbon surface. The much increased specific surface area may be one reason compared to the glassy carbon surface. Another possibility is that there exist an interface of different thickness formed between the glassy carbon electrode and the carbon layer of different thickness. Combining the CV under O_2 saturation, the reason may also be that the oxide group formed on the glassy carbon and on the carbon layer of different thickness is different.

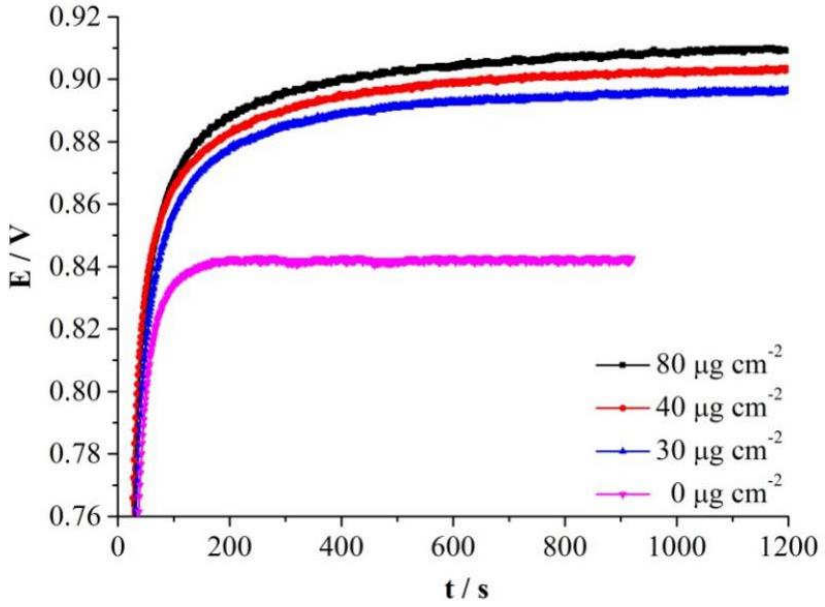

Figure 4.8. The t-E curve of different thickness of carbon layers in 1 M H_2SO_4 at 30°C with O_2 saturation.

4.3.4 The effect of different gas composition on OCP

The sample with the moderate carbon amount of 40 μg cm^{-2} is used to study the effect of gas type. Figure 4.9 displays the CV under three conditions, N_2, air and O_2. It can be seen that the normal CV of carbon layer is obtained. The CV below 0.8 V under O_2 saturation shows a bigger slope than that under air saturation.

The OCP at 30 °C under these conditions shows in Figure 4.10. The result shows that the increasing of OCP under air saturation is slower than that under O_2 saturation, and faster than that under N_2 saturation. The possibility is that the different surface oxide covered on the surface, and the higher the O_2 concentration, the bigger the surface coverage. Moreover, the stable OCP value (at 900 s) under O_2 is higher (15 mV) than that under air conditions, which is much more than that under N_2 conditions.

Figure 4.11 displays the OCP under these three conditions from 30 °C to 70 °C. Obviously, the higher the temperature, the lower the stable OCP value (at 900 s), except for that under O_2 conditions at 40 °C. And the voltage difference from 30 °C to 70 °C is about 28, 17 and 18 mV under the conditions of N_2, air and O_2, separately.

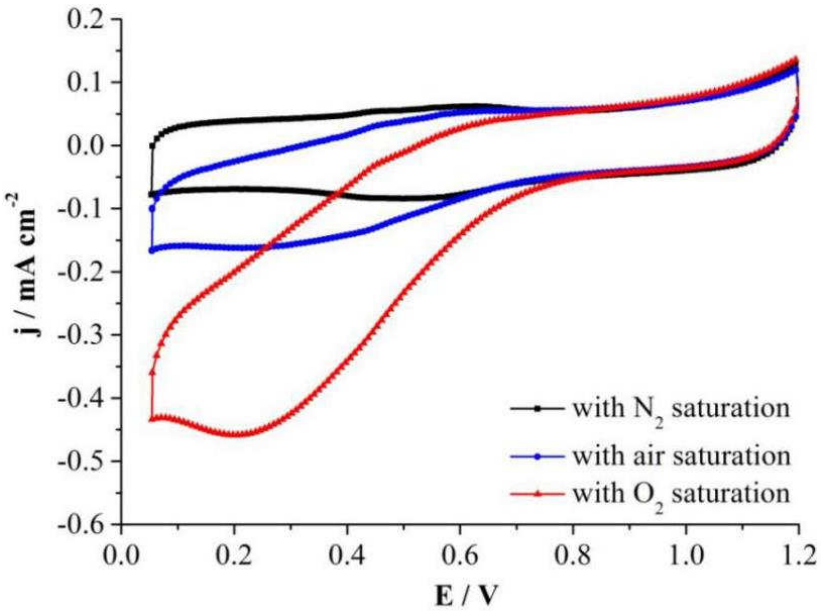

Figure 4.9. The CV of carbon layer with the carbon amount of 40 µg cm^{-2} in 1 M H_2SO_4 at 30°C with N_2, air and O_2 saturation.

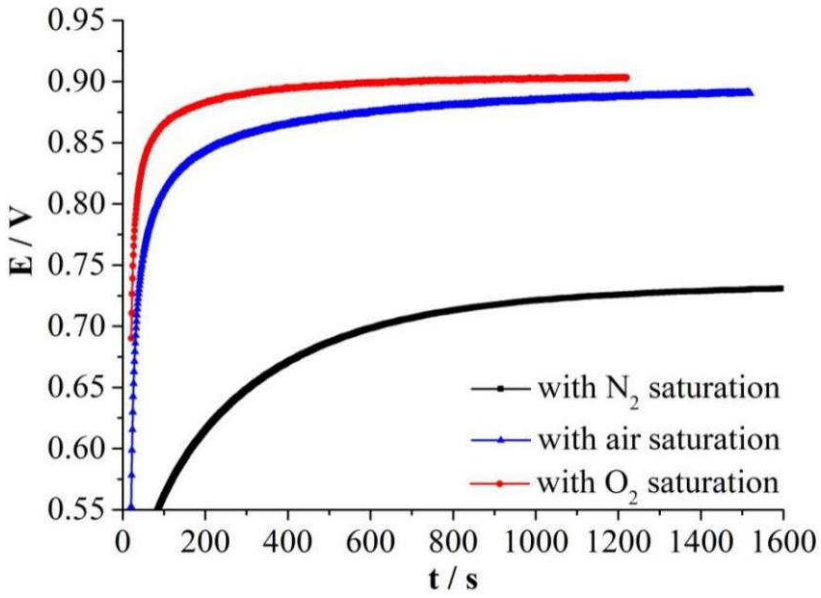

Figure 4.10. The t-E curves of carbon layer with the carbon amount of 40 µg cm^{-2} in 1 M H_2SO_4 at 30°C with N_2, air and O_2 saturation.

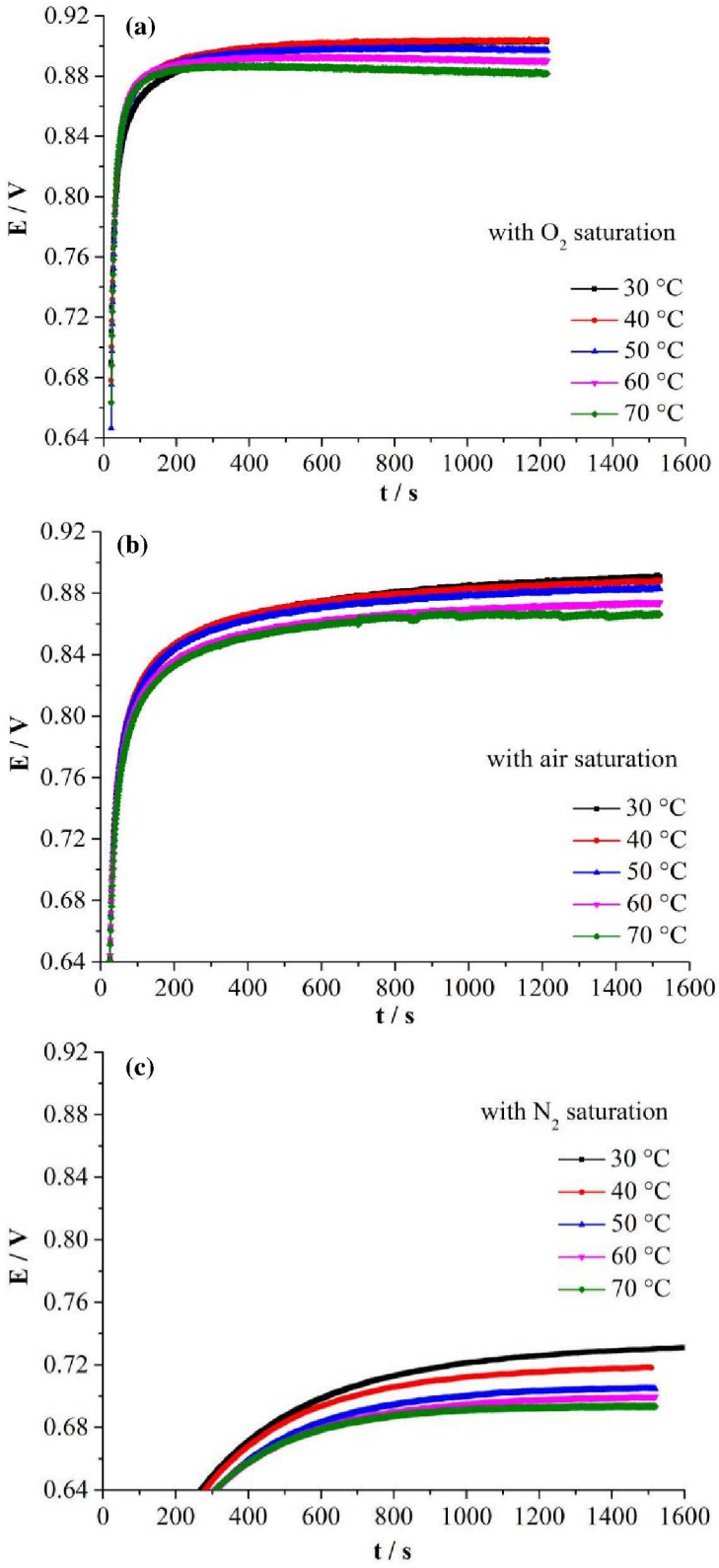

Figure 4.11. The t-E curves of carbon layer with the carbon amount of 40 μg cm^{-2} in 1 M H_2SO_4 from 30 °C to 70 °C with (a) N_2, (b) air and (c) O_2 saturation.

According to Equation 2.27 and the experimental results shown in Figure 4.11, the fitting results, which consider the gas solubility, are shown in Figure 4.12. The graph (a) and (b) relates to the OCP with O_2 and air saturation, respectively.

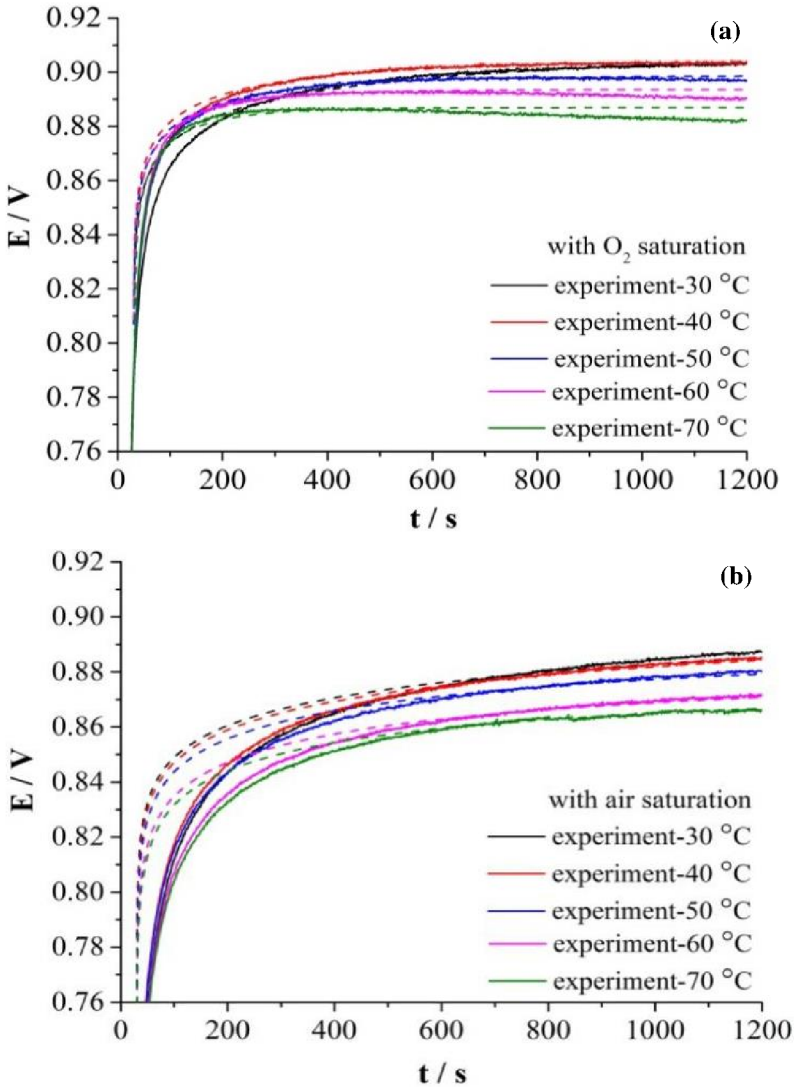

Figure 4.12. The experimental (solid line) and calculated (dashed line) t-E of carbon layer with the carbon amount of 40 µg cm^{-2} in 1 M H_2SO_4 from 30 °C to 70 °C with (a) O_2 and (b) air saturation.

Obviously, the calculation results fit well with the experimental OCP for O_2. However it does not work well for air because of the very slow reaction rate. Figure 4.13 shows the fitting parameters of $E^0_{mix}(T)$ and k, as a function of temperature. This figure shows the fitting results by the model of gas solubility, which is introduced in chapter 2.

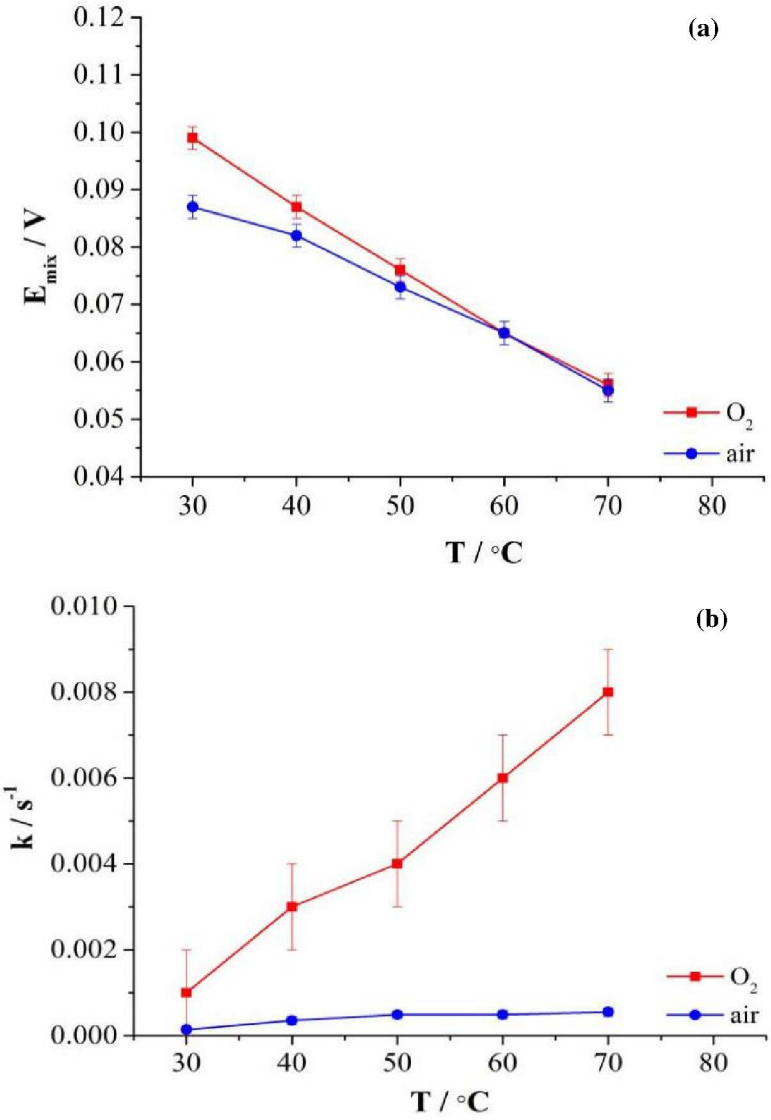

Figure 4.13. Fitting parameters E^{0}_{mix}(T) (a) and k(T) (b) with O_2 (red) and air (blue) saturation from 30 °C to 70 °C .

The E^{0}_{mix}(T) and k depends on temperature. The same value of E^{0}_{mix} is obtained for air and oxygen except for that at 30 °C, as shown in Figure 4.13(a), E^{0}_{mix}(T) decreases with increasing temperature**.** Figure 4.13 (b) shows the resulting values for the reaction rate coefficient k, which increases with increasing temperature, with values for air being nearly 0. This means the carbon oxidation reaction is nearly 0 in the case of air. With the temperature increasing, this condition is relieved.

From the reaction rate constants, the surface fraction of the oxidized carbon species for O_2 and air is obtained, as shown in Figure 4.14(a) and 4.14(b). Obviously, the higher the temperature gets, the bigger the surface coverage becomes, since the higher the reaction rate is. In the case of O_2, after 900 s, the surface is covered to 50% at 30 °C and almost completely oxidized starting from 40 °C. For air, only small amount of surface is covered, and the surface coverage at 30 °C is about 0.1 after 900 s, and even at 70 °C, a surface fraction of only 0.4 is reached.

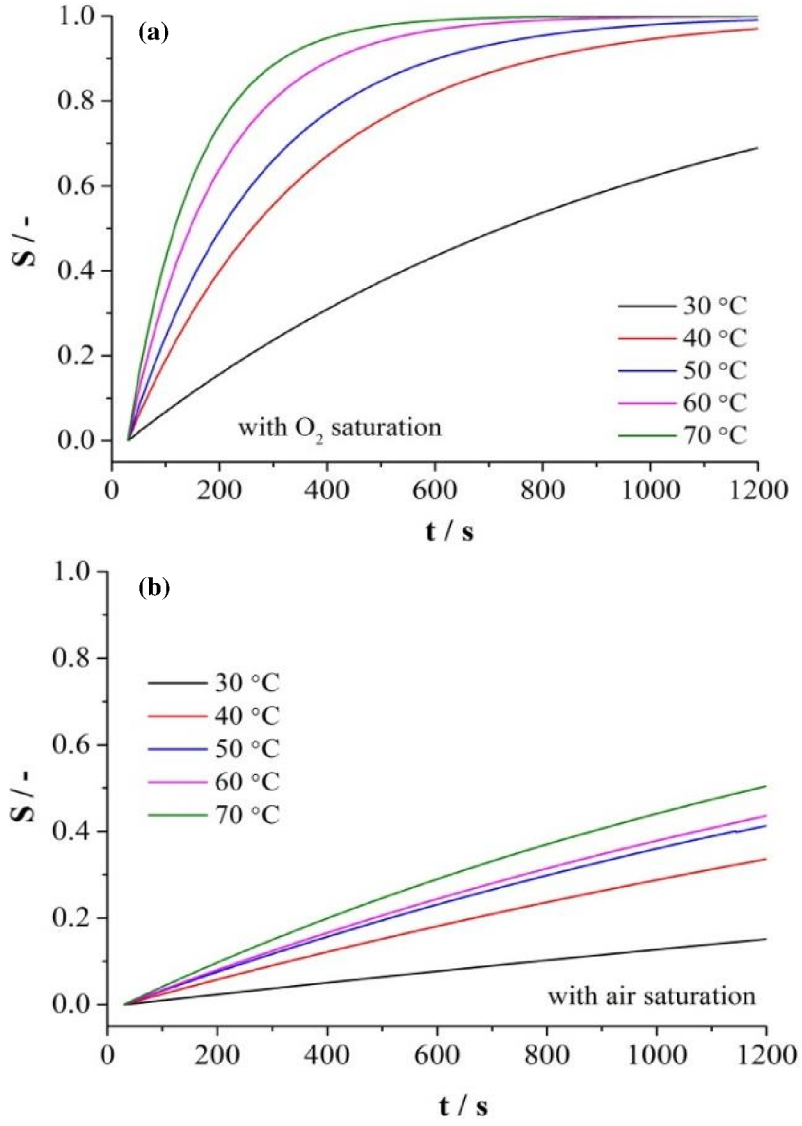

Figure 4.14. Surface coverage S as a function of time measured with O_2 (a) and air (b) saturation in the temperature range of 30-70°C.

4.4 Summary

(1) The t-E curve of carbon support shows to be the same type as that of the Pt disk, which includes fast reaction steps and slow reaction steps. They are the adsorption of carbon oxide species on the surface of carbon and its further oxidation to carbon monoxide or carbon dioxide, separately. Additionally, the value at 900 s, about 0.9 V, is lower than that of Pt disk.

(2) As temperature increases from 30 °C to 70 °C, the OCP of carbon layer in the slow region, at 900 s, decreases by 28 mV.

(3) The thicker the carbon layer gets, the higher the OCP value (at 900 s) becomes.

(4) Gas composition has an effect on the OCP of carbon layer. The OCP with N_2, air and O_2 saturation in 1 M H_2SO_4 is higher and higher. The Nernst equation and first order reaction have been used for calculation by using the model of gas solubility. A good fitting result is obtained.

Chapter 5 Half-cell experiment with Pt on carbon support

5.1 Introduction

In chapter 3 and 4, the OCP of pure platinum and carbon support in 1 M sulfuric acid with N_2, air and O_2 saturation from 30 °C to 70 °C has been studied using linear voltammetry scan and chronopotentiometry. Their OCP time dependent curves show a similar feature to that of platinum. The potential increases rapidly in the first several minutes, and then goes to a stable state. The OCP decreases with increases in the temperature or gas solubility. However, the OCP of the carbon layer is much lower than that of pure platinum.

In this chapter, the catalyst layer of Pt on carbon support is examined, which is widely used as catalyst in low temperature PEFC. The OCP of platinum on carbon in 1 M sulfuric acid in the temperature range of 30 °C to 70 °C is also investigated.

For the catalyst layer, as well as the material itself, the preparation is very important, as preparation will influence performance. And the preparation of the catalyst support is influenced by the species, structural components, and processes and so on. Using as electrode for the fuel cell, a pore network structure and a uniform reaction condition constitute the main targets of the catalyst preparation. These days, the prevailing type of catalyst layer used is a three-phase composite media which consists of a solid phase of Pt and electronic support material, an electrolyte phase of ionomer and water, and the gas phase in the porous medium [16]. The catalyst ink depends on the catalyst type. According to previous studies [134-136], the type and amount of alcohol, and its ratio to water, and the thickness of Nafion films should be optimized to each catalyst. Thus, a method from Garsany group [113] is used in this thesis.

5.2 Experimental

5.2.1 The cell

As with the carbon layer, a rotating disk electrode of glassy carbon covered by catalyst layer was used as the working electrode in this chapter because of good avoidance shown on boundary issues as before. As the reference electrode, a reversible hydrogen electrode (HydroFlex, Gaskatel GmbH) was employed, while a platinum mesh served as the counter electrode.

The 98 wt.% H_2SO_4 was diluted by using ultrapure water for the preparation of 1 M acidic electrolytes. High purity of nitrogen (99.999%), oxygen (99.9991%) and hydrogen (99.999%) were used.

The details on the preparation of electrode and catalyst ink have given in chapter 2. Three different ratios of Pt on Vulcan carbon are used in this chapter. Their Pt ratios are 20%, 46% and 60%. The amount of inks used in this chapter always is 10 µl. Additionally, for the catalyst of 60% Pt/C, the films of different platinum loading are studied, which is 20, 60 and 120 $\mu g_{Pt}\ cm^{-2}$.

5.2.2 Electrochemical measurement

After the cell was purged for 30 min with N_2 at gas flow rate of 100 ml min^{-1}, the specimen was connected to the Autolab potentiostat PGSTAT302N (Metrohm). In order to demonstrate cleanliness of the surface, eight cycles in the potential range of 0.05-1.2 V were performed with the working electrode. Afterward, by switching the gas to O_2 for 30 minutes at 100 ml min^{-1} gas-flow rate, a CV on the potential range of 0.05 and 1.2 V at 50 mV s^{-1} was implemented again. Finally, linear sweep voltammetry was performed in the cathodic direction from 1.1 V to 0.4 V, This was immediately followed by open circuit voltage record. The experiment was repeated by using OCP with N_2 and air saturation.

5.3 Results and discussion

5.3.1 Electrochemical measurement of 20% Pt on carbon support

An electrochemical cleaning procedure should be done at first by using sweeping cyclic voltammetry linear scan from 0.0 V to 1.2 V for several cycles at the scan rate of 100 mV s^{-1}

[113] after feeding nitrogen for 30 minutes. Then, the CV sweeping measurements between 0.05 V and 1.20 V at a suitable rate during 20 - 100 mV s^{-1} is done. It can be used to calculate the Pt electrochemical surface area in the 0.05 -0.4 V region. Here, the catalyst of $Pt/C_{20\%\ Pt}$ with platinum loading of 20 μg_{Pt} cm^{-2} was given as an example to show the OCP measurement and their results.

Figure 5.1 gives a comparison of CV at different sweeping rates. Clearly, the electrode of $Pt/C_{20\%\ Pt}$ shows a platinum CV shape, and the higher the sweeping rate, the higher the intensity of peaks. For example, the CV at the rate of 50 mV s^{-1} shows two obvious and nearly symmetrical hydrogen adsorption and desorption peaks. They are the peaks related to (110)-type sites at 0.115 V and the peak related to (100)-type sites at 0.240 V, which are typical peaks of poly-platinum [2]. Therefore, compared to the platinum oxidation, the carbon oxidation is very weak in the catalyst of platinum on carbon.

The positive peaks at 0.89 V and 1.04 V relate to the production of Pt_2OH and PtOH, separately, and the negative peak at 0.77 V shows the character of the reduction of platinum oxide. The small positive flat at 0.51 V is the oxidation peak of carbon groups. Totally, the CV of Figure 5.3 illustrates that the electrode of platinum on Vulcan carbon is clean. For the CV swept at 50 mV s^{-1}, the type of peak is clear and the intensity of peak is moderate. Thus, 50 mV s^{-1} is used as the sweeping rate of CV in next experiment.

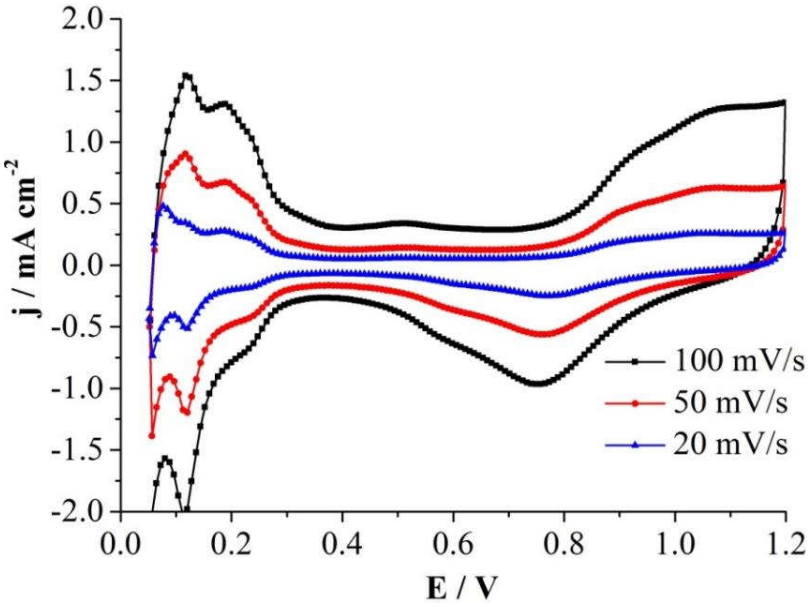

Figure 5.1. The CV of $Pt/C_{20\%\ Pt}$ with N_2 saturated in 1 M H_2SO_4 at 30 °C at different sweeping rate.

Next switch the gas to O_2 for 30 minutes, and then sweep the CV from 0.05 to 1.2 V at the rate of 50 mV s^{-1}. Figure 5.2 gives the CV with O_2 and N_2 saturation. Integrating the current density in the H adsorption potential region, and then dividing by scan rate, the charge density is 3115.98 μC cm^{-2}, which is much more than pure platinum, about 252.11 μC cm^{-2}. This is because the real surface area of catalyst layer of platinum on carbon is much more than the geometric one owing to the existence of porous carbon structure. Comparing the CV with N_2 and O_2 saturation, the results is the same as that of pure Pt. That is they have the same potential position but different net current. And the CV above 0.9 V is the same region which was thought to be the OCP region.

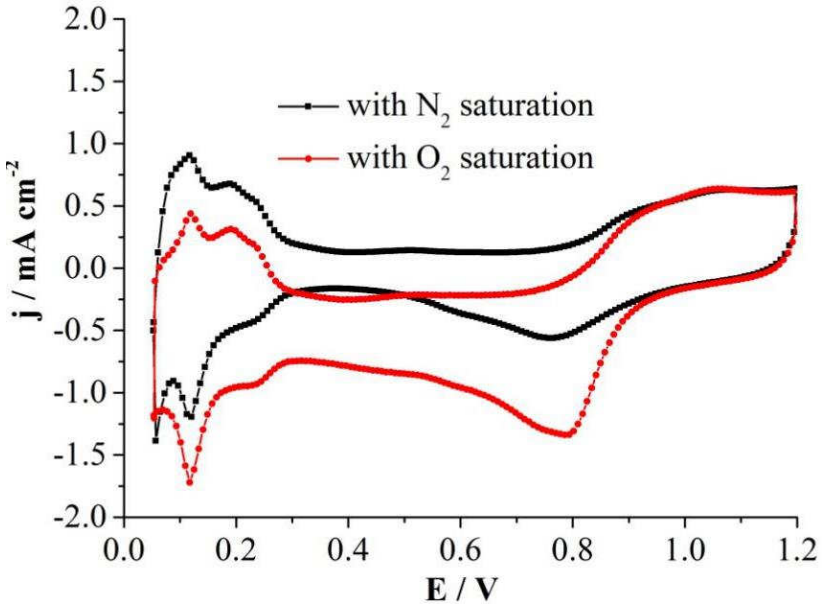

Figure 5.2. The CV of $Pt/C_{20\%\ Pt}$ with N_2 and O_2 saturation in 1 M H_2SO_4 at 30 °C at a sweeping rate of 50 mV s^{-1}.

Following the CV measurement, the same OCP measurement as that of pure Pt, introduced in chapter 3, is applied. That is LSV measurement and the chronopotentiometry method. Figure 5.3 and Figure 5.4 give one of the results at 30 °C in 1 M H_2SO_4.

The LSV swept from 1.1 V to 0.4 V is applied for reducing the surface of platinum to a pure Pt condition. Two times measurements was using to check the reproducibility. Clearly, the same LSV curve was obtained, which means the surface condition is the same before two times OCP measurements.

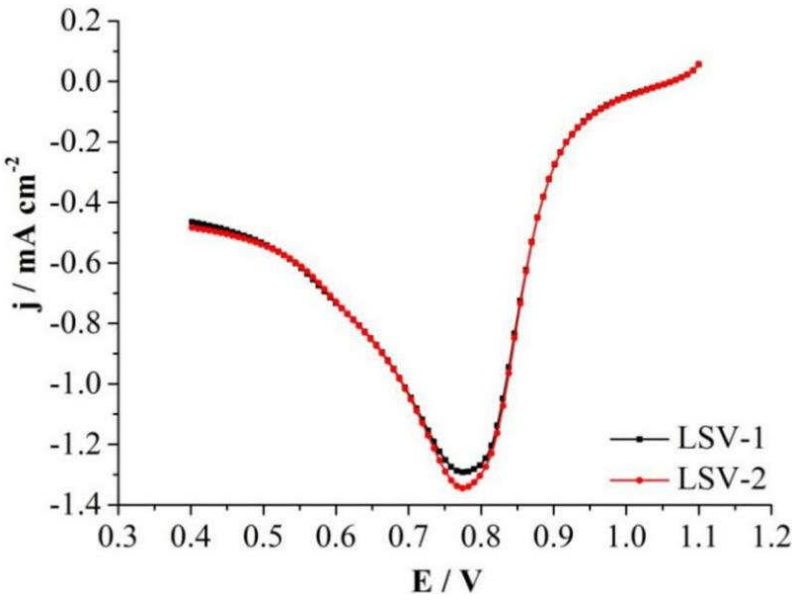

Figure 5.3. The LSV curves of $Pt/C_{20\%\ Pt}$ in 1 M H_2SO_4 at 30 °C at a sweeping rate of 50 mV s^{-1}. The results of two measurements under identical test conditions are displayed.

It is known from Figure 5.4 that the potential goes from a sharply increasing step to a slower transition, and finally up to a steady state. Combining the t-E curve of platinum and carbon with loading of 80 µg cm^{-2}, this is the mixed processes of oxygen reduction and the platinum or carbon oxidation. In addition, the OCP value, at 900 s, is closer to the OCP value of pure platinum, as shown in Figure 5.5. Combining the CV and OCP results, it is Pt that plays a major role in Pt/C catalyst.

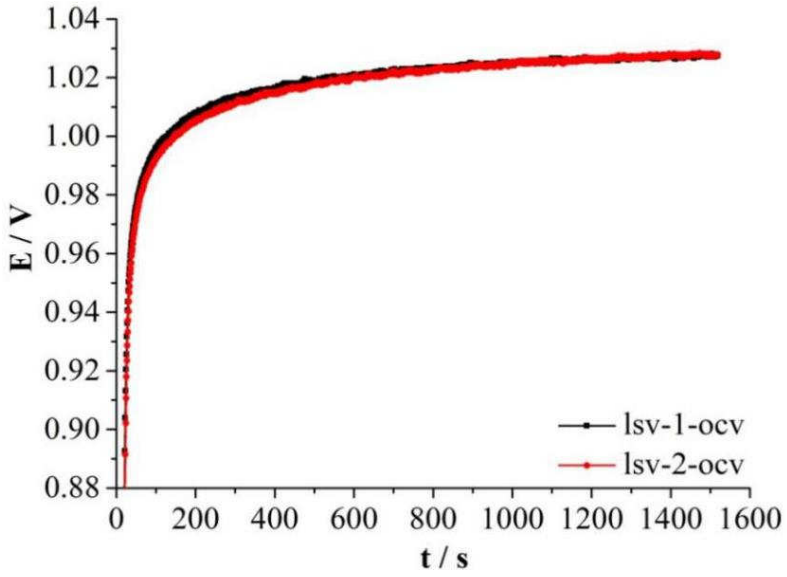

Figure 5.4. The t-E curves of $Pt/C_{20\%\ Pt}$ in 1 M H_2SO_4 at 30 °C under open circuit condition after LSV-1 and LSV-2.

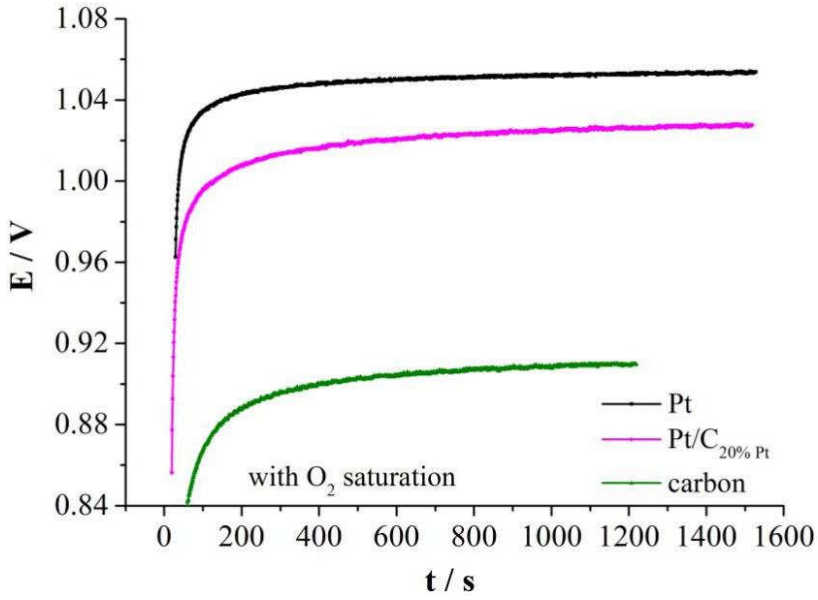

Figure 5.5. The t-E curves of Pt, $Pt/C_{20\%\ Pt}$ (20 μg_{Pt} cm^{-2}) and carbon (80 µg cm^{-2}) in 1 M H_2SO_4 at 30 °C under open circuit condition.

The reproducibility of this measurement is shown in Figure 5.6. The voltage at 900 s was chosen to compare the values, because the voltage after 900 s increases slowly. It is clear that the OCP at 900 s is 1.025 ± 0.004 V under the four identical preparation conditions.

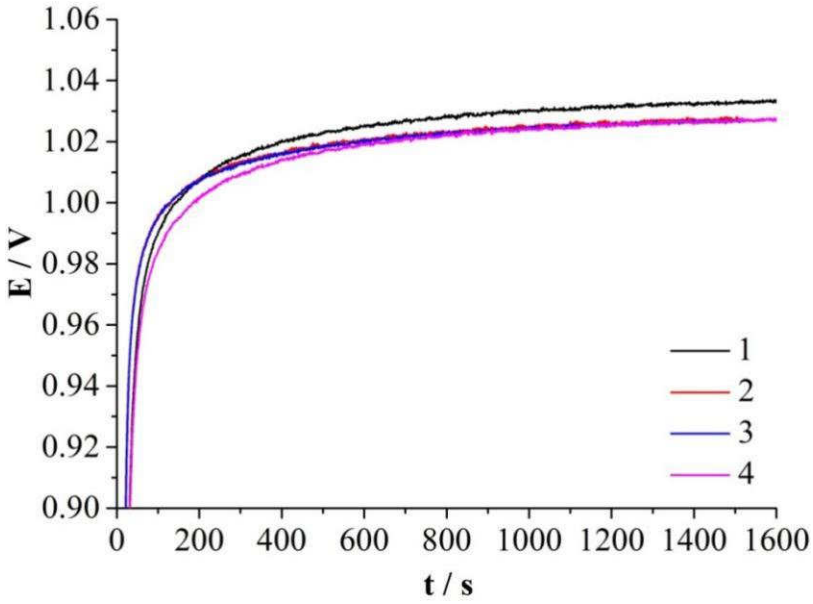

Figure 5.6. The t-E curves of $Pt/C_{20\%\ Pt}$ in 1 M H_2SO_4 at 30 °C under open circuit condition. The results of four measurements under identical test conditions are displayed.

5.3.2 The effect of temperature on OCP

In accordance of the Nernst equation and the study of pure Pt in chapter 3, the higher the temperature, the smaller the OCP value (at 900 s). So the effect of temperature in the normal operational range of 30 °C - 70 °C on the catalyst of Pt on carbon has been studied in this chapter.

Figure 5.7 and 5.8 shows the CV and t-E curve of the catalyst of $Pt/C_{20\%Pt}$ with platinum loading of 20 μg_{Pt} cm^{-2} at different temperatures, respectively. The CV at each temperature displays a similar CV type of Pt. But the positive peak of CV above 0.9 V regions has a little left shift from 30 °C to 70 °C, which implies that the Pt oxidation becomes easier with increasing temperature.

The OCP from 30 °C to 70 °C is shown in Figure 5.8. They have the same curve type, including a fast increasing step and a slow increasing step. With increasing temperature, the OCP value (at 900 s) decreases.

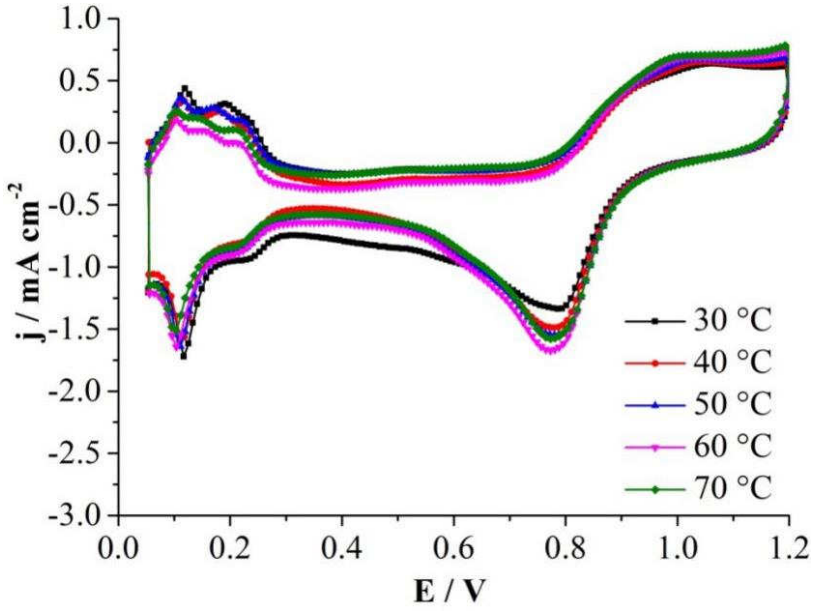

Figure 5.7. The CV curves of $Pt/C_{20\%\ Pt}$ in 1 M H_2SO_4 from 30 °C to 70 °C under O_2 saturation.

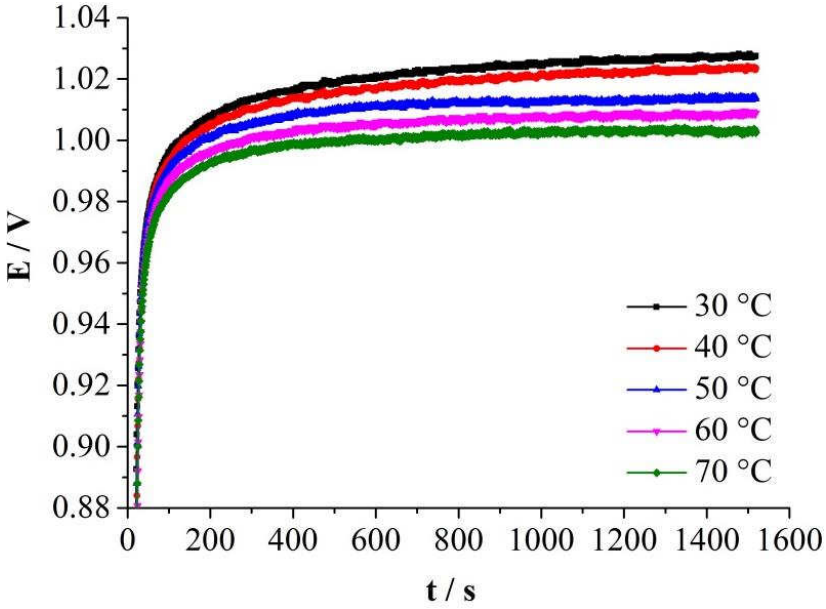

Figure 5.8. The t-E curves of $Pt/C_{20\%\ Pt}$ in 1 M H_2SO_4 from 30 °C to 70 °C under open circuit condition.

5.3.3 The effect of gas composition

Figure 5.9 shows the CV curve of the catalyst of $Pt/C_{20\%\ Pt}$ with platinum loading of 20 μg_{Pt} cm^{-2} at 30 °C with N_2, air and O_2 saturation. It is known from the CV that : a) a cleaned CV of Pt

on Vulcan carbon surface was obtained; b) the potential position is the same under these three conditions; c) the net current negative increases from the condition of N_2 saturation to O_2 saturation; d) the region above 0.9 V is the same.

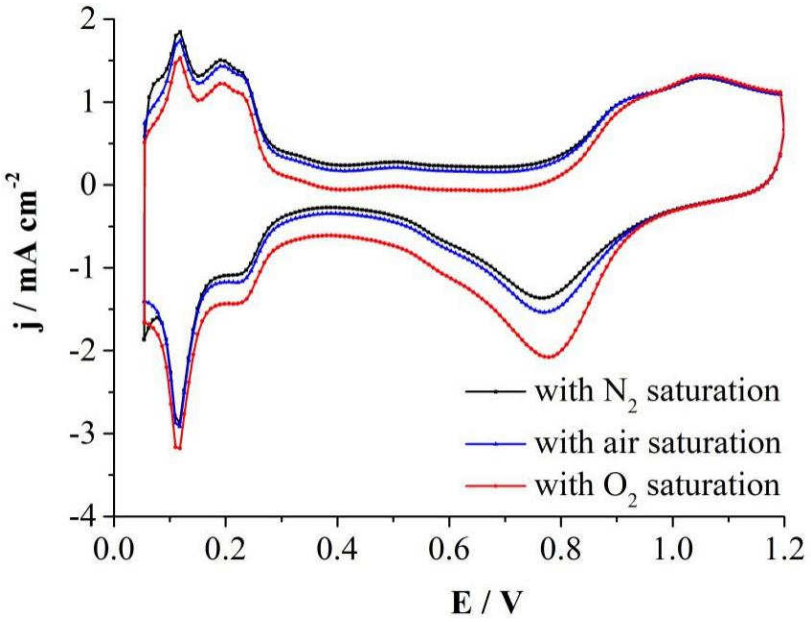

Figure 5.9. The CV of $Pt/C_{20\%\ Pt}$ with O_2, air and N_2 saturation in 1 M H_2SO_4 at 30 °C.

Figure 5.10 and 5.11 show the t-E curve of the catalyst of $Pt/C_{20\%\ Pt}$ with platinum loading of 20 $\mu g_{Pt}\ cm^{-2}$ with N_2, air and O_2 saturation in range of 30 °C - 60 °C and their OCP comparison at 30 °C separately. The OCP curve under O_2 and air shows a similar type, which increases very fast at the beginning (< 300 s), and then increases slowly up to relative stable condition (> 300 s). However, the OCP under N_2 saturation shows a slightly different trend. It needs more time to increase at first (> 800 s), and then more time to increase slowly up to relative stable condition (> 2100 s). The same trend is that the OCP value under relative stable condition decreases with increasing temperature, which consists with the Nernst equation. Additionally, the OCP under stable condition with O_2 saturation is higher than that with air saturation, and higher than that with N_2 saturation. The difference between the value under O_2 and air condition at 30 °C is about 30 mV. This is caused by the different surface oxide coverage as a result of different O_2 concentration.

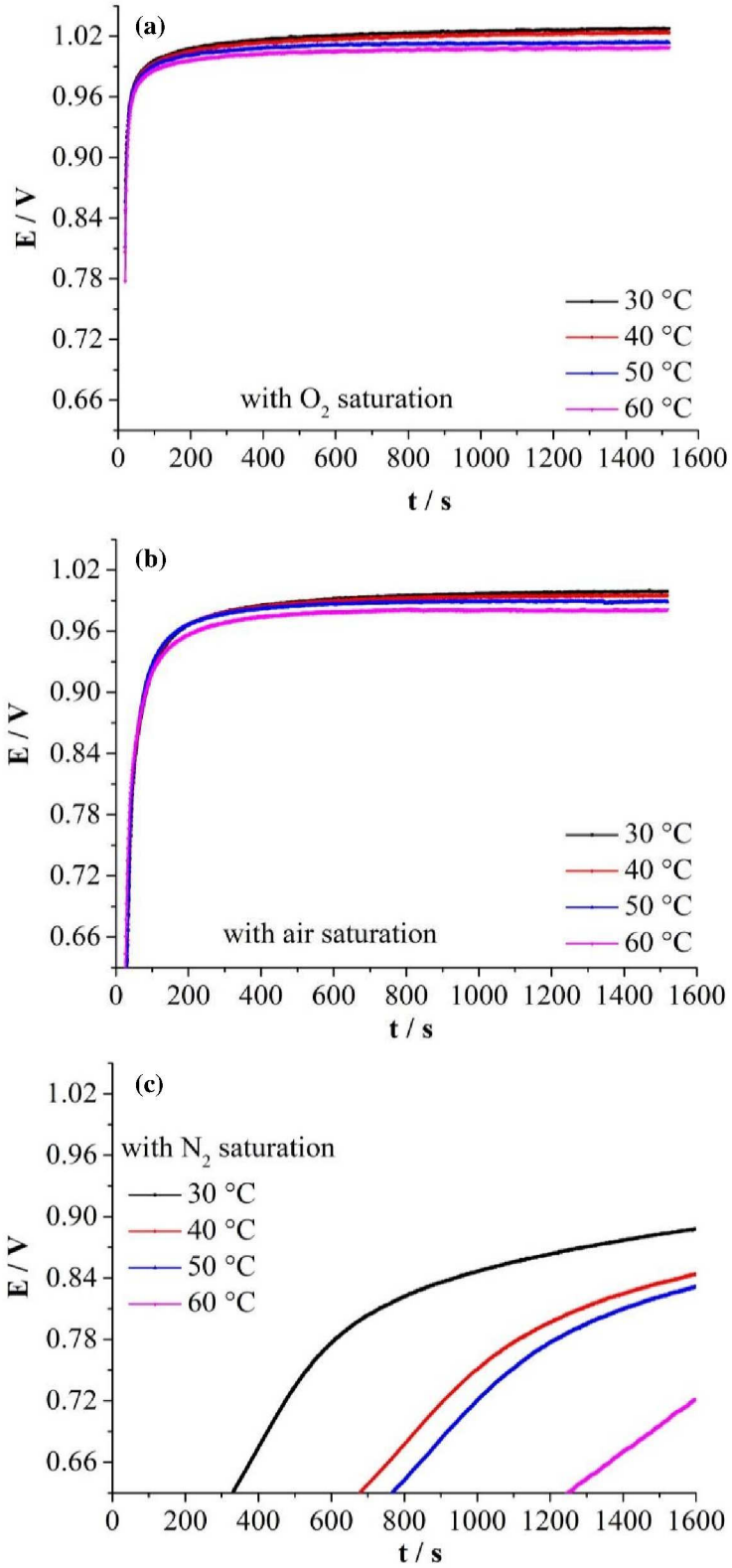

Figure 5.10. (a) The t-E curve of $Pt/C_{20\%\ Pt}$ with O_2 saturation , (b) t-E curve of $Pt/C_{20\%\ Pt}$ with air saturation and (c) t-E curve of $Pt/C_{20\%\ Pt}$ with N_2 saturation in 1 M H_2SO_4 from 30 °C to 70 °C under open circuit condition.

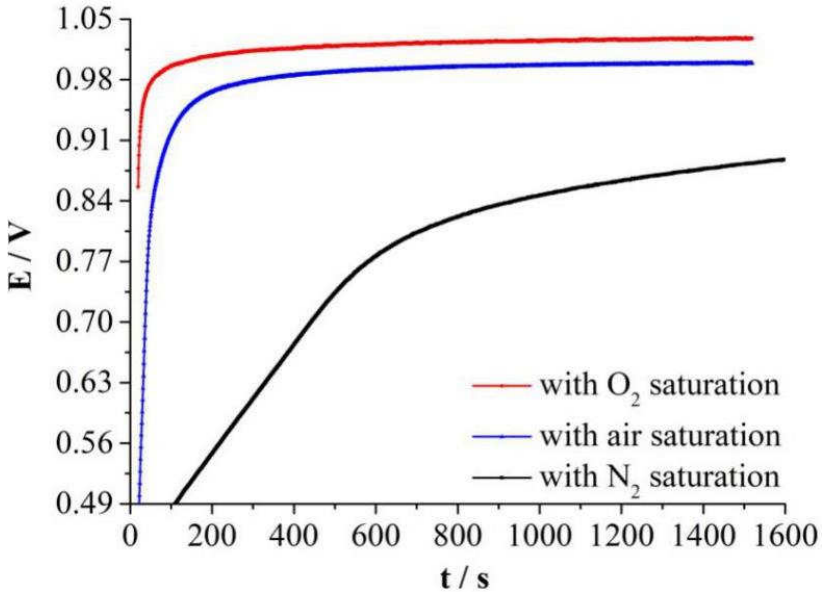

Figure 5.11. The t-E curves of $Pt/C_{20\%\ Pt}$ with O_2, air and N_2 saturation in 1 M H_2SO_4 at 30 °C.

According to the calculation method shown in chapter 2 and the experimental results shown in Figure 5.10, the fitting result, which considers the gas solubility, was shown in Figure 5.12. The graph (a), (b) and (c) relates to the OCP with O_2, and air saturation, respectively. For N_2, the model cannot fit well with the experimental results.

Obviously, the calculation results fit well with the experimental OCP with O_2 and air saturation. However, it does not work for that with N_2 saturation. And the fitting parameters, E^0_{mix} (T) and k, as a function of temperature, is displayed in Figure 5.13. This figure shows the fitting results contained by Equation 2.27.

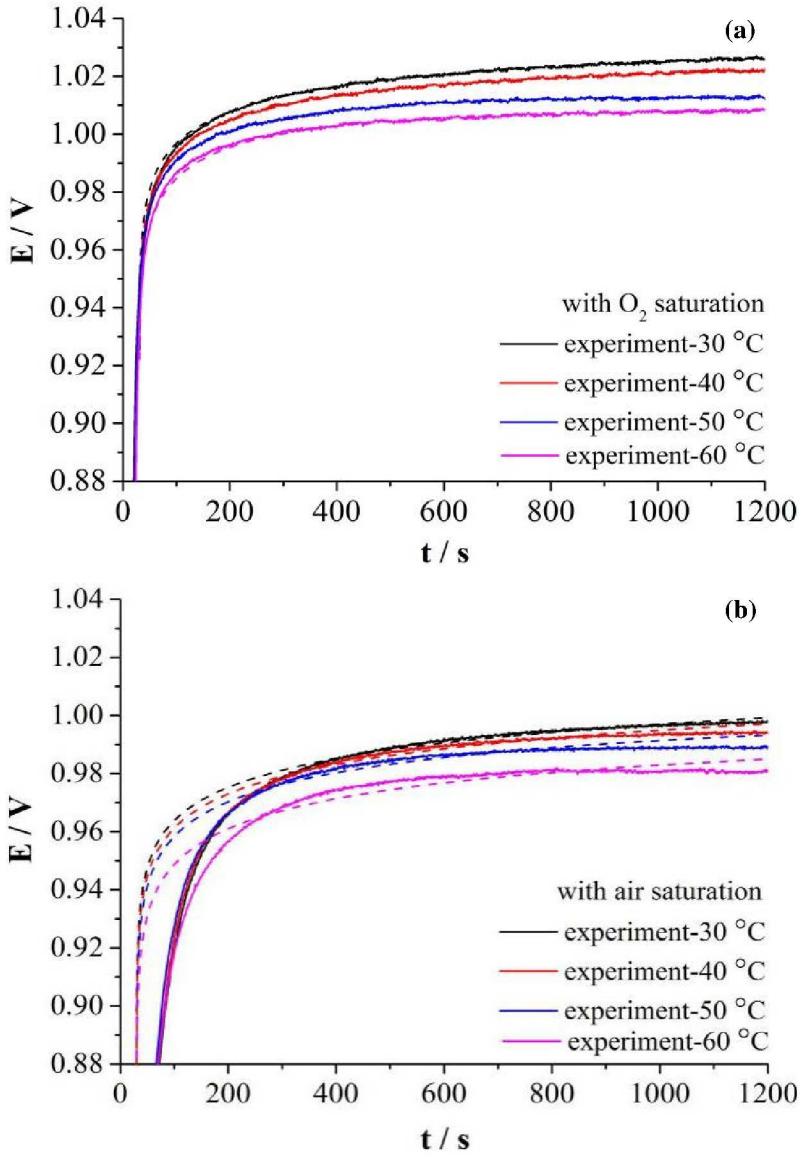

Figure 5.12. The experimental (solid lines) and calculated (dashed lines) t-E of Pt/C $_{20\%\ Pt}$ in 1 M H_2SO_4 from 30 °C to 70 °C with (a) O_2, (b) air saturation.

The same as theory, the $E^{0}_{mix}(T)$ with O_2 saturation is the same as that with air saturation and decreases with increasing temperature in these two cases. Figure 5.13 (b) shows the resulting values for the reaction rate coefficient k as a function of temperature. The absolute value of k is higher for oxygen than for air. This is due to the different surface oxide. A higher oxygen concentration would, in turn, provide a higher surface oxide coverage.

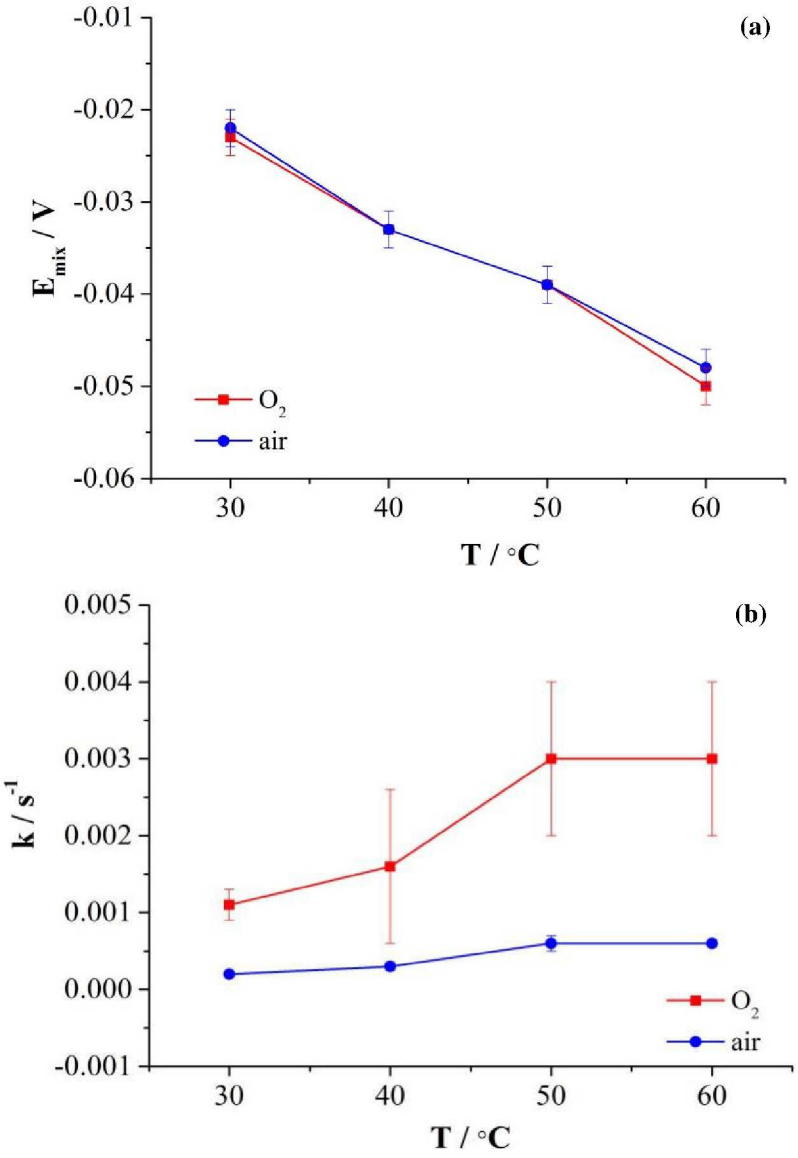

Figure 5.13. Fitting parameters E^{0}_{mix}(T) (a) and k(T) (b) from 30 °C to 80 °C.

The surface fraction of the oxidized species for O_2 and air is shown in Figure 5.14. For oxygen, after 900 s, the surface is almost completely oxidized at 50 °C and 60 °C, while is only covered to 0.6 at 30 °C. For air, after 900 s, about 18% of the surface is covered by oxidized species at T = 30 °C, and even at T = 60 °C, a surface fraction of only 0.4 is reached.

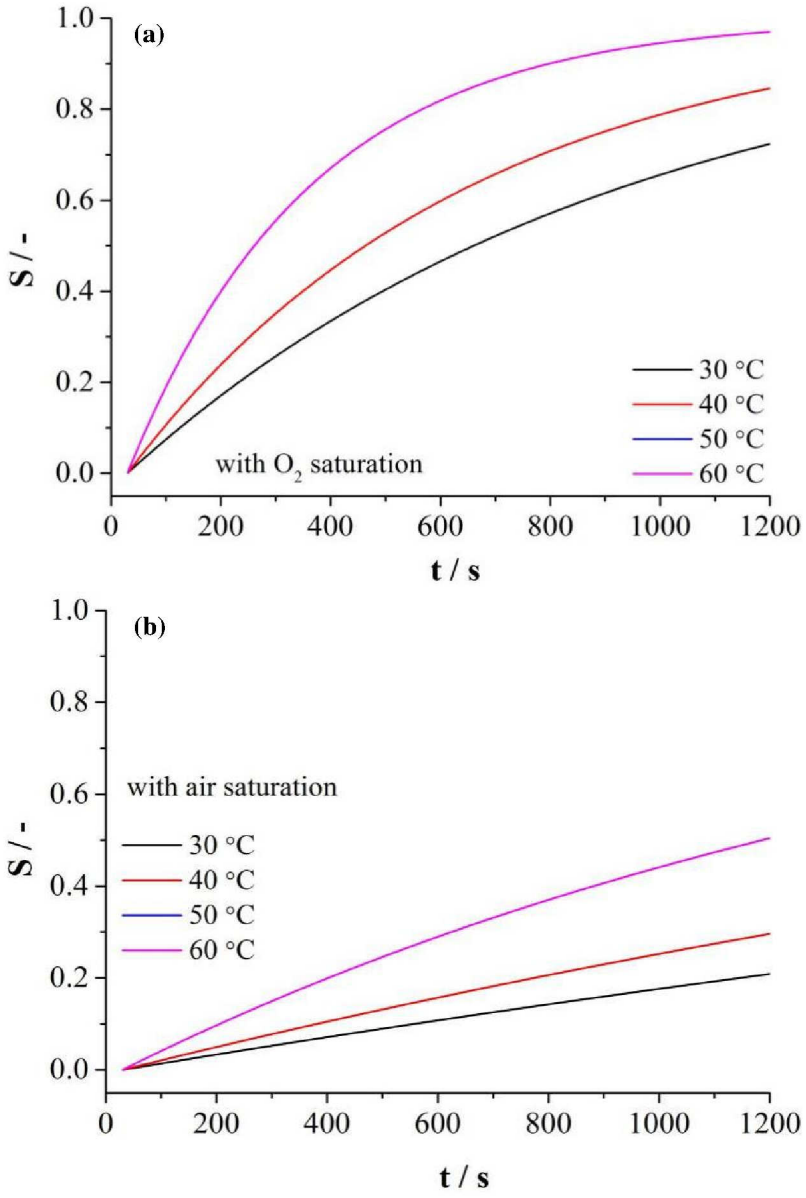

Figure 5.14. Surface coverage S as a function of time with O_2 (a) and air (b) saturation of the electrolyte at different temperatures.

5.3.4 The effect of the ratio of platinum and carbon on OCP

In order to know more about the catalyst layer, the OCP of electrode prepared from various ratio of Pt on carbon support with platinum loading of 20 μg_{Pt} cm^{-2} is observed in this section. The schematic graph of this three films shows in graph 5.1. The CV and OCP curve at 30 °C is shown in Figure 5.15 and 5.16 separately.

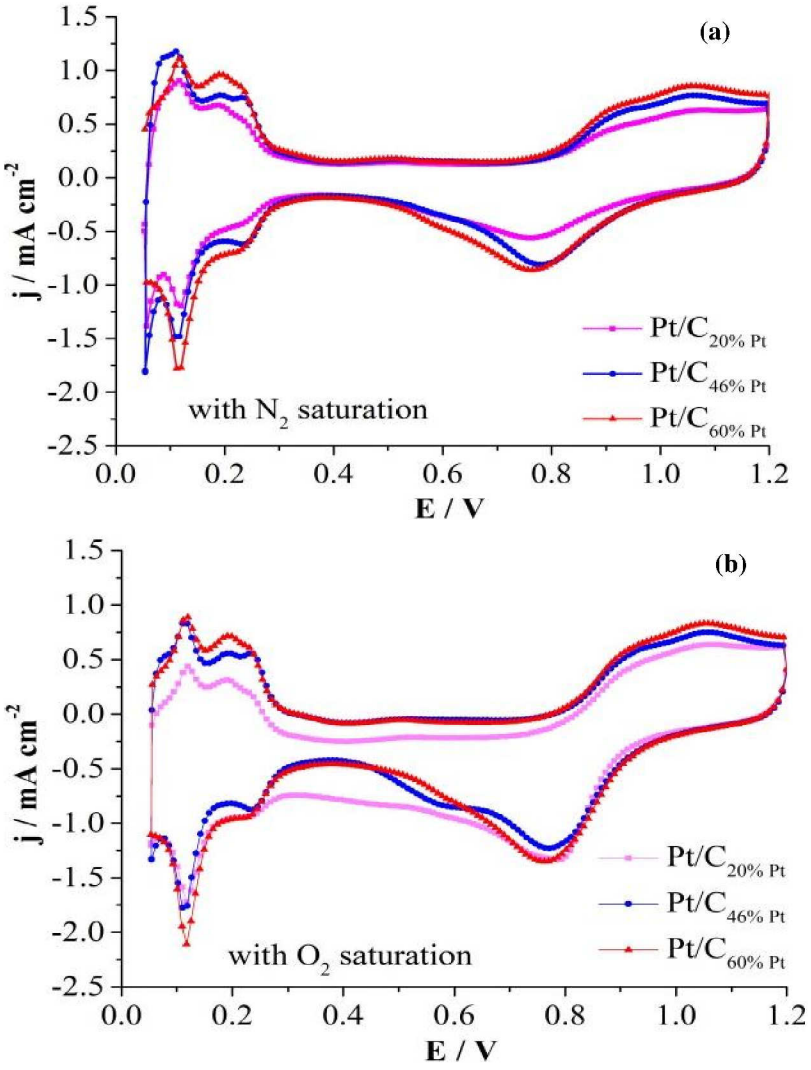

Figure 5.15. The CV (a) under N_2 and (b) under O_2 saturation of $Pt/C_{20\%\ Pt}$, $Pt/C_{46\%\ Pt}$ and $Pt/C_{60\%\ Pt}$ in 1 M H_2SO_4 at 30 °C.

All the CV with N_2 and O_2 saturation (Figure 5.15 a and b) show obvious CV peaks of Pt with one weak positive carbon peak (about 0.5 V) and one weak negative peak (about 0.6 V). The charge of H- adsorption peak of the catalyst $Pt/C_{20\%\ Pt}$, $Pt/C_{46\%\ Pt}$ and $Pt/C_{60\%\ Pt}$ is 444.8, 585.0 and 609.1 μC. Obviously, the higher the platinum ratio is, the higher the charge will be. And it's known in the case of the same amount of platinum loading, the more the platinum ratio, the thinner the film. Thus, the possible reason of this different charge of H- adsorption peak is that the thicker the film, the more serious the agglomeration of the platinum particles, which is caused by the preparation processes. It's known from the t-E curve in Figure 5.16 that for all of the catalyst of Pt on Vulcan carbon, the OCP is smaller than pure Pt. What's more, the OCP

value of $Pt/C_{20\%\ Pt}$ is a little smaller than that of $Pt/C_{46\%\ Pt}$ and $Pt/C_{60\%\ Pt}$. And the OCP of the latter two catalysts is close.

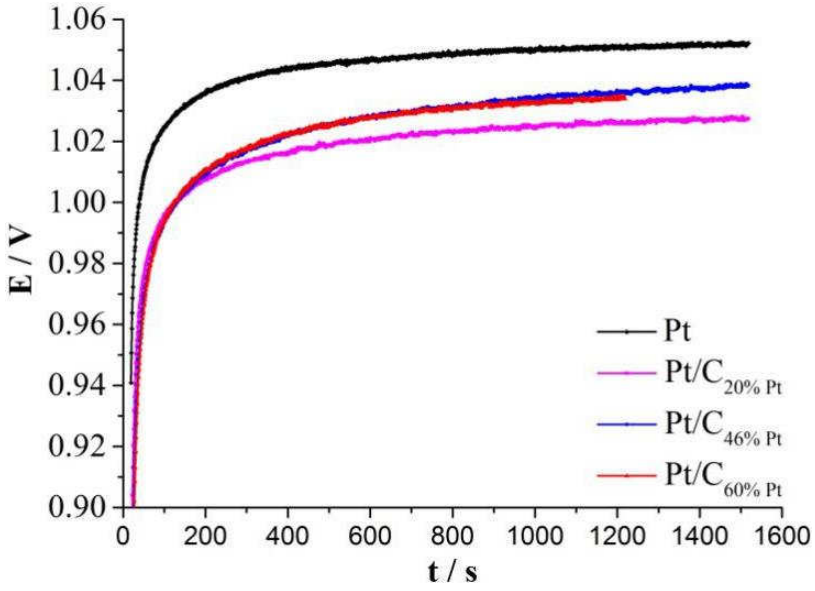

Figure 5.16. The t-E curve of $Pt/C_{20\%\ Pt}$, $Pt/C_{46\%\ Pt}$ and $Pt/C_{60\%\ P}$ in 1 M H_2SO_4 with O_2 saturation at 30 °C under open circuit condition with platinum loading of 20 $\mu g_{Pt}\,cm^{-2}$.

5.3.5 The effect of platinum loading on OCP

Except for the ratio of Pt on carbon support, platinum loading is another controllable factor of catalyst layer. In this chapter, the OCP of $Pt/C_{60\%Pt}$ with different platinum loading was measured.

The CV results and OCP curves are displayed in Figure 5.17 and 5.18. Because the thickness is related to the platinum loading, three different thick catalyst layers are marked by different platinum loading. The higher the platinum loading is, the thicker the film will be.

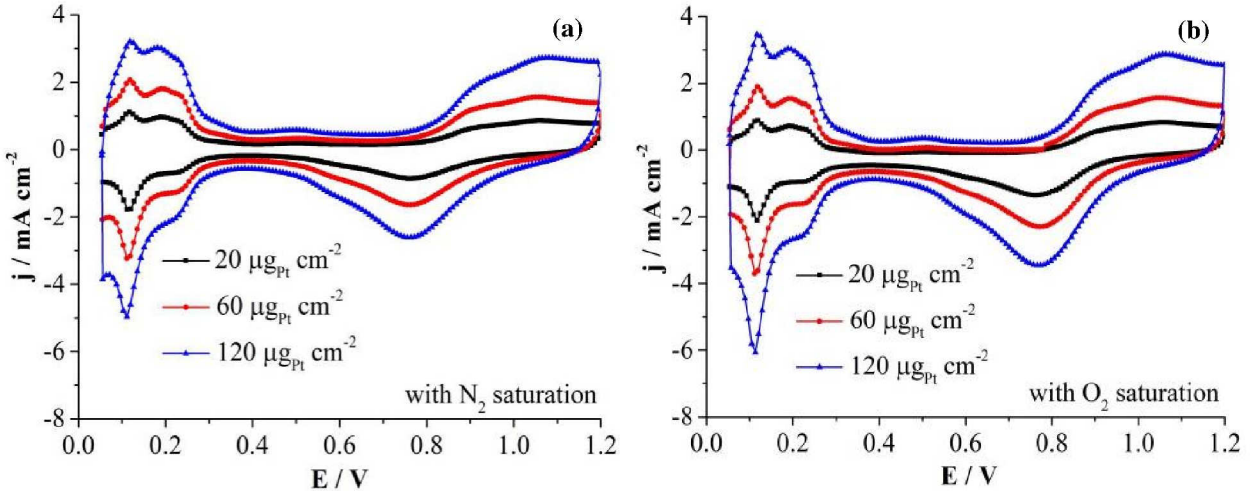

Figure 5.17. The CV of $Pt/C_{60\%\ Pt}$ in 1 M H_2SO_4 with (a) N_2 and (b) O_2 saturation with the platinum loading of 20, 60 and 120 $\mu g_{Pt}\ cm^{-2}$ at 30 °C.

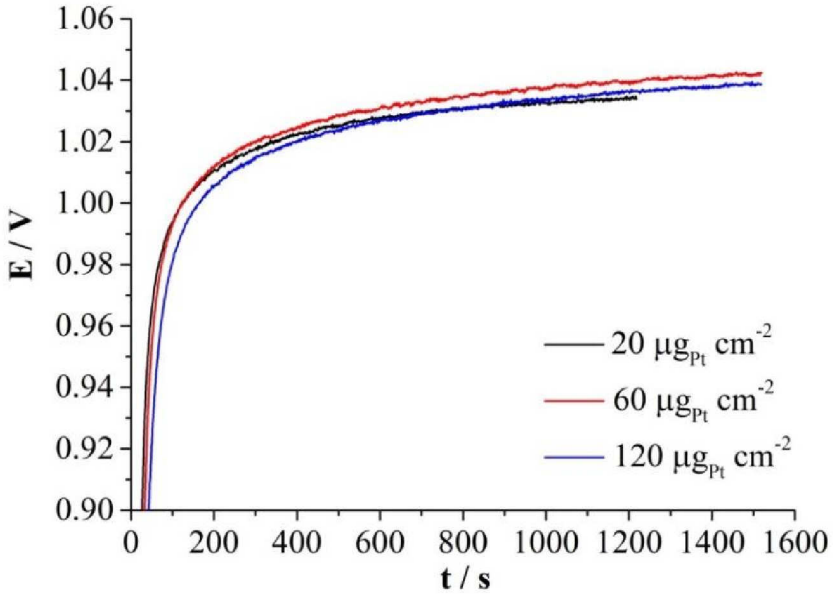

Figure 5.18. The t-E curve of $Pt/C_{60\%\ Pt}$ with the platinum loading of 20, 60 and 120 $\mu g_{Pt}\ cm^{-2}$ in 1 M H_2SO_4 with O_2 saturation at 30 °C.

Compared to the CV under N_2 atmosphere, the CV under O_2 atmosphere has the same potential position, but more negative net current. For these three different thick catalyst layers, the net current density is the same. The phenomenon that the CV in the potential range of 0.95 to 1.2 V is overlapped is the same as that of pure platinum as discussed in chapter 3. The thicker the film is, the bigger the intensity of current density will be. By calculation, the charge of H-

adsorption peak of the catalyst $Pt/C_{60\%\ Pt}$, with platinum loading of 20, 60 and 120 μg cm^{-2} is 609.1, 1170.5 and_1824.5 μC, separately. The reason why the charge amount has the different multiple as the platinum loading is that the more amount the platinum loading, the more serious the agglomeration of the platinum particles.

It can be seen from Figure 5.18 that the OCP of Pt with carbon is lower than that of pure platinum. What's more, these different thick catalyst layers present a close OCP value. And the value at 900 s is 1.034 ± 0.003 V. Compared to the effect of loading on the OCP of carbon support, in which the higher amount of carbon the higher the OCP value, the influence of loading on the OCP of Pt/C is very slight. The role of carbon in the Pt/C is verified to be very small again.

5.4 Summary

(1) The catalyst of Pt on carbon support shows a same shape of t-E curve with that of pure Pt and carbon, which includes a fast reaction step and a slow reaction step, but the value in slow region (about 900 s) is lower than that of Pt. This process is closer to the t-E of platinum than that of carbon.

(2) Increasing temperature, the OCP of the catalyst of Pt on carbon support in the slow region (about 900 s) decreases. Comparing the OCP at 900 s, the OCP at 70 °C is about 22 mV smaller than that at 30 °C.

(3) Comparing the t-E curve of Pt on carbon support with N_2, air and O_2 saturation in 1 M H_2SO_4, the Nernst equation and first order reaction have been used for calculation by using the model of gas solubility, and a good fitting result is obtained.

(4) The catalysts of Pt /C with different ratio have the same shape of t-E curve, and all of them are smaller than the OCP of pure Pt. The OCP of the Pt /C $_{20\%\ Pt}$ is the smallest, as well as the OCP of Pt /C $_{46\%\ Pt}$ and Pt /C $_{60\%\ Pt}$ is close.

(5) Different thickness of catalyst layer shows a close OCP value.

Chapter 6 Single cell experiment

6.1 Introduction

In the previous chapters, the OCP of Pt, carbon support and Pt on carbon support have been studied in the half-cell by the method of linear voltammetry scan and chronopotentiometry. All the t-E curves show a feature that the voltage increases quickly in the first minutes, and then goes to a stable state. Furthermore, the OCP is affected by the temperature and gas solubility/concentration, which decreases with increasing temperature or decreasing gas solubility/concentration. The calculation of developed Nernst equation can fit well with the experimental results, which explains the most OCP loss as the mixed potential of oxygen reduction and platinum oxidation. For the catalyst layer, the OCP can also be influenced by the preparation and materials.

For the single cell, the OCV is known to be affected not only by mixed potential, but also by hydrogen crossover. The over voltage caused by hydrogen crossover is studied in this chapter by calculation and experiment. On the one hand, the over voltage can be calculated by Equation 2.1, which can be accomplished by the crossover current density and charge transfer resistance from the LSV and EIS measurement. On the other hand, the over voltage can be obtained by the difference between the OCV of half-cell and single cell. In addition, the influence of temperature and RH on hydrogen crossover is studied in this chapter.

6.2 The experiment

A special single cell was used, which is called Baltic quickCONNECTfixture (qCf). It is composed of the support frame pressure unit (SFPU) and cell fixture (cf). The details of this cell are shown in chapter 2.

The measurement of the cycle voltammetry, linear sweeping voltammetry, OCV and EIS is applied in this section. Before the measurement, a break-in process was performed, which makes our cell achieve a stable condition.

6.3 Results and discussion

6.3.1 The electrochemical measurement

Here, the results of the singe cell under the conditions where the temperature is 60 °C and the RH of both sides is 100% is shown. This is an example to show the OCV of the single cell. Pure H_2 is used at the anode side.

The polarization curve under air conditions for the cathode is shown in Figure 6.1. The two curves shown in the graph give the condition before and after the test procedure. Clearly, after measurement the polarization curve is a little higher than that before measurement, which means after the measurement including OCV, CV and EIS and so on, the performance of the single cell shows a little improvement.

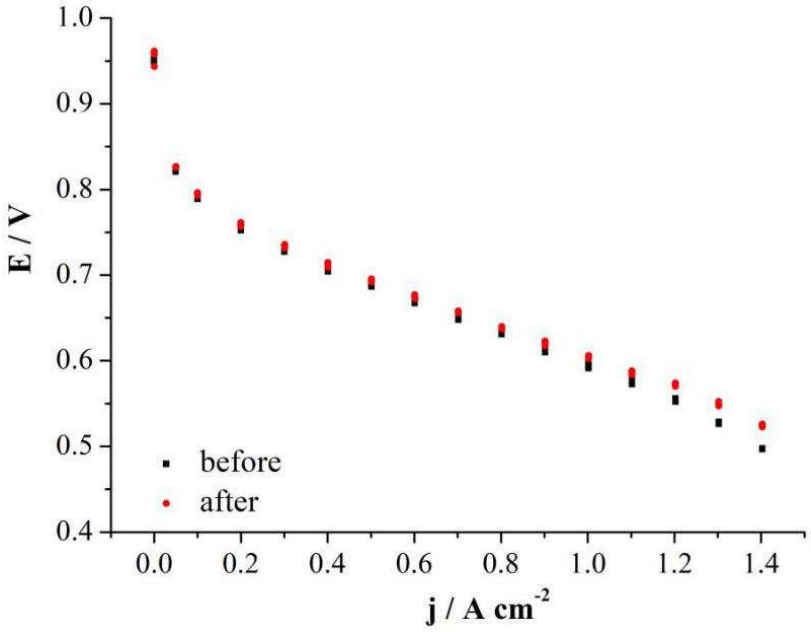

Figure 6.1. The polarization curve of single cell before (black) and after (red) the break-in procedure at 60 °C operated with 100% RH for both side under air for the cathode side.

(1) Cyclic voltammetry and cyclic voltammetry linear scan

Figure 6.2 shows the CV result when the temperature is 60 °C and the RH of both sides is 100%. The curve shows classical Pt and carbon CV peaks. The sharp peak at the minimum

potential is caused by the measurement method, that being the closure of the cell when testing. Namely, there is no inflow and outflow of gas. By calculating from Equation 2.3 [125], the ESA_{Pt} is 49.3 $m^2 g^{-1}$. This is very close to the ECSA of 40% Pt prepared catalysts in the literature [137].

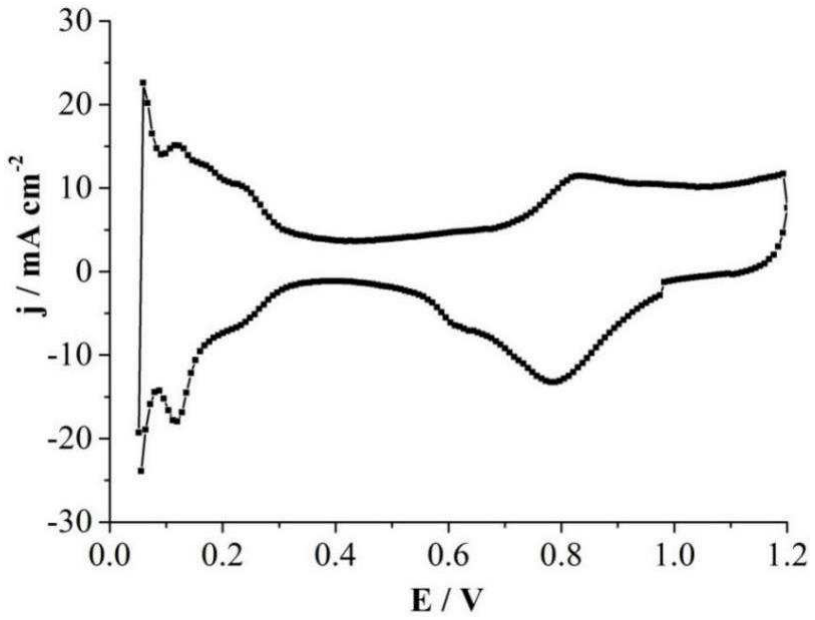

Figure 6.2. The CV curve of single cell at 60 °C with 100% RH for both sides under N_2 for the cathode side.

In order to know the H_2 crossover current, linear sweeping voltammetry is applied by the sweeping rate of 1 mV/s. Figure 6.3 gives the LSV result as the temperature is 60 °C and the RH of both sides is 100%. It is clear that the three curves are not overlapped, but the fluctuations become smaller and smaller from curve 1 to curve 3. Thus, the mean of these three curves is chosen to compare with others. There is a little difference of these curves to the curve of other researchers' [65, 121, 122]. This is due to the measurement operation, on which there is no inflow and outflow of gas. The crossover current density according to this Figure is 1.558±0.071 mA cm^{-2}. According to Pei's statement [123], the crossover current density is influenced by the sweeping rate if the method in this thesis is used. And the faster the sweeping rate, the higher the crossover current density. Compared to other literature, our crossover current density is a little higher, see Table 6.1.

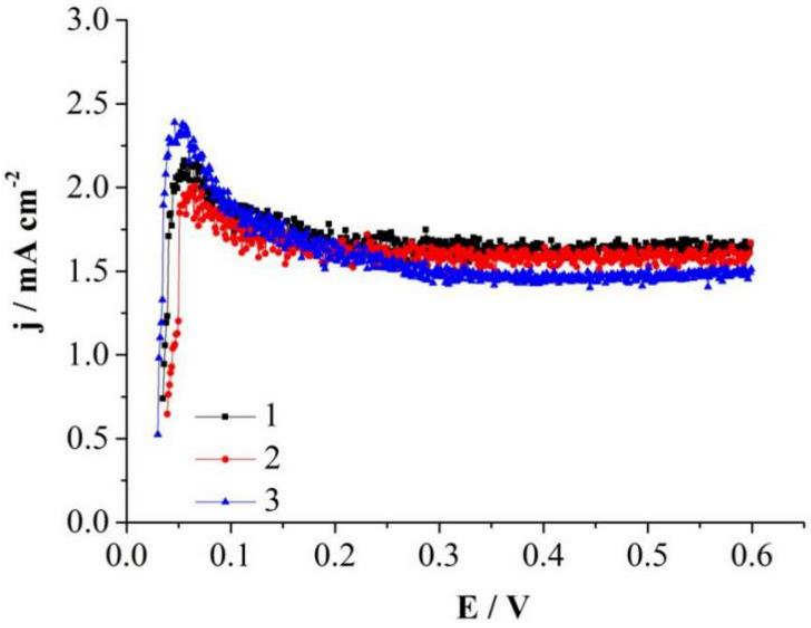

Figure 6.3. The LSV curve of single cell at 60 °C with 100% RH for both sides under N_2 condition for the cathode side. Three different measurements at the same conditions are presented in order to demonstrate the reproducibility.

(2) Electrochemical impedance spectroscopy

Figure 6.4 displays Nyquist plot of the EIS results when the temperature is 60 °C and RH of both sides is 100%. It is clear that the curve shows a single semicircle loop. This is the typical Nyquist plot of PEFC at OCV condition [115] , in which case the electrode process is dominated only by the inter facial kinetics of the ORR process. This measurement is to test charge transfer resistance, and also to test that the cell is functioning properly. The charge transfer resistant, R_{CT}, has been marked in this Figure. Obviously, it is bigger under O_2 conditions (3.688 Ω) than that under air conditions (2.942 Ω). More details about impedance at OCV are presented in the appendix.

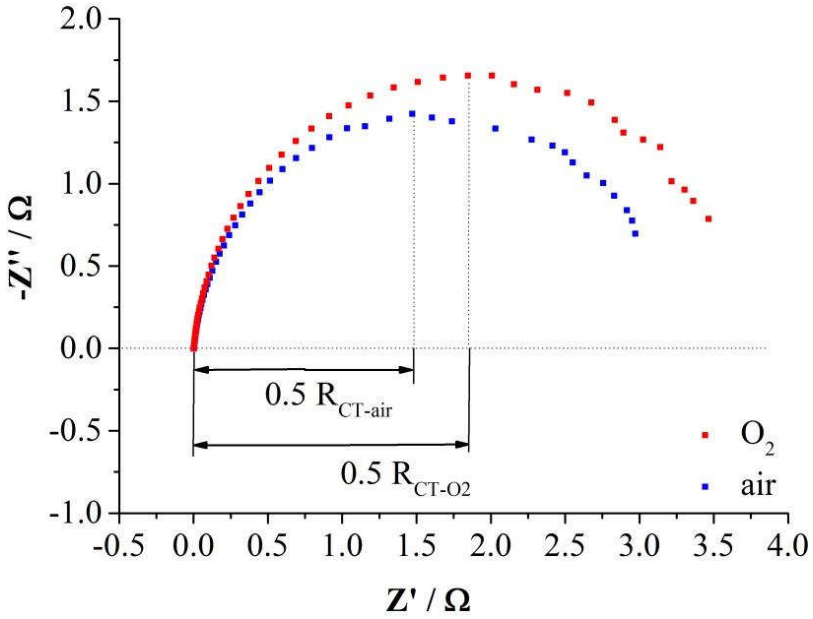

Figure 6.4. The EIS curve of single cell at 60 °C with 100% RH for both sides under air and O_2 condition for the cathode side at OCV conditions.

In order to compare our EIS result to other literature, the charge transfer resistant can be calculated to get the exchange current density, $j^0_{O_2}$, by the Equation 2.2. Table 6.1 gives their related comparison. According to the Equation 2.1, the over voltage can be calculated, which is 0.144±0.007 V. This value is a little smaller than in some other literature, as shown in Table 6.1.

Table 6.1. The parameters: exchange current density ($j^0_{O_2}$), crossover current density (j_C) and the calculated overvoltage (η_C) from Equation 2.1 caused by hydrogen crossover in PEFC.

number	Source	Testing condition	$j^0_{O_2}$ / mA cm^{-2}	j_C / mA cm^{-2}	η_C / V
1	This work	60 °C , 100%RH,	7.8×10^{-4}	1.558±0.071	0.144
2	T. Thampan. *et al.*[138]	80 °C , 100%RH,	1×10^{-7}	/	0.22
3	J. Laraminie. *et al.*[29]	/	4×10^{-5}	2	0.3
4	M. Inaba. *et al.*[99]	60 °C , 100%RH,	/	0.6	/
5	P. Spinelli. *et al.*[139]	70-80 °C , 100%RH,	$5.3\text{-}10\times10^{-4}$	0.18-0.24	0.3
6	*C. Francia. et al.* [140]	60 °C , 100%RH,	/	0.12-0.22	/
7	*P.Pei. et al.*[123]	50 °C , 100%RH,	/	1.306±0.036-1.312±0.04 7	/
8	N.Wagner. *et al.*[117]	50-80 °C , 100%RH,	6×10^{-3}	/	/
9	S.S. Kocha. *et al.*[97]	65 °C , 100%RH,	/	1.5/2.5	/

(3) OCV measurement

The potential holding and t-E curves on the open circuit condition is shown in Figure 6.5 when the temperature is 60 °C and RH of both side is 100%. Obviously, no matter whether the cathode is air or O_2, the twice repeated t-E curves are the same, namely, a stable t-E curve is obtained. The OCV value changes with time, increasing very fast at first, about 20 s, and then decreases to a stable condition (5 mV/180 s). The OCV value (at 900 s) under O_2 condition (0.986 V) is about 30 mV higher than that under air condition (0.954 V). This value is much smaller than that of half-cell, which is 1.034 V and 1.018 V with O_2 and air saturation, separately, when the electrode is pure platinum.

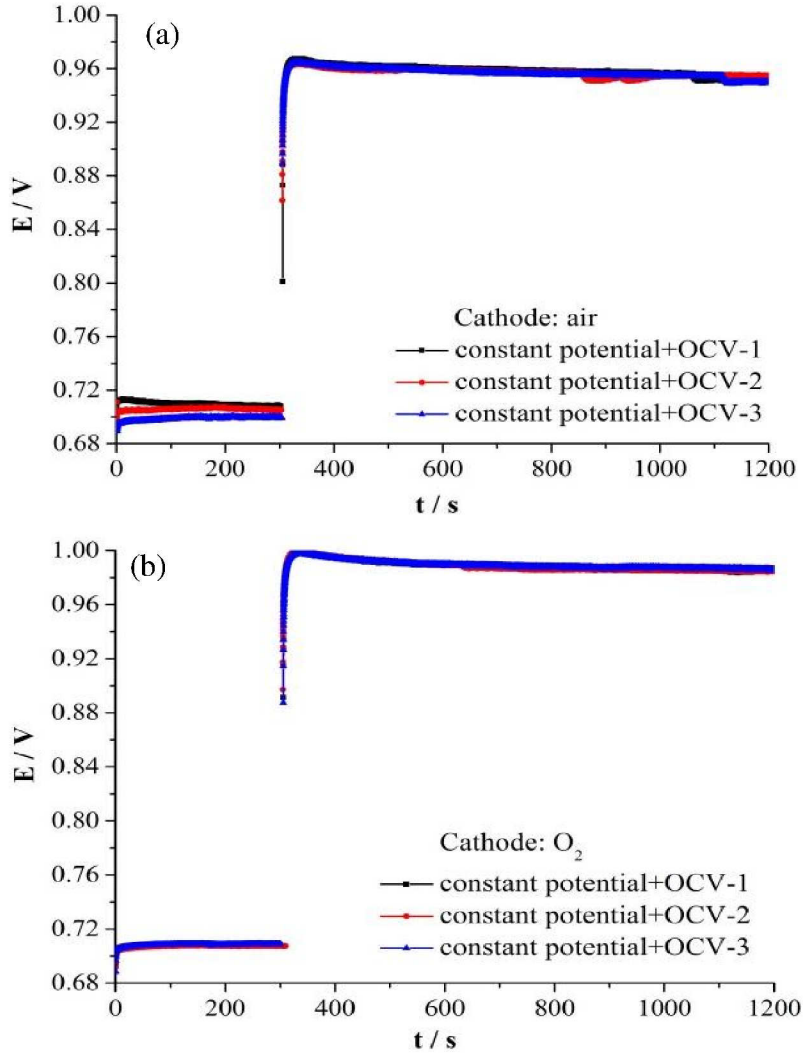

Figure 6.5. The potential holding and t-E curve of a single cell on the open circuit condition at 60 °C with 100% RH for both sides and feeding (a) air and (b) O_2 for the cathode. The measurements are repeated twice under the same operating conditions in order to demonstrate the repeatability.

Figure 6.6 gives the t-E curve of single cell and half-cell at 60 °C and 100% RH for the O_2 on the cathode side. Considering the unknown of the ratio of Pt/C in single cell, here, the data of Pt and three different ratio of Pt/C with platinum loading of 20 μg_{Pt} cm^{-2} is given. It is clear that the OCP increases fast at first, which is about 20 s and 300 s for single cell and half-cell, separately. Then, the OCP of half-cell shows a slow increasing slope, while the OCV of the single cell decreases slowly.

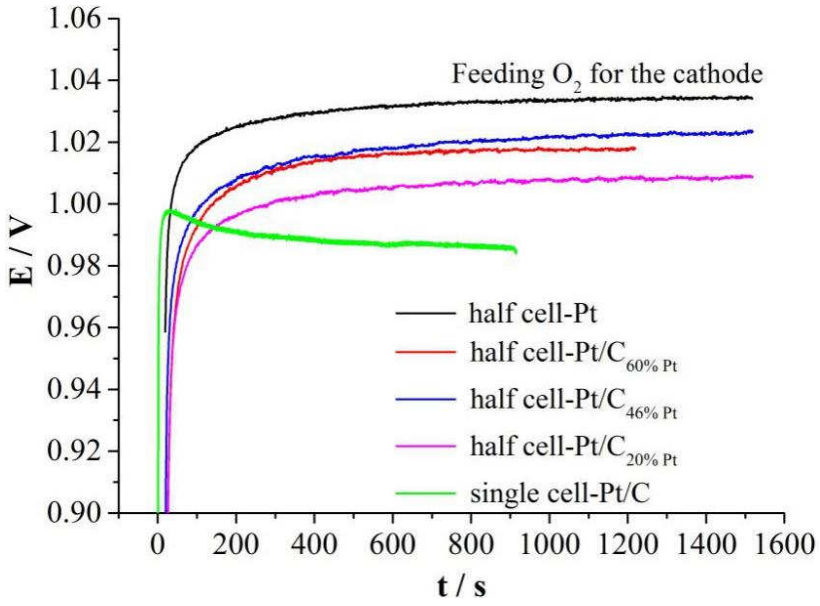

Figure 6.6. The comparison of the t-E curves of half-cell at 60 °C with O_2 saturation for Pt, Pt/$C_{60wt\%Pt}$, Pt/$C_{46wt\%Pt}$ and Pt/$C_{20wt\%Pt}$ and the t-E curves of single cell at 60 °C with 100% RH for both sides and feeding O_2 for the cathode. The Pt loading in the three cases with Pt/C catalyst is in all cases 20 $\mu g_{Pt}\ cm^{-2}$.

(4) Over voltage caused by hydrogen crossover

The OCV (or OCP) of half-cell and single cell is known, thus, the over voltage caused by hydrogen crossover is the difference, as shown in Figure 6.7 (a). The same method is applied to the condition when the cathode is air, and the result is shown in Figure 6.7 (b). Obviously, the overvoltage caused by hydrogen crossover increases with time. Moreover, the minimum and maximum over potential, at 900 s, is 21 and 48 mV for O_2, separately, and 31 and 64 mV for air, separately, in which the OCP value of half-cell comes from the t-E of pure platinum solid disk and catalyst layer of Pt/$C_{20.wt\ \%\ Pt}$ (20 $\mu g_{Pt}\ cm^{-2}$). Clearly, this experimental over potential, the difference between the OCP of half-cell and the OCV of single cell, is much smaller than the calculated over potential, from Equation 2.1. In both cases of O_2 and air, they are 0.144±0.007 V and 0.115±0.005 V, separately. The possible reason is shown in Figure 6.8.

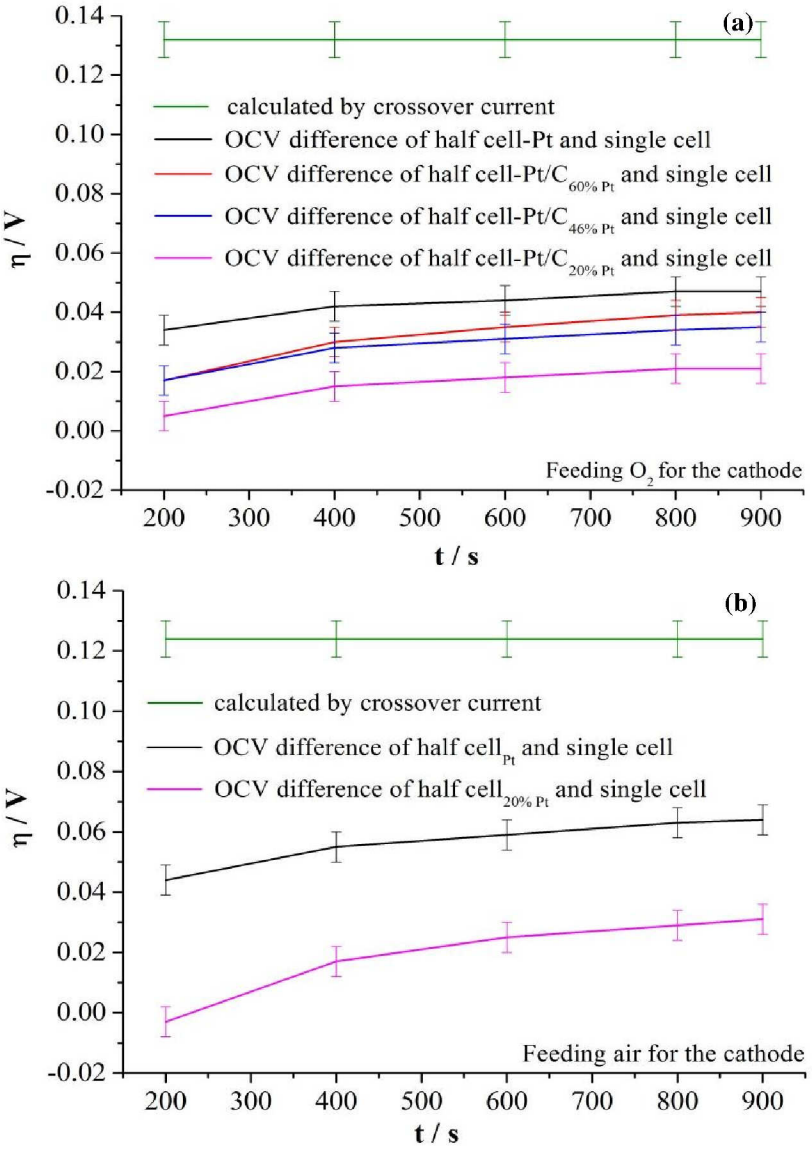

Figure 6.7. The comparison of calculated (from Equation 2.1) and experimental (OCV difference of single cell and half-cell) t - η at 60° C for (a) O_2 and (b) air on the cathode.

Figure 6.8 (a) gives the normal reaction on the cathode electrode with hydrogen crossover from anode to cathode. The hydrogen loose electrons on the surface of the cathode and produces protons, then the electrons and protons are offered to the reaction with O_2 to form water. In this case, the over voltage is just equal to the calculated one from Equation 2.1. Because the crossover current density from LSV measurement corresponds to the reaction of hydrogen oxidizing to protons and the charge transfer resistance from EIS measurement under open circuit condition corresponds to the reaction of protons and O_2 to form water.

However, the experimental over voltage from the OCV difference is smaller than the calculation one from Equation 2.1. Thus, there must be more processes happening. One possibility is that the hydrogen directly reacts with O_2 and produces water, as shown in Figure 6.8 (b). This process does not produce additional charge transfer on the cathode surface, and thus there is no contribution to over voltage. Another probability is that the electrons and protons from hydrogen are offered to the reaction with platinum oxide species to form pure platinum, as shown in Figure 6.8 (c). Therefore, the real condition is the coexistence of these three cases, as shown in Figure 6.8 (d). It just explains well why the experimental over voltage caused by hydrogen crossover is lower than the calculated one. Additionally, the varying O_2 concentrations in the case of O_2 and air make their ratio placements differ.

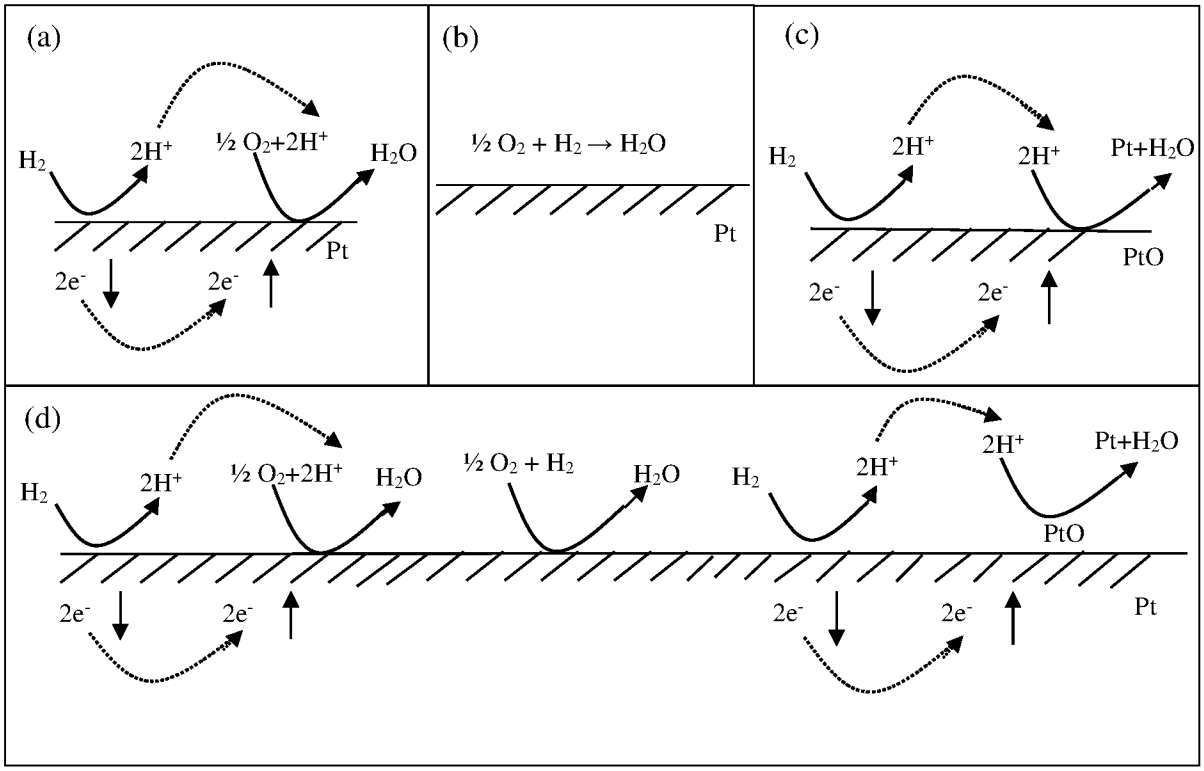

Figure 6.8. The schematic representation of hydrogen reaction on the cathode surface. (a), (b), (c) and (d) represent different possible reactions. Details can be found in the main text.

6.3.2 The effect of temperature on OCV

It's known that temperature has an effect on the OCV of fuel cells. The influence from 40 °C to 80 °C is studied in this section. Figure 6.9 (a), (b) and (c) gives the polarization curve before and after the measurement including LSV, OCV, EIS, etc. It can be seen that the higher the temperature, the better is the performance of the cell which is presented in figure 6.9 (d). The cell is improved after measurement when the temperature is 40 °C and 60 °C. The improvement is larger at 40 °C than that at 60 °C. At 80°C the situation changed. The cell after the measurement shows a slightly lower performance than before the measurement.

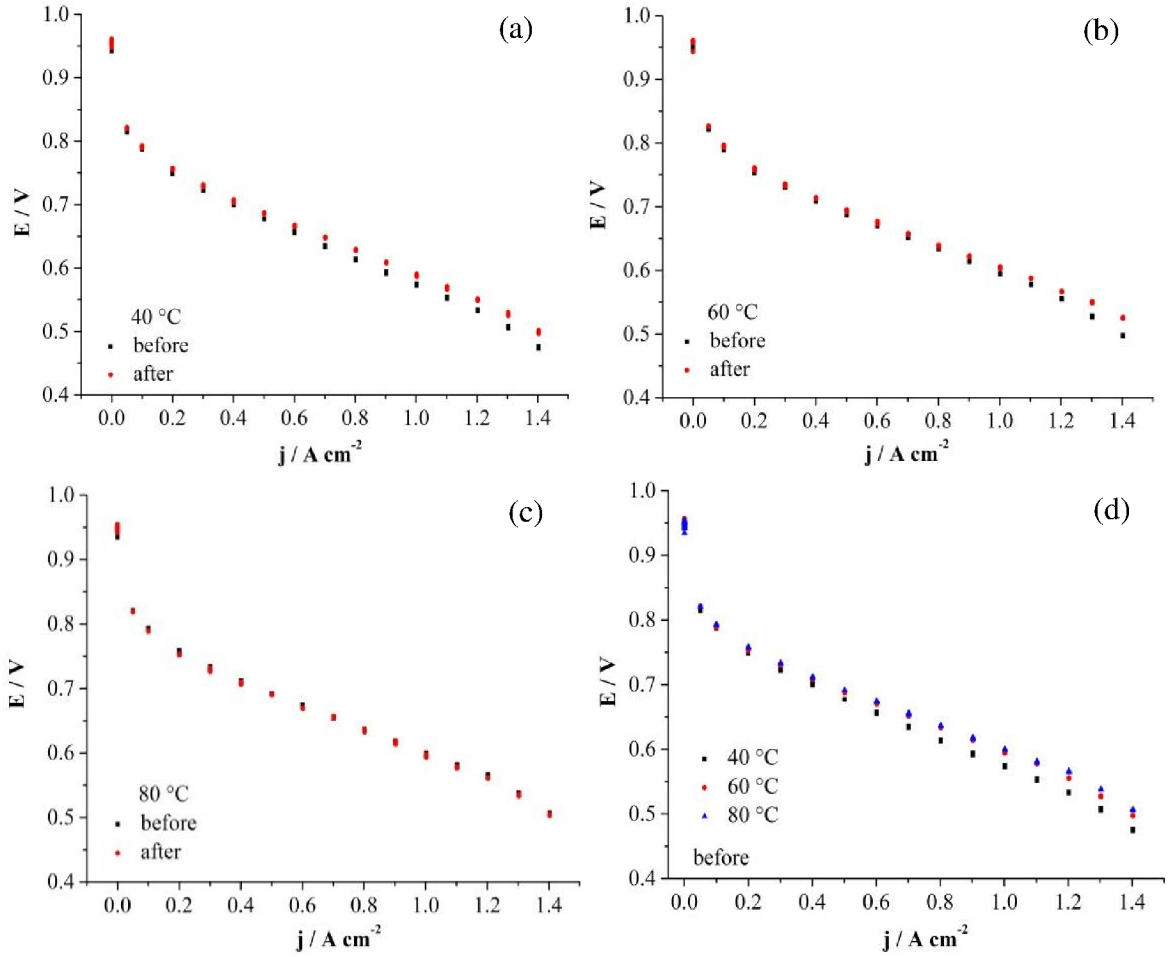

Figure 6.9. The polarization curve of single cell at (a) 40 °C, (b) 60 °C, (c) 80 °C before and after the measurement and (d) their comparison before the measurement with 100% RH for both sides under air condition for the cathode side.

The LSV result is shown in Figure 6.10, displaying the LSV curve of single cell at 40 °C, 60 °C and 80 °C with 100% RH for both sides. Obviously, the LSV shows a feature that the higher the temperature gets, the higher the current density becomes. It means that as the temperature increases, the hydrogen crossover becomes more serious. This agrees with other researchers [99, 140]. The same method as above is used to get the crossover current, and the result is displayed in Table 6.2.

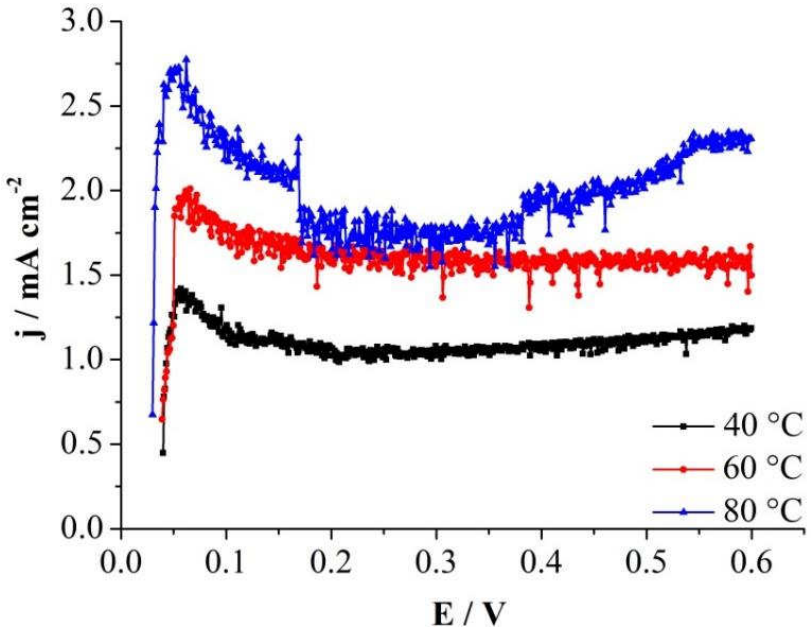

Figure 6.10. The LSV curve of single cell at at 40 °C, 60 °C and 80 °C with 100% RH for both sides.

Table 6.2. The crossover current density at different temperature.

	40 °C	60 °C	80 °C
j_C/ mA cm^{-2}	1.058±0.029	1.558±0.071	1.864±0.060

Additionally, the EIS result is shown in Figure 6.11, including the EIS curve of single cell at 40 °C, 60 °C and 80 °C with 100% RH for both sides under air and O_2 condition for the cathode side. The EIS result of PEFC displays a typical half circle type. After measurement, the charge transfer resistance is obtained. Obviously, it is bigger under O_2 conditions than that under air conditions. Under O_2 conditions, the higher the temperature, the smaller the R_{CT}, which is the same trend as literature [102] when temperature is below 100 °C. However, under air conditions,

the R_{CT} is close at 60 °C and 80 °C, which is smaller than that at 40 °C. The value of R_{CT} is shown in Table 6.3.

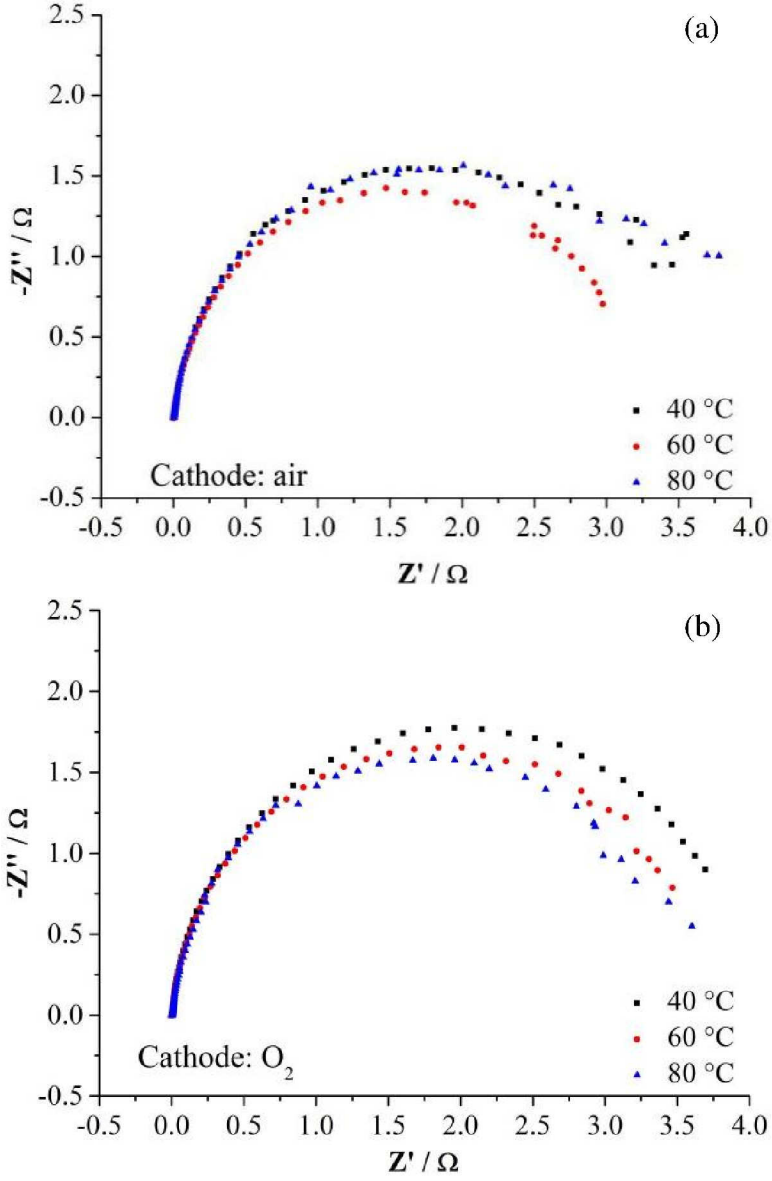

Figure 6.11. The EIS curve of single cell at 40 °C, 60 °C and 80 °C with 100% RH for both sides and feeding (a) air and (b) O_2 for the cathode at OCV conditions.

Table 6.3. The charge resistance and calculated over voltage from Equation 2.1 caused by hydrogen crossover at different temperatures.

	Feeding O_2 in the cathode			Feeding air in the cathode		
	40 °C	60 °C	80 °C	40 °C	60 °C	80 °C
R_{ct} / Ω	3.909	3.688	3.616	3.576	2.942	3.115
η_C / V	0.103±0.003	0.144±0.007	0.168±0.005	0.095±0.003	0.115±0.005	0.145±0.005

From the crossover current density and the charge transfer resistance, the over voltage from 40 °C to 80 °C can be calculate by Equation 2.1. The result is shown in Table 6.3. It was found that the over voltage is increasing with increasing temperature, and the over potential under O_2 conditions is 20 - 30 mV bigger than that under air conditions.

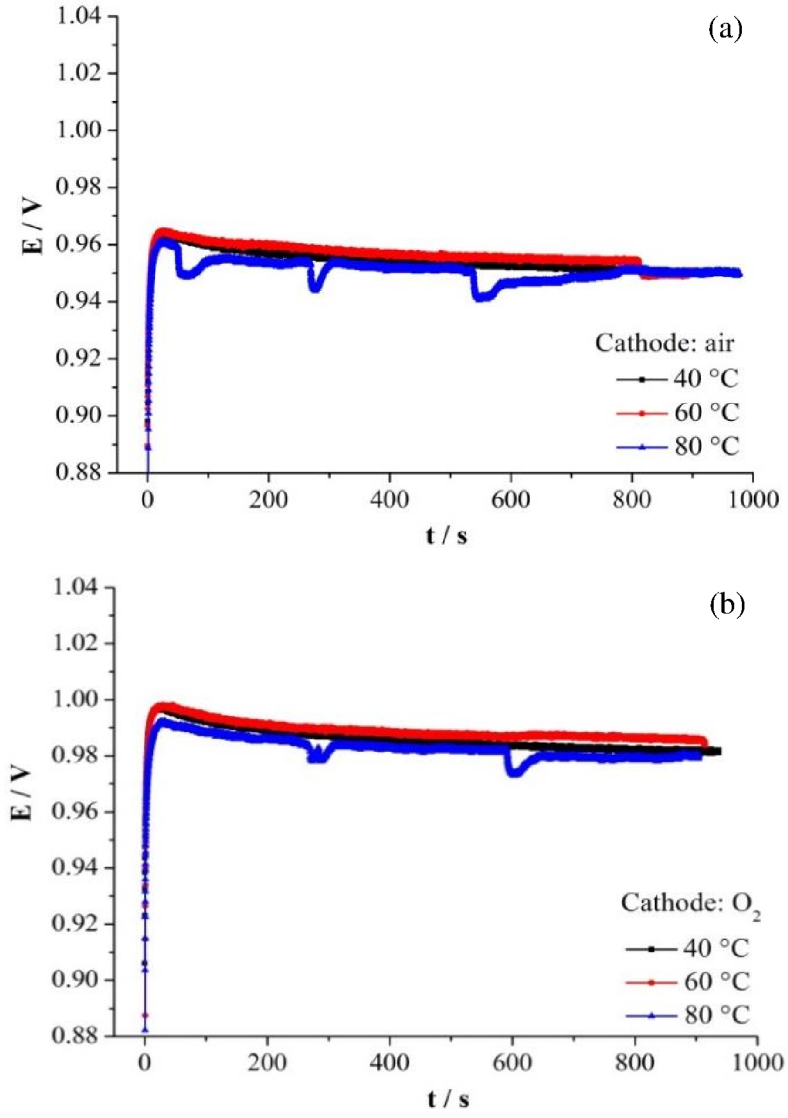

Figure 6.12. The t-E curve of single cell at 40 °C, 60 °C and 80 °C with 100% RH for both sides and feeding (a) air and (b) O_2 for the cathode.

The t-E curve of single cell at 40 °C, 60 °C and 80 °C with 100% RH for both sides under air and O_2 conditions for the cathode shows in Figure 6.12, in which graph (a) and (b) presents that the cathode side is fed air and O_2, separately. It is clear that all the t-E curve shows a character that the OCV value increases fast at first (~ 20 s), and then decreases slowly up to a stable state. For both conditions, the OCV value at 40 °C is similar to that at 80 °C and about 5 mV lower than that at 60 °C. Moreover, the OCV value for O_2 is about 30 mV higher than for air. As above, the over voltage can be obtained by calculation (from Equation 2.1) and OCV experiment (OCV difference between single cell and half-cell). Table 6.4 gives the experimental results of the OCV from single cell experiment, OCP of pure Pt solid disk from half-cell experiment and the over voltage, η_C, at 900 s.

Table 6.4. The OCV and OCP value (at 900 s) and experimental over voltage (η_C) (at 900 s) caused by hydrogen crossover at different temperatures.

	Feeding O_2 in the cathode			Feeding air in the cathode		
	40 °C	60 °C	80 °C	40 °C	60 °C	80 °C
$OCV_{single\ cell}$ / V	0.982	0.986	0.979	0.950	0.954	0.950
$OCP_{half\text{-}cell}$ / V	1.045±0.005	1.034±0.005	1.014±0.005	1.028±0.005	1.018±0.005	0.997±0.005
η_C / V	0.063±0.005	0.048±0.005	0.035±0.005	0.078±0.005	0.064±0.005	0.047±0.005

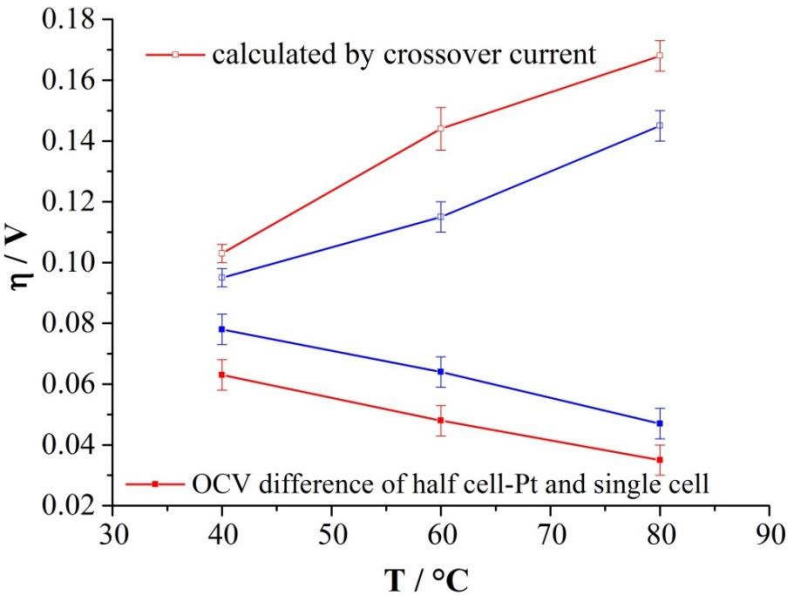

Figure 6.13. The comparison of calculated (empty symbol) and experimental (full symbol) t-η when the cathode is O_2 (red) and air (blue) at different temperature.

Figure 6.13 displays the over voltage caused by hydrogen crossover obtained from calculation and experiments, in which the half-cell data comes from the OCP of pure Pt solid disk. Clearly, the results at 40 °C and 80 °C show a similar tendency to that at 60 °C. Clearly, the over voltage from calculation increases with increasing temperatures, and the value for O_2 is higher than for air. This is caused by increasing crossover current density with increasing temperature, and the charge transfer resistance under O_2 is higher than for air. However, the real over voltage from experiments decreases with increasing temperatures, and the value for O_2 is lower than for air. An explanation is that the higher temperature is directly helping the reaction of H_2 with O_2 to form water and the reaction of platinum oxide reducing to pure platinum.

6.3.3 The effect of RH on OCV

It is known that gas concentration has an effect on the OCV of a fuel cell, which is influenced in the single cell by the relative humidity. In this section, the case of the relative humidity of 100%, 75% and 50% for the cathode is studied. For the anode, the relative humidity is always 100%.

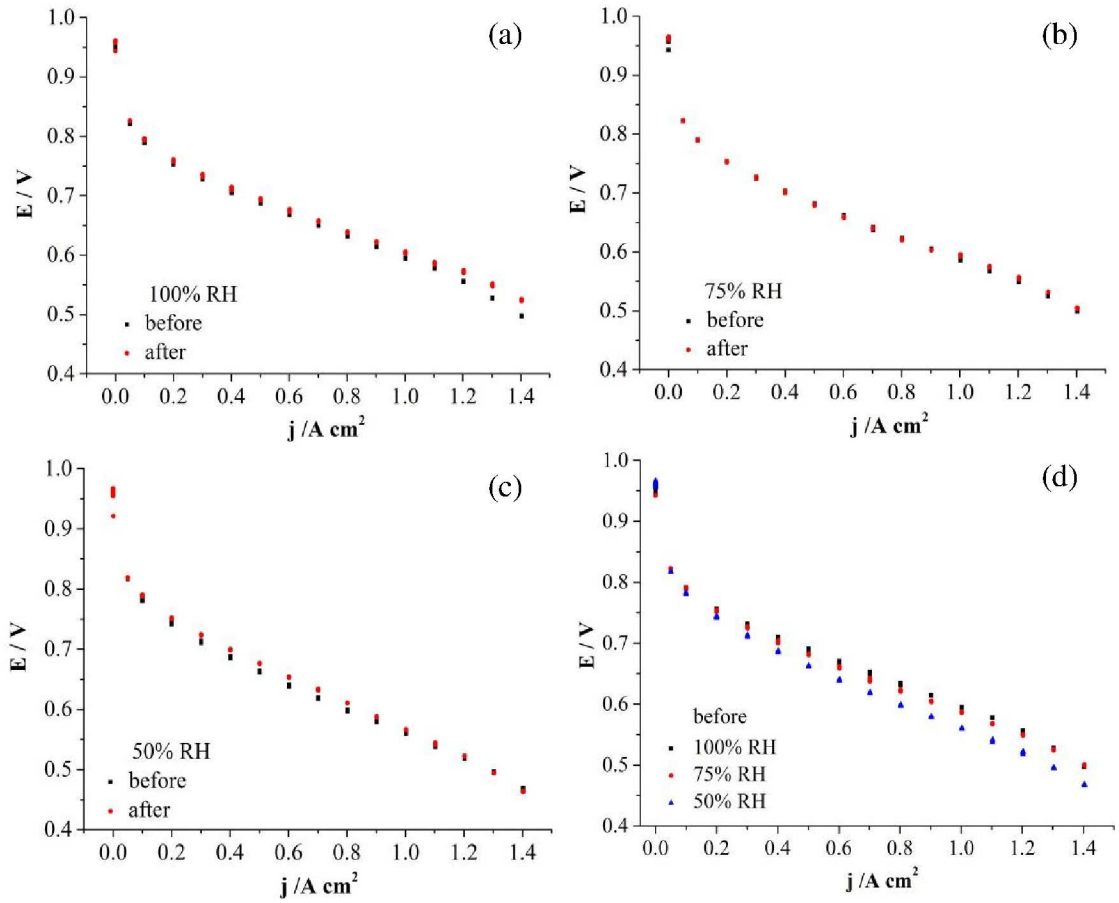

Figure 6.14. The polarization curves of single cell at 60 °C with (a) 100%, (b) 75%, (c) 50% RH for the cathode before and after the measurement and (d) their comparison before measurement.

The polarization curves before and after the measurement at different humidity conditions for the cathode is displayed in Figure 6.14. The cell performance is best when the relative humidity is 100%, followed by 75% RH and then 50% RH. The difference between the polarization curves before and after the measurement is lowest when the RH is 75%.

The LSV result of single cell at 60 °C with 100%, 75% and 50% RH for cathode displays in Figure 6.15. The crossover current density at different relative humidity is nearly the same, as shown in Table 6.5. This result is a little different with Inaba group's [99] research, which states the higher RH, the higher crossover current density.

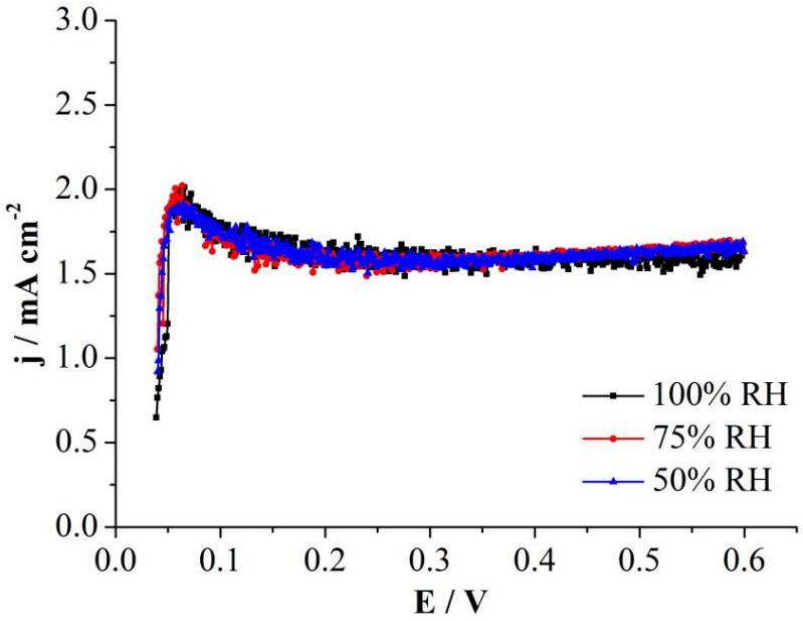

Figure 6.15. The LSV curves of single cell at 60 °C with 100%, 75% and 50% RH for the cathode.

Table 6.5. The crossover current density (j_c) at 60 °C with different RH for the cathode.

	100% RH	75% RH	50% RH
j_C / mA cm^{-2}	1.558±0.071	1.635±0.065	1.572±0.023

The EIS result of single cell at 60 °C with 100%, 75% and 50% RH under air and O_2 condition for the cathode side is shown in Figure 6.16 (a) and (b), apart. A typical half-circle EIS result of PEM fuel cell is obtained. The charge transfer resistance shows in Table 6.6. Obviously, the higher the humidity, the higher the R_{CT}, which is the same trend as presented in the literature [120]. Additionally, the R_{CT} is higher under O_2 conditions than that under air conditions, as shown in Table 6.6.

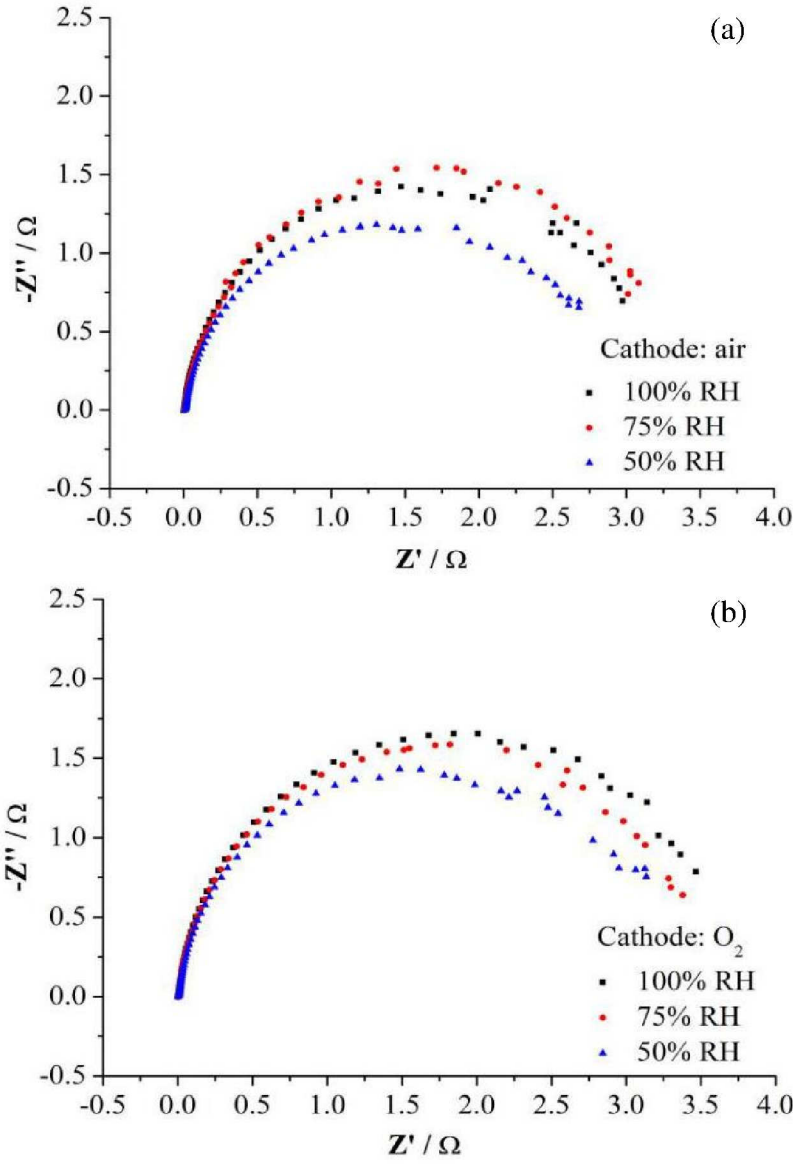

Figure 6.16. The EIS curves of single cell at 60 °C with 100%, 75% and 50%RH and feeding (a) air and (b) O_2 for the cathode at OCV conditions.

As above, the over voltage can be calculated by Equation 2.1, and the result is shown in Table 6.7. It was found that the over voltage is close at 100% and 75% RH, and higher than 50% RH, and the over potential is higher under O_2 conditions than that under air conditions.

Table 6.6. The charge resistance (R_{CT}) and calculated over voltage (η_C) of hydrogen reaction at different temperatures.

	Feeding O_2 in the cathode			Feeding air in the cathode		
	100% RH	75% RH	50% RH	100% RH	75% RH	50% RH
R_{CT} / Ω	3.688	3.443	2.961	2.942	2.875	2.604
η_C / V	0.144±0.007	0.141±0.006	0.116±0.002	0.115±0.005	0.118±0.005	0.102±0.001

The t-E curves of single cell at 60 °C with 100%, 75% and 50% RH under air and O_2 conditions for the cathode is shown in Figure 6.17 (a) and (b), separately. Clearly, all the curves show a characteristic that the OCV value increases fast at first (~20 s), and then decreases slowly up to a stable state. For both cases of O_2 or air, the OCV value increases with decreasing relative humidity, which is consistent with Sompalli groups research [141]. Moreover, the difference between maximum and minimum OCV value, at 900 s, is not more than 5 mV. Additionally, the OCV value in the case of O_2 is about 30 mV higher than for air.

Table 6.7. The OCV and OCP and relative calculated over voltage (η_C) caused by hydrogen crossover at different humidity.

	Feeding O_2 in the cathode			Feeding air in the cathode		
	100% RH	75% RH	50% RH	100% RH	75% RH	50% RH
$OCV_{single\ cell}$ / V	0.986	0.987	0.988	0.954	0.953	0.955
$OCP_{half\text{-}cell}$ / V	1.028±0.005	1.029±0.005	1.030±0.005	1.004±0.005	1.005±0.005	1.006±0.005
η_C / V	0.042±0.005	0.042±0.005	0.042±0.005	0.050±0.005	0.052±0.005	0.051±0.005

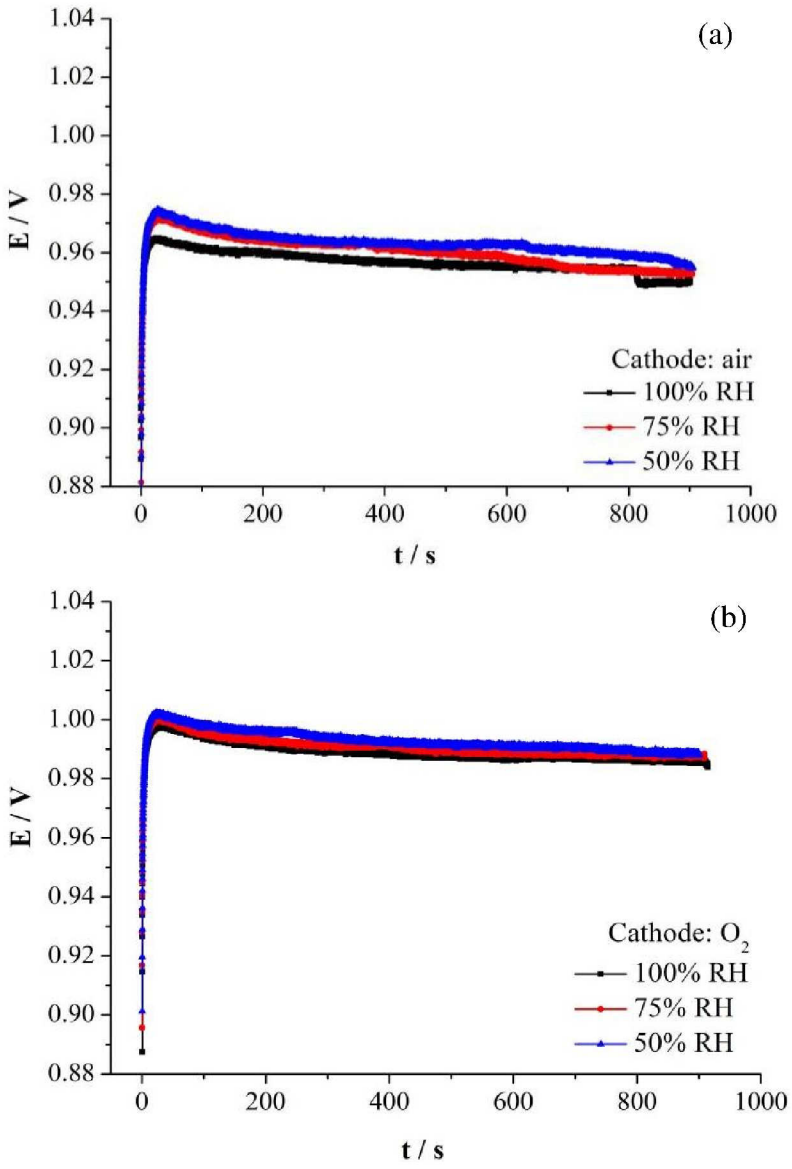

Figure 6.17. The t-E curves of single cell at 60 °C with 100%, 75% and 50% RH and feeding (a) air and (b) O_2 for the cathode.

Owing to the requirement of the experimental OCP of half-cell on different humidity, which is lacking, it was replaced by the calculated half-cell OCP on different humidity, using the method in chapter 2. The half-cell data comes from the OCP of pure Pt. The OCP value at 900 s is shown in Table 6.7. Then, the relationship of humidity and over voltage can be qualitatively analyzed.

Figure 6.18 shows the comparison of the calculated and experimental over voltage. It can be seen that the calculated over voltage is close at 100% and 75% RH, which is bigger than that at

50% RH. The value in the case of O_2 is bigger than for air. However, the experimental over voltage is the same at different RH in both cases of O_2 and air.

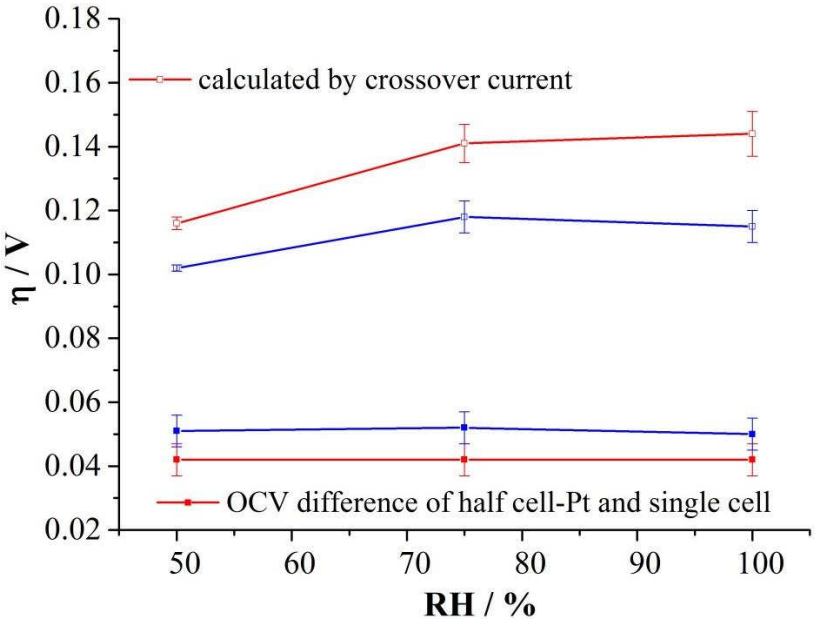

Figure 6.18. The comparison of calculated (empty symbol) and experimental (full symbol) t-η at 60 °C when the cathode is O_2 (red) and air (blue) at different humidity.

6.4 Summary

(1) PEM fuel cells show a different t-E shape from that of half-cells. Fast steps and slow steps are included, but the slope decreases in the slow steps, and the difference is caused by hydrogen crossover. The overvoltage caused by hydrogen crossover increases with increasing time.

(2) The over voltage caused by hydrogen crossover can be obtained by calculation from Equation 2.1 and by experiment from the difference between the OCP of half-cell and the OCV of single cell. The calculated over voltage is higher than the experimental one. An assumption is that for the hydrogen diffused from anode to cathode, only a part of them lose electrons, produce protons, and then offer the electrons and protons to react with O_2 to form water, or to react with the platinum oxide to form pure platinum. Additionally, another part of this hydrogen directly reacts with O_2 to form water.

(3) The OCV value with O_2 on the cathode, at 900 s, is about 30 mV bigger than that for air. They are about 0.986 V and 0.954 V at 60 °C when the cathode is O_2 and air, separately. Moreover, the minimum and maximum over potential from experiment, at 900 s, is 21 and 48 mV for O_2, separately, and 31 and 64 mV for air, separately, in which the OCV value of half-cell comes from the t-E of pure platinum and catalyst of $Pt/C_{20\%\ Pt}$. Namely, for the assumed reactions above, it creates different reaction efficiency at different O_2 concentration.

(4) The OCV value, at 900 s, at different temperatures is very close. The over voltage calculated from Equation 2.1 increases with increasing temperatures because of the increasing crossover current density. The over voltage from experiments decreases with increasing temperatures, which is explained by the possibility that the higher temperature is helpful for the reaction of H_2 directly reacting with O_2 to form water and the reaction of platinum oxide reduced to pure platinum.

(5) The OCV value, at 900 s, at different humidity is very close. The calculated over voltage is close at 100% and 75% RH, which is bigger than that at 50% RH. The experimental over voltage is the same at different RH in both cases of O_2 and air.

Chapter 7 Discussion

The OCV is the voltage under no current load. The research on OCV of fuel cells is significant since it has been an effective means of diagnosing fuel cells and has been applied for accelerated life-time tests for fuel cells. Theoretically, the OCV should be equal to the theoretical cell potential, which should be about 1.22 V (NTP) [7-9, 46] when temperature and gas pressure is considered, or about 1.01 V (NTP) [8, 46] when gas solubility is considered. However, the OCV of PEFC [29] is close to 1V when the H_2 is for the anode and air for the cathode, respectively. Mixed potential and hydrogen crossover are the most widely accepted explanations for why the experimental potential is lower than the theoretical value. Study on mixed potential always focuses on the oxidation of Pt/PtO surface, and study on hydrogen crossover is usually done through the crossover rate.

In the literature noted above, the mechanism of platinum surface oxidation is investigated as a function of potential. In the case of the OCV of PEFC, the potential results from the kinetics of the surface reaction. The kinetics of surface oxidation can be derived by observing the open circuit potential as a function of time. In this thesis, I study the OCV of PEFC independently by mixed potential and hydrogen crossover, which is accomplished by the study of OCP of half-cell and OCV of single cell.

In this thesis, the study on the OCP of the half-cell is achieved with two different equipments using the electrochemical measurement of cyclic voltammetry and LSV added chrono-potentiometry. The study on OCV of the single cell is accomplished with the Baltic quickCONNECTfixture using the electrochemical measurement of cycle voltammetry, linear sweeping voltammetry, EIS, and potential holding added chronopotentiometry.

7.1. The t-E curve

As shown before, the t-E curve of platinum disk, carbon support and platinum on carbon support in H_2SO_4 is of the same shape, which changes with time. Figure 7.1 gives their comparison. All the curves can be divided into 2 steps: a fast reaction step and a slow reaction step. For the catalyst of platinum disk, it refers to the process of Pt oxidation to PtOH and its

further oxidation to PtO, separately. For the catalyst of carbon support, it refers to the adsorption of carbon oxide species on the surface of carbon and its further oxidation to carbon monoxide or carbon oxide, separately. And for the catalyst of platinum on carbon support, it is a mixture of these two conditions, but platinum is dominant in its electrochemical property. Comparing their OCP value, Pt is the highest and carbon support is the lowest, and Pt on carbon support is between them, closer to Pt. The OCP of the Pt /$C_{20\%Pt}$ is the smallest. As well, the OCP of Pt /$C_{46\%Pt}$ and Pt /$C_{60\%Pt}$ is close.

However, for the single cell, it shows a difference in t-E shape from that of the half-cell. The half-cell includes fast steps and slow steps, but shows a slope decrease in the slow steps. As discussed in the introductory chapter, this difference is caused by hydrogen crossover. Obviously, the overvoltage caused by hydrogen crossover increases with increasing time.

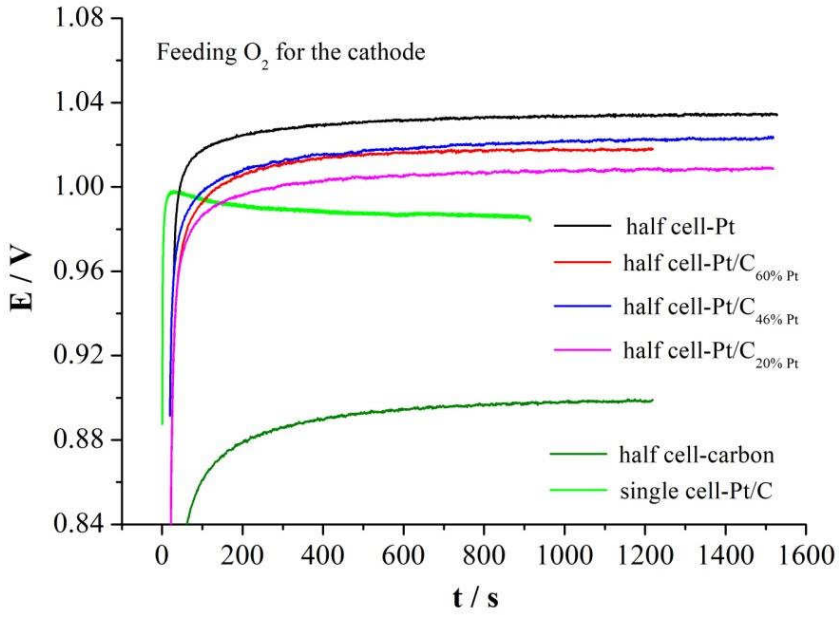

Figure 7.1. The comparison of t-E curves of half-cell at 60 °C with O_2 saturation and single cell at 60 °C with 100% RH for both sides and feeding O_2 for the cathode.

The over voltage caused by hydrogen crossover can also be calculated by Equation 2.1. The calculated over voltage is higher than the experimental one, the difference between the OCP of half-cell and the OCV of single cell. An assumption is that for the hydrogen diffused from anode to cathode, only a part of them loses electrons, produces protons, and then offers the electrons

and protons to react with O_2 to form water (case 1), or to react with the platinum oxide to form pure platinum (case 3). Also some hydrogen directly reacts with O_2 to form water (case 2). If only case 1 exists, the over voltage is just equal to the calculated value from Equation 2.1. However, the reality of the mix of case 1, case 2 and case 3 makes the over voltage from OCV difference is smaller than calculated one.

7.2. The effect of temperature

From the Nernst equation and the experiment, it is known that temperature affects the OCP of the half-cell significantly. Specifically, the OCV value decreases with increasing temperature. From 30 °C to 70 °C, the OCP value decreases about 26 mV, 22 mV and 28 mV for the catalyst of platinum solid disk, carbon layer and the catalyst layer of 20% platinum on carbon support, separately. For single cell, the OCV at different temperatures is very close. Figure 7.2 (a) shows a comparison of them.

Moreover, the calculated over voltage caused by hydrogen crossover increases with increasing temperature because of the increasing crossover current density. While, the experimental one decreases with increasing temperatures, which is explained by the possibility that the higher temperature is helpful for the reaction of H_2 directly reacting with O_2 to form water and the reaction of platinum oxide reduced to pure platinum.

Here, I give the over potential caused by the mixed potential ($\eta_{\text{mixed potential}}$) and hydrogen cross over ($\eta_{\text{cross over}}$), separately, in the temperature range of 30 °C - 80 °C, as shown in Figure 7.2 (b). In which, the OCP or OCV value used for calculation is the value at 900 s. The absolute value of $\eta_{\text{mixed potential}}$ is used because it is negative. The OCP value comes from the sample of the platinum disk and 20% platinum on carbon support with 20 μg_{Pt} cm^{-2} loading.

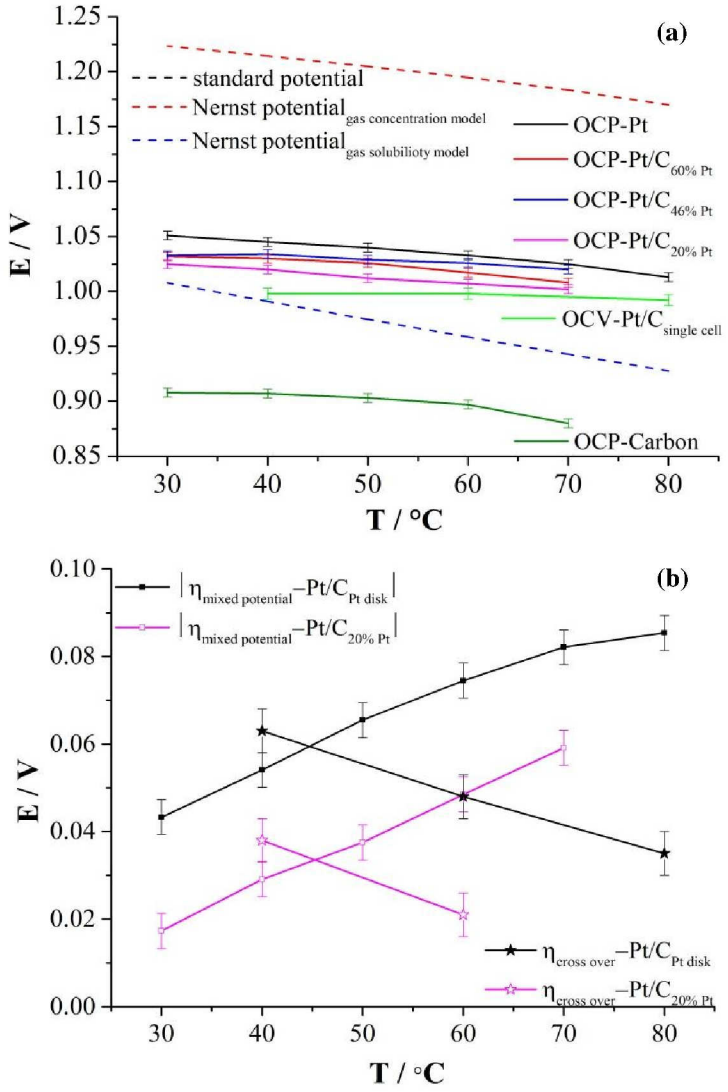

Figure 7.2. (a) a total comparison of calculated standard potential (dashed line, black), calculated Nernst potential by two different gas concentration consideration (dashed line, red and blue) and experimental OCV value of single cell (solid line, light green) and half-cell for the electrode of platinum solid disk (solid line, black), carbon layer (solid line, dark green) and catalyst layer of 20%, 46% and 60%Pt on carbon support (solid line, purple, blue and red) at different temperature, and (b) the over potential caused by the mixed potential (cube symbol) and hydrogen cross over (stars symbol) in the case of O_2 for the cathode at different temperature. The black and purple line in (b) represents the OCP of half-cell comes from platinum solid disk and catalyst layer of 20%Pt on carbon support, separately.

7.3. The effect of gas composition

As discussed above, the OCP value of platinum disk, carbon support and platinum on carbon support, at 900 s, in 1 M H_2SO_4 with O_2 saturation is higher than that with air saturation and higher than that with N_2 saturation. The Nernst equation and first order reaction have been used for calculation. The calculation results fit well with the experimental results. The mixed potential, E_{mix}, and the reaction rate constant, k, are a function of temperature. Each of their coverage in the case of O_2 is higher than for air. Figure 7.3 (a), (b) and (c) give a general comparison of them.

For single cell, the OCV value in the case of O_2 on the cathode, at 900 s, is about 30 mV bigger than for air. They are about 0.986 V and 0.954 V at 60 °C when the cathode is O_2 and air, separately. Moreover, the minimum and maximum over voltage from experiment, at 900 s, is 21 and 48 mV for O_2, separately, and 31 and 64 mV for air, separately, in which the OCP value of half-cell comes from the t-E of pure platinum and catalyst of $Pt/C_{20\%Pt}$. Namely, for the assumed reactions above, the reaction efficiency is different at different O_2 concentration. This has been shown in Figure 6.10.

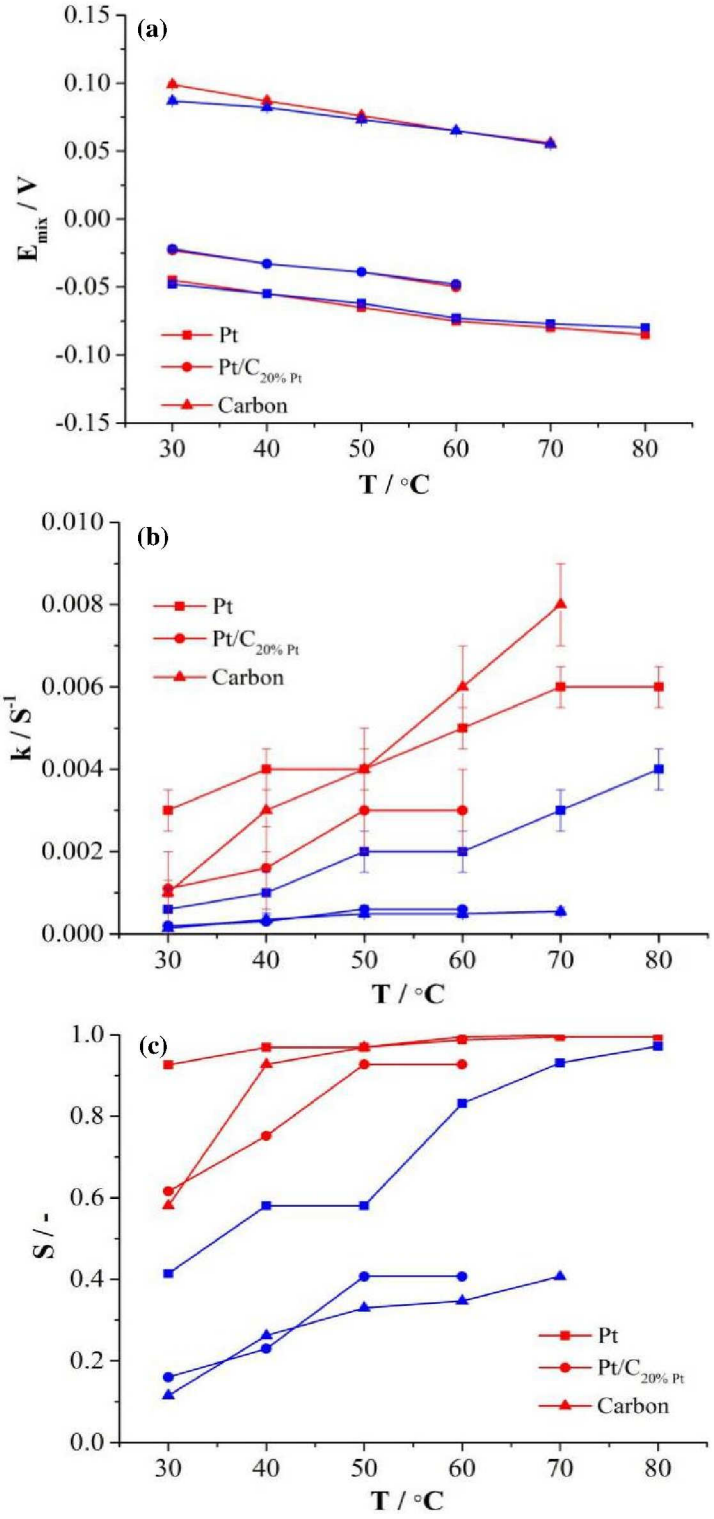

Figure 7.3. (a)The mixed potential (E_{mix}), (b) reaction rate constant rate (k), and (c) the surface coverage at 900 s(S) of the catalyst of platinum disk, carbon support and platinum on carbon support, with O_2 (red line) and air (blue line) saturation at different temperature.

7.4. The effect of electrolyte concentration on the OCP of half-cell

Another influencing factor which is worth mentioning is the electrolyte concentration. As shown in Figure 7.4, the OCP of Pt in H_2SO_4, at 900 s, decreases with increasing electrolyte concentration. From 0.001 to 6 M H_2SO_4, the OCP value at 30 °C decreases about 80 mV, and the OCP value in the temperature range of 30 - 80 °C decreases about 43 mV, 38 mV and 36 mV, separately. By calculation, it demonstrates that the mixed potential and the reaction rate constant depend on the concentration, which is not consistent with the model. A possible explanation is that the proton amount on both sides of the electrode of the cell is no longer the same following the surface oxidation of platinum electrode on the cathode side.

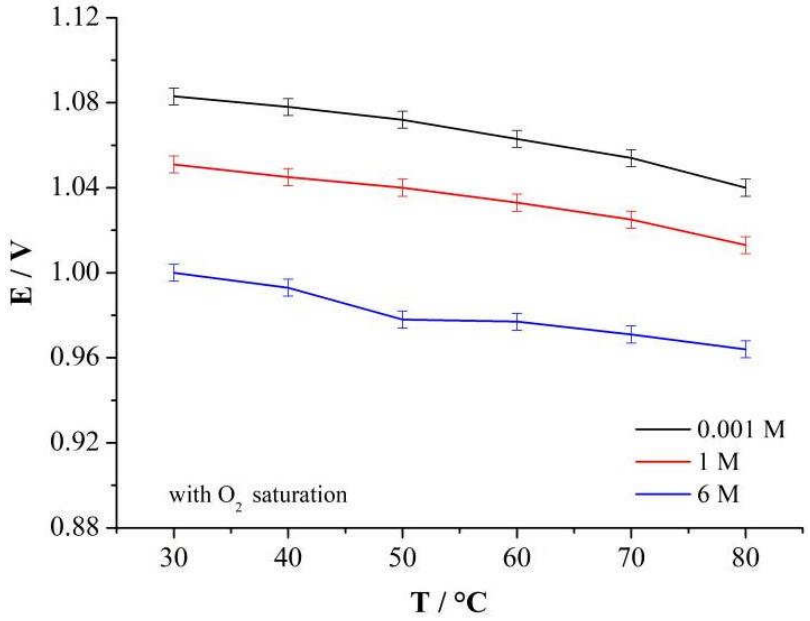

Figure 7.4. The OCP value of Pt, at 900 s, with O_2 saturation in H_2SO_4 at different concentration and temperature.

7.5. Other factors

As for some other factors, their effects are shown below:

(1) For platinum, its reaction rate depends on the electrolyte. In perchloric acid, it seems to be faster, but the sulfuric acid is chosen because the results can be compared to the literature.

(2) For platinum, 'glass cell-2' half-cell shows a lower OCP value than 'glass cell-1' half-cell.

(3) For the different thicknesses of carbon support, the thicker the carbon layer, the higher the OCP value (at 900 s). For platinum on carbon support, it only shows a slightly different OCP value.

(4) From Table 6.7 and Figure 6.18, it is known that the calculated OCP value of half-cell and the OCV value of single cell, at 900 s, is close at different humidity. The calculated over voltage is close at 100% and 75% RH, which is bigger than that at 50% RH. The experimental over voltage is the same at different RH in both cases of O_2 and air.

Chapter 8 Conclusion

In order to gain a good understanding of the OCV of PEFC, the OCP of the half-cell and the OCV of the single cell is studied in this thesis. It is found that the OCP of the half-cell is a mixed potential of oxygen reduction reaction, and platinum oxidation (or carbon oxidation or both of them) with a catalyst of platinum solid disk (or carbon layer or Pt with carbon layer). However, the OCV of the single cell is not only influenced by mixed potential, but also by hydrogen crossover.

The key findings of the half-cell experiment are presented in the following：

- The OCP of Pt (or carbon support or Pt on carbon support) in the half-cell in H_2SO_4 changes with time, which includes a fast reaction region and a slow reaction region. The OCP with O_2 saturation is higher than that for air. The OCP of platinum disk, carbon support and platinum on carbon support in 1 M H_2SO_4 at 30 °C is about 1.051, 0.908 and 1.024 V with the error of ±0.004 V, separately. All the curves can be divided into 2 steps: a fast reaction step and a slow reaction step. For the catalyst of platinum disk, it refers to the process of Pt oxidation to PtOH and its further oxidation to PtO, separately. For the catalyst of carbon support, it refers to the adsorption of carbon oxide species on the surface of carbon and its further oxidation to carbon monoxide or carbon oxide, separately. For a catalyst of platinum on carbon support, it is a mix of these two conditions, but platinum is dominant in its electrochemical property.
- The OCP in the half-cell in 1 M H_2SO_4, at 900 s, decreases with increasing temperature. From 30 °C to 70 °C, it drops about 26 mV, 22 mV and 28 mV for the platinum disk catalyst, carbon layer and platinum on carbon support, separately.
- Gas composition influences the OCP value in the half-cell. In order to facilitate an understanding of the principle reactions from an engineering perspective, the same model for calculation using the Nernst equation and first order reaction fits well with the experimental result. The higher the temperature is, the lower the mixed potential (E_{mix}) will be, and the higher reaction rate constant (k) will be. Additionally, the mixed potential is independent of gas concentration, while the reaction rate constant is higher for O_2 than for

air.

- The OCP of Pt in H_2SO_4, at 900 s, decreases with increasing acid concentration. From 0.001 to 6 M H_2SO_4, the OCP value at 30 °C decreases about 43 mV, 38 mV and 36 mV, separately. The mixed potential, E_{mix}, and the reaction rate constant, k, depends on the concentration.
- Other factors like acid type, the equipment of the cell and layer thickness and so on, influence the OCP of half-cell slightly.

The following are the key findings of the single cell experiment：

- The t-E curve of the single cell shows a different curve shape with that of the half-cell, including more fast steps and a decreased slow step. The difference is explained to be the result of hydrogen crossover. Compared to the calculation, the experimental over potential caused by hydrogen crossover is smaller.
- The OCV value for O_2 on the cathode, at 900 s, is about 30 mV bigger than that for air on the cathode side. They are about 0.986 V and 0.954 V at 60 °C when the cathode is O_2 and air, separately. Moreover, the minimum and maximum over potential from the experiment, at 900 s, is 21 and 48 mV for O_2, separately, and 31 and 64 mV for air, separately.
- The OCV at different temperature and humidity is close. As the temperature increases, the crossover current density increases, while the experimental over voltage decreases. The experimental over voltage at different humidity is very close.

Reference

1. Huang, X., Z. Zhang, and J. Jiang. Fuel cell technology for distributed generation: an overview. in Industrial Electronics, 2006 IEEE International Symposium on. 2006. IEEE.
2. Franco, A.A., Polymer electrolyte fuel cells: science, applications, and challenges. 2016: Pan Stanford.
3. Steele, B.C. and A. Heinzel, Materials for fuel-cell technologies, in Materials For Sustainable Energy: A Collection of Peer-Reviewed Research and Review Articles from Nature Publishing Group. 2011, World Scientific. p. 224-231.
4. Koh, J.K., Y. Jeon, Y.I. Cho, J.H. Kim, and Y.-G. Shul, A facile preparation method of surface patterned polymer electrolyte membranes for fuel cell applications. Journal of Materials Chemistry A, 2014. **2**(23): p. 8652-8659.
5. Daud, W., R. Rosli, E. Majlan, S. Hamid, R. Mohamed, and T. Husaini, PEM fuel cell system control: A review. Renewable Energy, 2017. **113**: p. 620-638.
6. Vilekar, S.A. and R. Datta, The effect of hydrogen crossover on open-circuit voltage in polymer electrolyte membrane fuel cells. Journal of Power Sources, 2010. **195**(8): p. 2241-2247.
7. Mench, M.M., E.C. Kumbur, and T.N. Veziroglu, Polymer electrolyte fuel cell degradation. 2011: Academic Press.
8. Reimer, U., W. Lehnert, Y. Holade, and B. Kokoh, Irreversible losses in fuel cells, in Fuel Cells and Hydrogen. 2018, Elsevier. p. 15-40.
9. Zhang, J., Z. Xie, J. Zhang, Y. Tang, C. Song, T. Navessin, Z. Shi, D. Song, H. Wang, and D.P. Wilkinson, High temperature PEM fuel cells. Journal of Power Sources, 2006. **160**(2): p. 872-891.
10. Huaman, R.N.E. and T.X. Jun, Energy related CO_2 emissions and the progress on CCS projects: a review. Renewable and Sustainable Energy Reviews, 2014. **31**: p. 368-385.
11. Nejat, P., F. Jomehzadeh, M.M. Taheri, M. Gohari, and M.Z.A. Majid, A global review of energy consumption, CO_2 emissions and policy in the residential sector (with an

overview of the top ten CO_2 emitting countries). Renewable and Sustainable Energy Reviews, 2015. **43**: p. 843-862.

12. Seto, K.C., B. Güneralp, and L.R. Hutyra, Global forecasts of urban expansion to 2030 and direct impacts on biodiversity and carbon pools. Proceedings of the National Academy of Sciences, 2012. **109**(40): p. 16083-16088.
13. d'Amour, C.B., F. Reitsma, G. Baiocchi, S. Barthel, B. Güneralp, K.-H. Erb, H. Haberl, F. Creutzig, and K.C. Seto, Future urban land expansion and implications for global croplands. Proceedings of the National Academy of Sciences, 2017. **114**(34): p. 8939-8944.
14. Merkel, T.C., H. Lin, X. Wei, and R. Baker, Power plant post-combustion carbon dioxide capture: An opportunity for membranes. Journal of Membrane Science, 2010. **359**(1-2): p. 126-139.
15. Pablo-Romero, M.d.P., R. Pozo-Barajas, and R. Yñiguez, Global changes in residential energy consumption. Energy Policy, 2017. **101**: p. 342-352.
16. Castanheira, L.F.R., Corrosion of high surface area carbon supports used in proton-exchange membrane fuel cell electrodes. 2014, Université de Grenoble.
17. Bagotsky, V.S., Fuel cells: problems and solutions. Vol. 56. 2012: John Wiley & Sons.
18. Calise, F., Design of a hybrid polygeneration system with solar collectors and a solid oxide fuel cell: dynamic simulation and economic assessment. International Journal of Hydrogen Energy, 2011. **36**(10): p. 6128-6150.
19. Gencoglu, M.T. and Z. Ural, Design of a PEM fuel cell system for residential application. International Journal of Hydrogen Energy, 2009. **34**(12): p. 5242-5248.
20. Hamada, Y., K. Takeda, R. Goto, and H. Kubota, Hybrid utilization of renewable energy and fuel cells for residential energy systems. Energy and Buildings, 2011. **43**(12): p. 3680-3684.
21. Wee, J.-H., Contribution of fuel cell systems to CO_2 emission reduction in their application fields. Renewable and Sustainable Energy Reviews, 2010. **14**(2): p. 735-744.
22. Hajimolana, S.A., M.A. Hussain, W.A.W. Daud, M. Soroush, and A. Shamiri, Mathematical modeling of solid oxide fuel cells: A review. Renewable and Sustainable Energy Reviews, 2011. **15**(4): p. 1893-1917.

23. Wee, J.-H., J.H. Roh, and J. Kim, A comparison of solar photovoltaics and molten carbonate fuel cells as commercial power plants. Renewable and Sustainable Energy Reviews, 2011. **15**(1): p. 697-704.
24. Mekhilef, S., R. Saidur, and A. Safari, Comparative study of different fuel cell technologies. Renewable and Sustainable Energy Reviews, 2012. **16**(1): p. 981-989.
25. Hwang, J.-J., Sustainability study of hydrogen pathways for fuel cell vehicle applications. Renewable and Sustainable Energy Reviews, 2013. **19**: p. 220-229.
26. Kim, T., S. Lee, and H. Park, The potential of PEM fuel cell for a new drinking water source. Renewable and Sustainable Energy Reviews, 2011. **15**(8): p. 3676-3689.
27. Andújar, J.M. and F. Segura, Fuel cells: History and updating. A walk along two centuries. Renewable and sustainable energy reviews, 2009. **13**(9): p. 2309-2322.
28. Lucia, U., Overview on fuel cells. Renewable and Sustainable Energy Reviews, 2014. **30**: p. 164-169.
29. Laraminie, J. and A. Dicks, Fuel Cell Systems Explained. 2003, West Sussex, England. John Wiley & Sons, Inc.
30. Vielstich, W., H.A. Gasteiger, and H. Yokokawa, Handbook of fuel cells: fundamentals technology and applications: advances in electrocatalysis, materials, diagnostics and durability. Vol. 5. 2009: John Wiley & Sons.
31. Barbir, F., PEM fuel cells: theory and practice. 2012: Academic Press.
32. Antolini, E., Carbon supports for low-temperature fuel cell catalysts. Applied Catalysis B: Environmental, 2009. **88**(1-2): p. 1-24.
33. Ambrosio, E., M. Dumitrescu, C. Francia, C. Gerbaldi, and P. Spinelli, Ordered mesoporous carbons as catalyst support for PEM fuel cells. Fuel Cells, 2009. **9**(3): p. 197-200.
34. Bezerra, C.W., L. Zhang, K. Lee, H. Liu, A.L. Marques, E.P. Marques, H. Wang, and J. Zhang, A review of Fe–N/C and Co–N/C catalysts for the oxygen reduction reaction. Electrochimica Acta, 2008. **53**(15): p. 4937-4951.
35. Zhang, S., X.-Z. Yuan, J.N.C. Hin, H. Wang, K.A. Friedrich, and M. Schulze, A review of platinum-based catalyst layer degradation in proton exchange membrane fuel cells. Journal of Power Sources, 2009. **194**(2): p. 588-600.

36. Schmittinger, W. and A. Vahidi, A review of the main parameters influencing long-term performance and durability of PEM fuel cells. Journal of Power Sources, 2008. **180**(1): p. 1-14.

37. Franco, A.A. and M. Gerard, Multiscale model of carbon corrosion in a PEFC: coupling with electrocatalysis and impact on performance degradation. Journal of The Electrochemical Society, 2008. **155**(4): p. B367-B384.

38. Wu, J., X.Z. Yuan, J.J. Martin, H. Wang, J. Zhang, J. Shen, S. Wu, and W. Merida, A review of PEM fuel cell durability: Degradation mechanisms and mitigation strategies. Journal of Power Sources, 2008. **184**(1): p. 104-119.

39. Weber, A.Z., Gas-crossover and membrane-pinhole effects in polymer-electrolyte fuel cells. Journal of the Electrochemical Society, 2008. **155**(6): p. B521-B531.

40. Sugawara, S., T. Maruyama, Y. Nagahara, S.S. Kocha, K. Shinohra, K. Tsujita, S. Mitsushima, and K.-i. Ota, Performance decay of proton-exchange membrane fuel cells under open circuit conditions induced by membrane decomposition. Journal of Power Sources, 2009. **187**(2): p. 324-331.

41. Chen, H., P. Pei, and M. Song, Lifetime prediction and the economic lifetime of proton exchange membrane fuel cells. Applied Energy, 2015. **142**: p. 154-163.

42. Pei, P., Q. Chang, and T. Tang, A quick evaluating method for automotive fuel cell lifetime. International Journal of Hydrogen Energy, 2008. **33**(14): p. 3829-3836.

43. Tian, G., S. Wasterlain, I. Endichi, D. Candusso, F. Harel, X. François, M.-C. Péra, D. Hissel, and J.-M. Kauffmann, Diagnosis methods dedicated to the localisation of failed cells within PEMFC stacks. Journal of Power Sources, 2008. **182**(2): p. 449-461.

44. Tian, G., S. Wasterlain, D. Candusso, F. Harel, D. Hissel, and X. François, Identification of failed cells inside PEMFC stacks in two cases: Anode/cathode crossover and anode/cooling compartment leak. international journal of hydrogen energy, 2010. **35**(7): p. 2772-2776.

45. Khorasani, M.A., S. Asghari, A. Mokmeli, M. Shahsamandi, and B.F. Imani, A diagnosis method for identification of the defected cell (s) in the PEM fuel cells. International Journal of Hydrogen Energy, 2010. **35**(17): p. 9269-9275.

46. Reimer, U., Y. Cai, R. Li, D. Froning, and W. Lehnert, Time Dependence of the Open Circuit Potential of Platinum Disk Electrodes in Half Cell Experiments. Journal of The Electrochemical Society, 2019. **166**(7): p. F3098-F3104.
47. Brockris, J.M. and S. Srinivasan, Fuel cells: their electrochemistry. 1969.
48. Wroblowa, H., M. Rao, A. Damjanovic, and B. JO'M, Adsorption and kinetics at platinum electrodes in the presence of oxygen at zero net current. Journal of Electroanalytical Chemistry and Interfacial Electrochemistry, 1967. **15**: p. 139-150.
49. Appleby, A., Oxygen Reduction on Oxide-Free Platinum in 85% Orthophosphoric Acid: Temperature and Impurity Dependence. Journal of the Electrochemical Society, 1970. **117**(3): p. 328-335.
50. Hoare, J.P., Rest Potentials in the Platinum-Oxygen-Acid System. Journal of the Electrochemical Society, 1962. **109**(3): p. C83-C83.
51. Gilroy, D. and B. Conway, Surface oxidation and reduction of platinum electrodes: coverage, kinetic and hysteresis studies. Canadian Journal of Chemistry, 1968. **46**(6): p. 875-890.
52. Jerkiewicz, G., G. Vatankhah, J. Lessard, M.P. Soriaga, and Y.-S. Park, Surface-oxide growth at platinum electrodes in aqueous $H2SO_4$: Reexamination of its mechanism through combined cyclic-voltammetry, electrochemical quartz-crystal nanobalance, and Auger electron spectroscopy measurements. Electrochimica Acta, 2004. **49**(9-10): p. 1451-1459.
53. Biegler, T. and R. Woods, Limiting oxygen coverage on smooth platinum anodes in acid solution. Journal of Electroanalytical Chemistry and Interfacial Electrochemistry, 1969. **20**(1): p. 73-78.
54. Rand, D. and R. Woods, A study of the dissolution of platinum, palladium, rhodium and gold electrodes in 1 M sulphuric acid by cyclic voltammetry. Journal of Electroanalytical Chemistry and Interfacial Electrochemistry, 1972. **35**(1): p. 209-218.
55. Makrides, A., N. Komodromos, and N. Hackerman, Dissolution of Metals in Aqueous Acid Solutions I. Current-potential Relations for Iron and Mild Steel 1. Journal of The Electrochemical Society, 1955. **102**(7): p. 363-369.
56. Angerstein-Kozlowska, H., B. Conway, and W. Sharp, The real condition of electrochemically oxidized platinum surfaces: Part I. Resolution of component processes.

Journal of Electroanalytical Chemistry and Interfacial Electrochemistry, 1973. **43**(1): p. 9-36.

57. Tilak, B., B. Conway, and H. Angerstein-Kozlowska, The real condition of oxidized pt electrodes: Part III. Kinetic theory of formation and reduction of surface oxides. Journal of Electroanalytical Chemistry and Interfacial Electrochemistry, 1973. **48**(1): p. 1-23.
58. Nagy, Z. and H. You, Applications of surface X-ray scattering to electrochemistry problems. Electrochimica Acta, 2002. **47**(19): p. 3037-3055.
59. Drnec, J., M. Ruge, F. Reikowski, B. Rahn, F. Carlà, R. Felici, J. Stettner, O.M. Magnussen, and D.A. Harrington, Initial stages of Pt (111) electrooxidation: dynamic and structural studies by surface X-ray diffraction. Electrochimica Acta, 2017. **224**: p. 220-227.
60. Anastasijević, N., V. Vesović, and R. Adžić, Determination of the kinetic parameters of the oxygen reduction reaction using the rotating ring-disk electrode: Part I. Theory. Journal of electroanalytical chemistry and interfacial electrochemistry, 1987. **229**(1-2): p. 305-316.
61. Marković, N. and P. Ross Jr, Surface science studies of model fuel cell electrocatalysts. Surface Science Reports, 2002. **45**(4-6): p. 117-229.
62. Zhdanov, V.P. and B. Kasemo, Kinetics of electrochemical O2 reduction on Pt. Electrochemistry Communications, 2006. **8**(7): p. 1132-1136.
63. Nørskov, J.K., J. Rossmeisl, A. Logadottir, L. Lindqvist, J.R. Kitchin, T. Bligaard, and H. Jonsson, Origin of the overpotential for oxygen reduction at a fuel-cell cathode. The Journal of Physical Chemistry B, 2004. **108**(46): p. 17886-17892.
64. Shi, Z., J. Zhang, Z.-S. Liu, H. Wang, and D.P. Wilkinson, Current status of ab initio quantum chemistry study for oxygen electroreduction on fuel cell catalysts. Electrochimica Acta, 2006. **51**(10): p. 1905-1916.
65. Song, Y., J.M. Fenton, H.R. Kunz, L.J. Bonville, and M.V. Williams, High-performance PEMFCs at elevated temperatures using Nafion 112 membranes. Journal of The Electrochemical Society, 2005. **152**(3): p. A539-A544.
66. Ramaswamy, N. and S. Mukerjee, Fundamental mechanistic understanding of electrocatalysis of oxygen reduction on Pt and non-Pt surfaces: acid versus alkaline media. Advances in Physical Chemistry, 2012. **2012**.

67. Srejić, I., M. Smiljanić, Z. Rakočević, and S. Štrbac, Oxygen reduction on polycrystalline Pt and Au electrodes in perchloric acid solution in the presence of acetonitrile. Int. J. Electrochem. Sci, 2011. **6**: p. 3344-3354.

68. Hoare, J.P., R. Thacker, and C.R. Wiese, Sorption of oxygen from solution by noble metals: II. Nitric acid-passivated bright platinum. Journal of Electroanalytical Chemistry and Interfacial Electrochemistry, 1971. **30**(1): p. 15-23.

69. Zhang, J., PEM fuel cell electrocatalysts and catalyst layers: fundamentals and applications. 2008: Springer Science & Business Media.

70. Thacker, R. and J.P. Hoare, Sorption of oxygen from solution by noble metals: I. Bright platinum. Journal of Electroanalytical Chemistry and Interfacial Electrochemistry, 1971. **30**(1): p. 1-14.

71. Parthasarathy, A., S. Srinivasan, A.J. Appleby, and C.R. Martin, Temperature dependence of the electrode kinetics of oxygen reduction at the platinum/Nafion® interface—a microelectrode investigation. Journal of the Electrochemical Society, 1992. **139**(9): p. 2530-2537.

72. Parthasarathy, A., C.R. Martin, and S. Srinivasan, Investigations of the O_2 Reduction Reaction at the Platinum/Nafion® Interface Using a Solid-State Electrochemical Cell. Journal of the Electrochemical Society, 1991. **138**(4): p. 916-921.

73. Parthasarathy, A., B. Dave, S. Srinivasan, A.J. Appleby, and C.R. Martin, The platinum microelectrode/Nafion interface: an electrochemical impedance spectroscopic analysis of oxygen reduction kinetics and Nafion characteristics. Journal of The Electrochemical Society, 1992. **139**(6): p. 1634-1641.

74. Kangasniemi, K.H., D. Condit, and T. Jarvi, Characterization of vulcan electrochemically oxidized under simulated PEM fuel cell conditions. Journal of The Electrochemical Society, 2004. **151**(4): p. E125-E132.

75. Borup, R., J. Meyers, B. Pivovar, Y.S. Kim, R. Mukundan, N. Garland, D. Myers, M. Wilson, F. Garzon, and D. Wood, Scientific aspects of polymer electrolyte fuel cell durability and degradation. Chemical Reviews, 2007. **107**(10): p. 3904-3951.

76. Shen, Q., M. Hou, D. Liang, Z. Zhou, X. Li, Z. Shao, and B. Yi, Study on the processes of start-up and shutdown in proton exchange membrane fuel cells. Journal of Power Sources, 2009. **189**(2): p. 1114-1119.

77. Kim, J., J. Lee, and Y. Tak, Relationship between carbon corrosion and positive electrode potential in a proton-exchange membrane fuel cell during start/stop operation. Journal of Power Sources, 2009. **192**(2): p. 674-678.

78. Tang, H., Z. Qi, M. Ramani, and J.F. Elter, PEM fuel cell cathode carbon corrosion due to the formation of air/fuel boundary at the anode. Journal of Power Sources, 2006. **158**(2): p. 1306-1312.

79. Paul, T.Y., W. Gu, J. Zhang, R. Makharia, F.T. Wagner, and H.A. Gasteiger, Carbon-support requirements for highly durable fuel cell operation, in Polymer electrolyte fuel cell durability. 2009, Springer. p. 29-53.

80. Perry, M.L., R.M. Darling, S. Kandoi, T.W. Patterson, and C. Reiser, Operating requirements for durable polymer-electrolyte fuel cell stacks, in Polymer Electrolyte Fuel Cell Durability. 2009, Springer. p. 399-417.

81. Reiser, C.A., L. Bregoli, T.W. Patterson, S.Y. Jung, J.D. Yang, M.L. Perry, and T.D. Jarvi, A reverse-current decay mechanism for fuel cells. Electrochemical and Solid-State Letters, 2005. **8**(6): p. A273-A276.

82. Shao, Y., G. Yin, Y. Gao, and P. Shi, Durability study of Pt/C and Pt/CNTs catalysts under simulated PEM fuel cell conditions. Journal of the Electrochemical Society, 2006. **153**(6): p. A1093-A1097.

83. Shao, Y., G. Yin, J. Zhang, and Y. Gao, Comparative investigation of the resistance to electrochemical oxidation of carbon black and carbon nanotubes in aqueous sulfuric acid solution. Electrochimica Acta, 2006. **51**(26): p. 5853-5857.

84. Coloma, F., A. Sepulvedaescribano, and F. Rodriguezreinoso, Heat-treated carbon-blacks as supports for platinum catalysts. Journal of Catalysis, 1995. **154**(2): p. 299-305.

85. Maass, S., F. Finsterwalder, G. Frank, R. Hartmann, and C. Merten, Carbon support oxidation in PEM fuel cell cathodes. Journal of Power Sources, 2008. **176**(2): p. 444-451.

86. Avasarala, B., R. Moore, and P. Haldar, Surface oxidation of carbon supports due to potential cycling under PEM fuel cell conditions. Electrochimica Acta, 2010. **55**(16): p. 4765-4771.

87. Knights, S.D., K.M. Colbow, J. St-Pierre, and D.P. Wilkinson, Aging mechanisms and lifetime of PEFC and DMFC. Journal of Power Sources, 2004. **127**(1-2): p. 127-134.

88. Siroma, Z., N. Fujiwara, T. Ioroi, S. Yamazaki, K. Yasuda, and Y. Miyazaki, Dissolution of Nafion® membrane and recast Nafion® film in mixtures of methanol and water. Journal of Power Sources, 2004. **126**(1-2): p. 41-45.

89. Fowler, M., J.C. Amphlett, R.F. Mann, B.A. Peppley, and P.R. Roberge, Issues associated with voltage degradation in a PEMFC. Journal of New Materials for Electrochemical Systems, 2002. **5**(4): p. 255-262.

90. Cai, M., M.S. Ruthkosky, B. Merzougui, S. Swathirajan, M.P. Balogh, and S.H. Oh, Investigation of thermal and electrochemical degradation of fuel cell catalysts. Journal of Power Sources, 2006. **160**(2): p. 977-986.

91. Reimer, U., B. Schumacher, and W. Lehnert, Accelerated degradation of high-temperature polymer electrolyte fuel cells: discussion and empirical modeling. Journal of The Electrochemical Society, 2015. **162**(1): p. F153-F164.

92. Kinoshita, K., Carbon: electrochemical and physicochemical properties. 1988.

93. Passalacqua, E., P. Antonucci, M. Vivaldi, A. Patti, V. Antonucci, N. Giordano, and K. Kinoshita, The influence of Pt on the electrooxidation behaviour of carbon in phosphoric acid. Electrochimica Acta, 1992. **37**(15): p. 2725-2730.

94. Yi, Y., G. Weinberg, M. Prenzel, M. Greiner, S. Heumann, S. Becker, and R. Schlögl, Electrochemical corrosion of a glassy carbon electrode. Catalysis Today, 2017. **295**: p. 32-40.

95. Gallagher, K.G. and T.F. Fuller, Kinetic model of the electrochemical oxidation of graphitic carbon in acidic environments. Physical Chemistry Chemical Physics, 2009. **11**(48): p. 11557-11567.

96. Yi, Y., J. Tornow, E. Willinger, M.G. Willinger, C. Ranjan, and R. Schlögl, Electrochemical degradation of multiwall carbon nanotubes at high anodic potential for oxygen evolution in acidic media. ChemElectroChem, 2015. **2**(12): p. 1929-1937.

97. Kocha, S.S., J. Deliang Yang, and J.S. Yi, Characterization of gas crossover and its implications in PEM fuel cells. AIChE Journal, 2006. **52**(5): p. 1916-1925.

98. Cheng, X., J. Zhang, Y. Tang, C. Song, J. Shen, D. Song, and J. Zhang, Hydrogen crossover in high-temperature PEM fuel cells. Journal of Power Sources, 2007. **167**(1): p. 25-31.

99. Inaba, M., T. Kinumoto, M. Kiriake, R. Umebayashi, A. Tasaka, and Z. Ogumi, Gas crossover and membrane degradation in polymer electrolyte fuel cells. Electrochimica Acta, 2006. **51**(26): p. 5746-5753.

100. Teranishi, K., K. Kawata, S. Tsushima, and S. Hirai, Degradation mechanism of PEMFC under open circuit operation. Electrochemical and Solid-State Letters, 2006. **9**(10): p. A475-A477.

101. Kim, J., J. Je, M. Kaviany, S.Y. Son, and M. Kim, Fuel crossover and internal current in polymer electrolyte membrane fuel cell from water visualization using X-ray radiography. Journal of Power Sources, 2011. **196**(20): p. 8398-8401.

102. Zhang, J., Y. Tang, C. Song, J. Zhang, and H. Wang, PEM fuel cell open circuit voltage (OCV) in the temperature range of 23 °C to 120 °C. Journal of Power Sources, 2006. **163**(1): p. 532-537.

103. Collier, A., H. Wang, X.Z. Yuan, J. Zhang, and D.P. Wilkinson, Degradation of polymer electrolyte membranes. International Journal of Hydrogen Energy, 2006. **31**(13): p. 1838-1854.

104. Yeager, H. and A. Steck, Cation and water diffusion in Nafion ion exchange membranes: influence of polymer structure. Journal of the Electrochemical Society, 1981. **128**(9): p. 1880-1884.

105. Yu, J., T. Matsuura, Y. Yoshikawa, M.N. Islam, and M. Hori, In situ analysis of performance degradation of a PEMFC under nonsaturated humidification. Electrochemical and Solid-State Letters, 2005. **8**(3): p. A156-A158.

106. Wu, J., X.Z. Yuan, H. Wang, M. Blanco, J.J. Martin, and J. Zhang, Diagnostic tools in PEM fuel cell research: Part I Electrochemical techniques. International Journal of Hydrogen Energy, 2008. **33**(6): p. 1735-1746.

107. Sakai, T., H. Takenaka, and E. Torikai, Gas diffusion in the dried and hydrated Nafions. Journal of the Electrochemical Society, 1986. **133**(1): p. 88-92.

108. Ogumi, Z., Z. Takehara, and S. Yoshizawa, Gas Permeation in SPE Method I. oxygen permeation through Nafion and Neosepta. Journal of the Electrochemical Society, 1984. **131**(4): p. 769-773.

109. Ogumi, Z., T. Kuroe, and Z.i. Takehara, Gas permeation in SPE method II. Oxygen and hydrogen permeation through Nafion. Journal of the Electrochemical Society, 1985. **132**(11): p. 2601-2605.

110. Jiang, R., H.R. Kunz, and J.M. Fenton, Investigation of membrane property and fuel cell behavior with sulfonated poly (ether ether ketone) electrolyte: Temperature and relative humidity effects. Journal of Power Sources, 2005. **150**: p. 120-128.

111. Yoshida, N., T. Ishisaki, A. Watakabe, and M. Yoshitake, Characterization of Flemion® membranes for PEFC. Electrochimica Acta, 1998. **43**(24): p. 3749-3754.

112. Weissbecker, V., U. Reimer, K. Wippermann, and W. Lehnert, A Comprehensive Corrosion Study on Metallic Materials for HT-PEFC Application. Ecs Transactions, 2013. **58**(1): p. 693-704.

113. Garsany, Y., O.A. Baturina, K.E. Swider-Lyons, and S.S. Kocha, Experimental Methods for Quantifying the Activity of Platinum Electrocatalysts for the Oxygen Reduction Reaction. Analytical Chemistry, 2010. **82**(15): p. 6321-6328.

114. Chakraborty, U., Fuel crossover and internal current in proton exchange membrane fuel cell modeling. Applied Energy, 2016. **163**(C): p. 60-62.

115. Yuan, X., H. Wang, J.C. Sun, and J. Zhang, AC impedance technique in PEM fuel cell diagnosis—A review. International Journal of Hydrogen Energy, 2007. **32**(17): p. 4365-4380.

116. Andreaus, B., A. McEvoy, and G. Scherer, Analysis of performance losses in polymer electrolyte fuel cells at high current densities by impedance spectroscopy. Electrochimica acta, 2002. **47**(13-14): p. 2223-2229.

117. Wagner, N., Characterization of membrane electrode assemblies in polymer electrolyte fuel cells using ac impedance spectroscopy. Journal of Applied Electrochemistry, 2002. **32**(8): p. 859-863.

118. Hou, J., W. Song, H. Yu, Y. Fu, Z. Shao, and B. Yi, Electrochemical impedance investigation of proton exchange membrane fuel cells experienced subzero temperature. Journal of Power Sources, 2007. **171**(2): p. 610-616.

119. Jia, S., Lateral Current Density Distribution in a PEM Fuel Cell. 2013.

120. Cimenti, M., D. Bessarabov, M. Tam, and J. Stumper, Investigation of proton transport in the catalyst layer of PEM fuel cells by electrochemical impedance spectroscopy. ECS transactions, 2010. **28**(23): p. 147-157.

121. Hou, J., B. Yi, H. Yu, L. Hao, W. Song, Y. Fu, and Z. Shao, Investigation of resided water effects on PEM fuel cell after cold start. International Journal of Hydrogen Energy, 2007. **32**(17): p. 4503-4509.

122. Kang, J. and J. Kim, Membrane electrode assembly degradation by dry/wet gas on a PEM fuel cell. International Journal of Hydrogen Energy, 2010. **35**(23): p. 13125-13130.

123. Pei, P., Z. Wu, Y. Li, X. Jia, D. Chen, and S. Huang, Improved methods to measure hydrogen crossover current in proton exchange membrane fuel cell. Applied Energy, 2018. **215**: p. 338-347.

124. Sekar, N. and R.P. Ramasamy, Electrochemical impedance spectroscopy for microbial fuel cell characterization. J Microb Biochem Technol S, 2013. **6**(2).

125. Dhiman, R., E. Johnson, E.M. Skou, P. Morgen, and S.M. Andersen, SiC nanocrystals as Pt catalyst supports for fuel cell applications. Journal of Materials Chemistry A, 2013. **1**(19): p. 6030-6036.

126. Linstrom, P., NIST Standard Reference Database Number 69. NIST Chemistry WebBook, 2003.

127. Kerr, J. and D. Lide, CRC handbook of chemistry and physics 1999–2000: a ready-reference book of chemical and physical data. CRC Handbook of Chemistry and Physics, 2000.

128. Weissbecker, V., K. Wippermann, and W. Lehnert, Electrochemical Corrosion Study of Metallic Materials in Phosphoric Acid as Bipolar Plates for HT-PEFCs. Journal of the Electrochemical Society, 2014. **161**(14): p. F1437-F1447.

129. Ralph, T., G. Hards, J. Keating, S. Campbell, D. Wilkinson, M. Davis, J. St-Pierre, and M. Johnson, Low cost electrodes for proton exchange membrane fuel cells performance in single cells and Ballard stacks. Journal of the Electrochemical Society, 1997. **144**(11): p. 3845-3857.

130. Hasché, F., M. Oezaslan, and P. Strasser, Activity, stability and degradation of multi walled carbon nanotube (MWCNT) supported Pt fuel cell electrocatalysts. Physical Chemistry Chemical Physics, 2010. **12**(46): p. 15251-15258.

131. Zhang, Y., X. Zhang, X. Ma, W. Guo, C. Wang, T. Asefa, and X. He, A facile synthesis of nitrogen-doped highly porous carbon nanoplatelets: efficient catalysts for oxygen electroreduction. Scientific Reports, 2017. **7**: p. 43366.

132. Shui, J., M. Wang, F. Du, and L. Dai, N-doped carbon nanomaterials are durable catalysts for oxygen reduction reaction in acidic fuel cells. Science Advances, 2015. **1**(1): p. e1400129.

133. Guo, C., Y. Wu, Z. Li, W. Liao, L. Sun, C. Wang, B. Wen, Y. Li, and C. Chen, The oxygen reduction electrocatalytic activity of cobalt and nitrogen co-doped carbon nanocatalyst synthesized by a flat template. Nanoscale Research Letters, 2017. **12**(1): p. 144.

134. Watanabe, M., H. Igarashi, and K. Yosioka, An Experimental Prediction of the Preparation Condition of Nafion-Coated Catalyst Layers for Pefcs. Electrochimica Acta, 1995. **40**(3): p. 329-334.

135. Higuchi, E., H. Uchida, and M. Watanabe, Effect of loading level in platinum-dispersed carbon black electrocatalysts on oxygen reduction activity evaluated by rotating disk electrode. Journal of Electroanalytical Chemistry, 2005. **583**(1): p. 69-76.

136. Schmidt, T.J., H.A. Gasteiger, and R.J. Behm, Rotating disk electrode measurements on the CO tolerance of a high-surface area Pt/Vulcan carbon fuel cell catalyst. Journal of the Electrochemical Society, 1999. **146**(4): p. 1296-1304.

137. Taylor, S., E. Fabbri, P. Levecque, T.J. Schmidt, and O. Conrad, The effect of platinum loading and surface morphology on oxygen reduction activity. Electrocatalysis, 2016. **7**(4): p. 287-296.

138. Thampan, T., S. Malhotra, J. Zhang, and R. Datta, PEM fuel cell as a membrane reactor. Catalysis Today, 2001. **67**(1-3): p. 15-32.

139. Spinelli, P., C. Francia, E. Ambrosio, and M. Lucariello, Semi-empirical evaluation of PEMFC electro-catalytic activity. Journal of Power Sources, 2008. **178**(2): p. 517-524.

140. Francia, C., V.S. Ijeri, S. Specchia, and P. Spinelli, Estimation of hydrogen crossover through Nafion® membranes in PEMFCs. Journal of Power Sources, 2011. **196**(4): p. 1833-1839.

141. Sompalli, B., B.A. Litteer, W. Gu, and H.A. Gasteiger, Membrane degradation at catalyst layer edges in PEMFC MEAs. Journal of The Electrochemical Society, 2007. **154**(12): p. B1349-B1357.

Appendix

Impedance at OCV

In order to verify the impedance data presented in chapter 6, the experiments were repeated with different MEAs. The experiments were performed by using a Baltic cell with H_2/air (or O_2) for anode/cathode at 40 °C with 100% RH for both sides. The EIS comparison at different voltages is shown in Figure I.1. Obviously, the semi-circle increases when the cell voltage increases in both cases. This is consistent with the literatures [115, 118]. Moreover, the R_{CT} in the case of air is bigger than that for O_2 at the same voltage. The R_{CT} difference between the two cases at the same voltage from 0.919 V to 0.948 V becomes smaller and smaller, varying from 2.7 times to 1.4 times. The R_{CT} under O_2 condition at open circuit condition is higher than that under air conditions but it has to be taken into account that the OCV with pure oxygen on the cathode side is always higher in comparison of the situation where air is used.

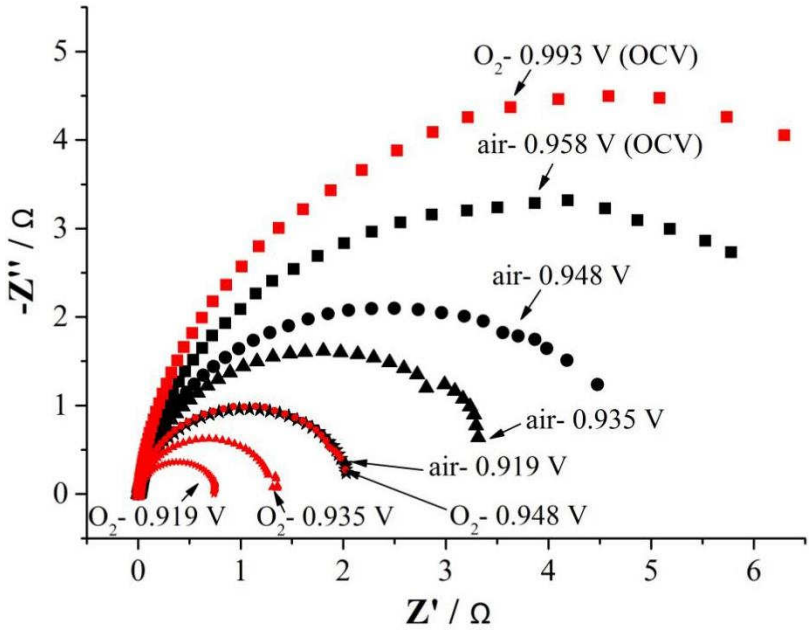

Figure I.1. The EIS curve of single cell at 40 °C with 100% RH for both sides under air and O_2 condition for the cathode side.

Figure I.2 displays the EIS curve at different current densities. Clearly, for both cases of air and O_2, the R_{CT} decreases with increases current density. Moreover, the R_{CT} for air is smaller than that for O_2 at same current density. This result is similar to literature [119], which has a close R_{CT} for air and O_2 at same current density.

The experiments were also repeated at 60°C and a relative humidity of 90%. They show the same trend and are not presented here.

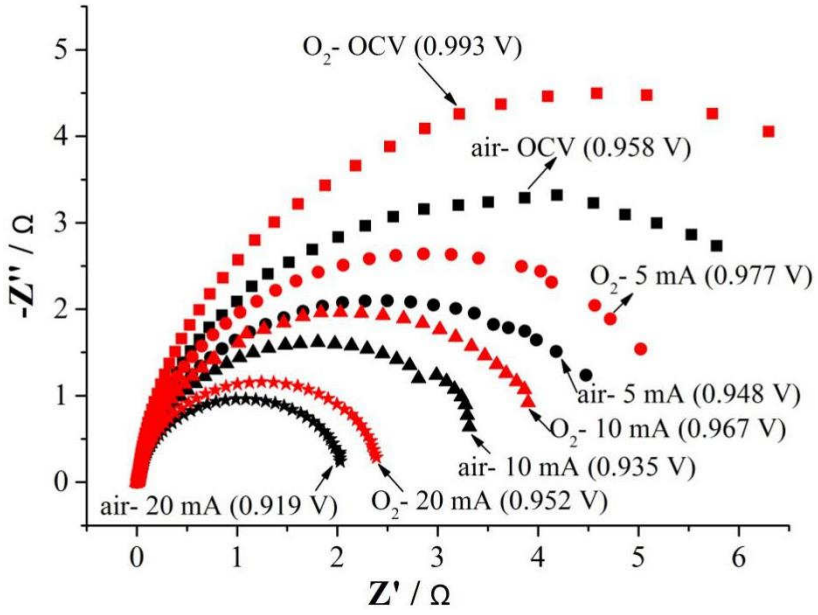

Figure I.2. The EIS curve of single cell at 40 °C with 100% RH for both sides under air and O_2 condition for the cathode side.

List of Figures

List of Tables

Acknowledgements

Firstly I am grateful to Prof. Werner Lehnert for his continuous support for my Ph.D study, for his patience, and abundant knowledge. I am also grateful to my supervisor, Dr. Uwe Reimer. He helped me a lot in all the time of my research in the last four years. His guidance and help makes me deeply understand the PEM fuel cells. Besides, I would like to thank the China Scholarship Council (CSC) for their financial support for my PhD research.

Very sincere gratitude goes out to my colleagues at IEK-3 for all of their help and patience. Especially, for Dr. Klaus Wippermann. In addition, this work was technically supported by Birgit Schumacher, Katja Klafki.

Also I thank my family, thanks for their support and encouragement all the time. In particular, I am grateful to my husband, Ruiyu Li, for his encouragement and cooperation in both work and life.

Finally, last but by no means least, I thank my thesis committee for their insightful comments and encouragement.

Thanks !